Bose-Einstein condensation of erbium atoms for fractional quantum Hall physics

Dissertation
zur
Erlangung des Doktorgrades (Dr. rer. nat.)
der
Mathematisch-Naturwissenschaftlichen Fakultät
der
Rheinischen Friedrich-Wilhelms-Universität Bonn

vorgelegt von
Daniel Frank Babik
aus
Köln

Bonn, November 2020

Angefertigt mit Genehmigung der
Mathematisch-Naturwissenschaftlichen Fakultät der
Rheinischen Friedrich-Wilhelms-Universität Bonn

1. Gutachter: Prof. Dr. Martin Weitz
2. Gutachter: Prof. Dr. Simon Stellmer

Tag der Promotion: 22.02.2021
Erscheinungsjahr: 2021

Abstract

With the advent of ultracold atomic gases experimentally realized by laser cooling techniques nearly 40 years ago, the doors to accessing novel physical behaviour have been opened wide and far. The possibility to prepare pure atomic samples of high coherence that can be precisely controlled and manipulated led to an abundance of opportunities for the study of fundamental quantum physical laws. Highlights in this research domain include the realization of Bose-Einstein condensation in dilute gases, degenerate atomic Fermi gases and even novel molecular physics. Experimentally, the investigation started with alkali atoms, proceeded with alkaline earth atoms, and only more recently laser cooling of atoms with higher complexity of their spectrum, as e.g. the highly dipolar lanthanide atomic species erbium and dysprosium, was realized. Those elements possess a non-vanishing orbital angular momentum in the ground state, leading to ample advantages for the manipulation with far-detuned laser light in phase imprinting schemes, as losses due to spontaneous scattering can be suppressed radically in comparison to the case of alkali atomic species. This beneficial behaviour will be used in the future for the generation of synthetic magnetic fields for electrically neutral erbium atoms aimed at investigating fractional quantum Hall physics. It will also be interesting to study novel interaction effects that due to the large dipole moment of the aforementioned lanthanide elements could arise in the context of artificial gauge fields.

This thesis describes in the first part the generation of an atomic erbium Bose-Einstein condensate in a hybrid crossed optical dipole trap. The main purpose of this endeavor was an enhancement of absolute atom number of the degenerate ensemble and long-term stability of the experimental setup with respect to the use of a single beam dipole trap. Atoms are loaded from an atomic erbium beam originating from an oven located inside an ultra-high vacuum chamber with the help of a spin-flip Zeeman slower and a transversal cooling stage at the transition wavelength near 400.91 nm wavelength into a narrow-line magneto-optical trap operating near 582.84 nm wavelength. After spatially compressing this trap, the cold atoms are loaded into a hybrid crossed optical dipole trap realized with two far-detuned focused laser beams, a mid-infrared beam near 10.6 μm wavelength emitted by a CO_2 laser and a transverse beam near 1.064 μm wavelength emitted by a Nd:YAG laser, and are subsequently evaporatively cooled until quantum degeneracy is reached. Starting from $5 \cdot 10^7$ atoms in the compressed magneto-optical trap, $7 \cdot 10^6$ atoms are loaded into the optical dipole trap, and finally a Bose-Einstein condensate with $3.5 \cdot 10^4$ atoms is realized. Here the critical temperature for the phase transition to a Bose-Einstein condensate was experimentally determined to be around 170 nK. The condensate is spin-polarized, and has a lifetime of up to 12 s. Also, a comparison of the here achieved results with respect to those achieved in only a single CO_2 laser beam dipole trap is presented.

In the second part of this thesis a theoretical evaluation of the generation of synthetic magnetic fields for ultracold erbium atoms in prospect for experimental investigations of fractional quantum Hall physics is given. One of the most promising techniques for the realization of

strong synthetic magnetic fields is by phase imprinting via Raman manipulation. Here for the theoretical calculation of such fields with erbium atoms a compared to earlier work on alkali atoms new modified optical Raman coupling scheme in a $\sigma^+ - \sigma^-$ beam polarization configuration is chosen. It is shown that sufficiently high field strengths with good spatial homogeneity can be reached for experimentally viable parameters. Additionally, an estimation for the expected Laughlin gap in the proposed erbium atomic fractional quantum Hall system is given.

For the future, it will be important to experimentally realize the expected possible large synthetic magnetic fields for a quantum gas of ultracold erbium atoms. Already at moderate synthetic field strengths, the study of vortices in such a dipolar quantum gas is an interesting topic. For larger field strengths the reaching of the fractional quantum Hall regime for the ultracold atomic gas sample is expected. On the theoretical side, here work describing the form of the ground state in the presence of both the synthetic magnetic field and dipolar interactions is of utmost importance.

Publication list

D. Babik, R. Roell, D. Helten, M. Fleischhauer, and M. Weitz, *Synthetic magnetic fields for cold erbium atoms*, Phys. Rev. **A** 101, 053603 (2020)

J. Ulitzsch, D. Babik, R. Roell, and M. Weitz, *Bose-Einstein condensation of erbium atoms in a quasielectrostatic optical dipole trap*, Phys. Rev. **A** 95, 043614 (2017)

Contents

1 Introduction

The generation of ultracold atomic gases offers the possibility to study a wide range of quantum phenomena in a very pure and well controllable system, with vibrant research activity since the mid 1980s. One of the highlights achieved with cold atoms is the demonstration of Bose-Einstein condensation, an effect theoretically discovered roughly 100 years ago. In 1924 A. Einstein predicted a new state of matter in the wake of his work on quantum statistics of massive bosonic particles, i.e. particles with integer spin: the Bose-Einstein condensate (BEC) [1–3]. Here single atoms are fully delocalized and the lowest energy state is macroscopically occupied, mathematically expressible by a single wavefunction describing the motion of the whole ensemble of particles, which is highly advantageous or often even absolutely essential for the study of quantum mechanical phenomena.

To reach such a condensate in atomic systems, the ensemble has to be cooled to ultralow temperatures typically in the nK regime, as the thermal de Broglie wavelength has to be larger than the average distance between the particles. The first experimental realization in the gaseous phase was achieved in 1995 by the groups of C. E. Wieman and E. A. Cornell as well as W. Ketterle [4, 5]. From then on many fundamental experiments regarding the coherence of macroscopic quantum states, novel quantum phases in optical lattices and interaction aspects of ultracold bound states were conducted with the help of BECs [6–8]. Importantly, Bose-Einstein condensates can be used for simulations of physics of other domains. One of the most notable areas has to be solid-state physics with systems that are generally not as flexible and easily manipulated as in the quantum optics case, where e.g. periodic structures can here be emulated by tunable optical lattices. A well-known example in this domain is the transition from a superfluid to a Mott-insulator [9]. Notable other experiments involve the detection of Bloch oscillations, and the study of topologically protected edge states [10, 11]. Besides variations of trapping potentials and irradiation with light fields, one popular way of manipulating ultracold atomic ensembles is by modifying the inter-particle interaction, which can be attractive, vanishing, or repulsive, with the help of an external magnetic field, where at distinct magnetic field strengths Feshbach resonances can occur [12–15].

Experimental simulations with BECs also come in handy when time dynamics of systems become too complex to study numerically, as e.g. for out-of-equilibrium interacting quantum matter [16]. Further research areas of interest for such simulations include fundamental concepts of statistical physics [17], and possibly quantum chemistry as well as high-energy physics [18]. Bose-Einstein condensation was also achieved for polaritons as well as photons [19, 20], where condensation is achieved at higher temperatures [20, 21]. Besides Bose-Einstein condensates, also degenerate quantum gases with fermionic atoms and corresponding Fermi-Dirac statistics could be realized experimentally [22–24], offering the possibility of a plethora of studies, as e.g. Fermi-Hubbard physics in optical lattices, aiding in the understanding of high-temperature superconductivity [25].

While in earlier works with cold atoms most of the Bose-Einstein condensates and degenerate Fermi gases were generated with elements from the group of the alkali atoms, as e.g. rubidium [4], which exhibit a comparatively simple electronic level structure due to their single valence electron, and later with elements from the group of the alkaline earth atoms, as e.g. strontium [26], which possess two valence electrons and feature a richer spectrum, a few years thereafter studies on spectrally very complex atomic species as e.g. the lanthanides from the group of rare earth metals increased, leading to the Bose-Einstein condensation and degenerate Fermi gas generation of several magnetic elements like dysprosium [27, 28], ytterbium [29], and erbium [30, 31], or in the case of thulium and holmium to laser-cooled atomic ensembles [32–34]. Additionally dipolar quantum mixtures of erbium and dysprosium have been realized [35]. Both dysprosium and erbium exhibit very rich spectra, and feature bosonic as well as fermionic isotopes with high relative occurrence, a non-vanishing electronic orbital angular momentum in their electronic ground states, which amount to $L = 6$ and $L = 5$ respectively, and high magnetic moments of 10 and 7 Bohr magnetons respectively. Reason for the complex energy spectra of lanthanides, with many transitions of various linewidths ranging from broad to ultra-narrow, are their incompletely filled $4f$ electron shells, leading to a so-called submerged shell structure, as the $4f$ shells are surrounded by the completely filled outer-lying $6s$ shell. For both dysprosium and erbium the d-wave collapse due to dipole-dipole interactions, as well as an abundance of Feshbach resonances, stemming from the lanthanides intricate electronic energy level structures, could be observed and described by random matrix theory [36, 37]. Other research in conjunction with dipolar physics included Fermi surface deformations, Feshbach-induced erbium molecules, an extended Bose-Hubbard model accounting for dipole-dipole-interactions, anisotropic collisions, BEC crossovers to dipolar macrodroplets, and studies of dipolar supersolids [38–43].

Ultracold atoms as a quantum simulator could also be used in the study of novel topological phases of matter that form in the sample when subjected to strong magnetic fields [44]. In this regard very interesting phenomena are expected for fractional quantum Hall states, as some of those could exhibit non-Abelian properties to possibly form topologically protected qubits [45], a feature that is highly sought after as current implementations of quantum computers despite tremendous advances in the field still suffer from non-robustness for too high numbers of qubits. As quantum Hall physics is normally only observable for charged particles subject to strong magnetic fields, for the electrically neutral ultracold lanthanide atomic case strong artificial magnetic fields via optical Raman manipulation have to be generated.

Prior experiments with the alkali atomic species rubidium were successful in creating synthetic magnetic fields, resulting in the observation of vortices in the rubidium BEC [46]. However, the maximum strength of the synthetic magnetic field is in alkali atoms based implementations using a phase imprinting scheme limited by the maximum useable detuning of the Raman light field. Elements from the group of the alkali atoms exhibit a S-ground state, i.e. possess an electronic orbital angular momentum of $L = 0$. The state-dependent manipulation with laser light of these atoms requires a detuning of magnitude below the size of the fine structure splitting of the electronically excited state [47]. Otherwise the energy shifts of all ground state levels become identical and are not dependent of the magnetic quantum number any more [48]. To prevent this behaviour the detuning of state-dependent optical lattices for example has to be chosen smaller than the fine structure, leading to higher photon scattering rates and therefore shorter coherence times of the BECs. Using erbium

or dysprosium atoms and their corresponding $L \neq 0$ ground state, such decoherence effects can be avoided, allowing state-dependent lattices with higher detuning, leading to longer coherence times [49]. Moreover, Raman manipulation between different ground state Zeeman sublevels, as of interest for the synthetization of large magnetic fields by phase imprinting, should then be possible with large detuning and corresponding long coherence times. For sufficiently strong synthetic magnetic fields studies of fractional quantum Hall physics with ultracold quantum gases could become possible [50, 51].

Specifically for the erbium system, the first realization of a magneto-optical trap (MOT), the latter being the standard tool to prepare a laser cooled ensemble as a first step in cold atom experiments, has despite the complex electronic structure of this lanthanide atomic species been achieved by McClelland and Hansen [52]. Further, evaporative cooling of these atoms due to their high dipolar moments and associated interaction effects require the use of traps being able to confine atoms in the lowest energetic Zeeman component of the electronic ground state, as possible with optical dipole traps. In earlier work of our group an experiment was built up which successfully prepared an ultracold atomic ensemble of erbium in a magneto-optical trap [53, 54], which was subsequently loaded into a quasi-electrostatic optical dipole trap realized by a focused CO_2 laser beam, where atoms were in a first step evaporatively cooled down to a few μK [55]. However due to the broad linewidth and the consequent high Doppler temperature of the 401 nm transition, together with the relatively high branching ratio of the transition, the losses during the cooling procedure were so high, that a BEC was ultimately not attainable. By using two cooling transitions, the 401 nm transition for slowing of the atomic beam on its way to the MOT chamber in a Zeeman slower, and the more narrow 583 nm transition for the actual trapping process, the group around F. Ferlaino finally managed to generate an erbium BEC. There after loading atoms from the narrow-line MOT into a crossed dipole trap formed by two laser beams at 1075 nm and 1064 nm wavelength, respectively, evaporative cooling was performed until quantum degeneracy was reached [30]. Enthused by the narrow-line magneto-optical trap setup, our working group was successful in creating an erbium BEC by evaporating atoms in a single beam CO_2 laser dipole trap [56, 57].

In the here presented thesis, a hybrid crossed dipole trap, consisting of a focused mid-infrared beam of a CO_2 laser operating near 10.6 μm wavelength and a Nd:YAG laser beam near 1064 nm wavelength, was realized. Erbium atoms loaded in such a trap were evaporatively cooled to Bose-Einstein condensation. Compared to the single beam CO_2 laser dipole trapping geometry, an increased atom number in the condensate and an improved long-term stability were achieved. A comparison of results obtained in both the single beam CO_2 laser dipole trap and the new hybrid crossed dipole trapping geometry is presented.

In further work contained in this thesis, a proposal to realize strong synthetic magnetic fields with cold erbium atoms is given based on phase imprinting by Raman manipulation. The unusual electronic structure of this rare earth multi-level atom is expected to allow for large synthetic magnetic fields. An estimate for the size of the Laughlin gap of the proposed two-dimensional system, devised for the future observation of the fractional quantum Hall effect, is given.

The work presented here consists of six chapters, with the introduction at hand being Chap. 1. In the following Chap. 2 properties of atomic erbium are described, and theoretical consider-

ations regarding the various experimental steps for generating a Bose-Einstein condensate of erbium atoms are laid out. Chap. 3 shows the experimental setup and methods, including the vacuum apparatus and the employed light sources, as well as the controlling setup of the optical dipole trap light. In the subsequent Chap. 4 a characterization of the experimental setup and the obtained experimental results are given. The theoretical derivation of a synthetic magnetic field for ultracold erbium atoms is conducted in Chap. 5, followed by a look on the Laughlin gap of the described system. The thesis closes with a conclusion and an outlook on future prospects in Chap. 6. There further plans for the next theoretical and experimental steps are outlined.

2 Theoretical background: Ultracold atomic erbium quantum gases

The generation of Bose-Einstein condensates involves several experimental steps, here tailored for the erbium atomic case. Below theoretical considerations for the understanding of the experiment are presented, starting with the treatment of ultracold Bose gases in a harmonic trapping potential, followed by a review of important properties of atomic erbium, and proceeded with the theoretical discussion regarding the at this experiment employed stages for the realization of an erbium Bose-Einstein condensate.

2.1 Low-temperature behaviour of Bose gases

S. N. Bose first introduced the concept of an ideal Bose gas consisting of free, non-interacting particles via Bose-statistics [3], which was extended to massive bosons by A. Einstein, who also predicted a phase transition of a thermal Bose gas to a Bose-Einstein condensate [2], where the particles occupy the ground state of the system macroscopically, leading to a single wavefunction for the whole ensemble. It takes place for sufficiently high phase space densities, that can be achieved by increasing the density and decreasing the temperature of the ensemble below a critical non-vanishing temperature. This phase transition works only for bosonic particles with integer spin, which exhibit a symmetric multi-particle wavefunction, and therefore can be in the same quantum mechanical state simultaneously as the Pauli principle does not hold. In contrast for fermions with half-integer spin, the Pauli principle holds and a quantum mechanial state cannot be occupied by two or more fermions with the same set of quantum numbers [58].

The below mathematical treatment follows [6, 56, 59]. Consider N bosonic atoms trapped in an external harmonic potential, so that the particles act as N individual harmonic oscillators, an approximation for the center of mass motion of the whole ensemble. The potential for each particle will take the form of

$$V_{\text{ext}}(\mathbf{r}) = \tfrac{1}{2}m(\omega_x^2 x^2 + \omega_y^2 y^2 + \omega_z^2 z^2) \tag{2.1}$$

with position space vector $\mathbf{r} = (x, y, z)$, mass m of the bosons, and trap frequencies $\omega_{x,y,z}$. For a dilute gas we can neglect the atom-atom interaction, and the system's Hamiltonian can be written as the sum of single-particle Hamiltonians with energy levels

$$\epsilon(n_x, n_y, n_z) = \left(n_x + \tfrac{1}{2}\right)\hbar\omega_x + \left(n_y + \tfrac{1}{2}\right)\hbar\omega_y + \left(n_z + \tfrac{1}{2}\right)\hbar\omega_z, \tag{2.2}$$

where $\hbar = h/2\pi$ is the reduced Planck constant, and for the quantum numbers $n_{x,y,z}$ it holds that $n_{x,y,z} \in \mathbb{N}$. In the case of grand canonical ensembles the mean occupation number $\langle n(\epsilon_{n_x,n_y,n_z})\rangle$ of state $|n_x, n_y, n_z\rangle$ with energy $\epsilon(n_x, n_y, n_z)$ is defined by

$$\langle n(\epsilon_{n_x,n_y,n_z})\rangle = \frac{1}{e^{(\epsilon_{n_x,n_y,n_z}-\mu)/k_\mathrm{B}T}-1}, \tag{2.3}$$

where all $\epsilon_{n_x,n_y,n_z} > \mu$, with μ being the chemical potential, k_B the Boltzmann constant, and T the temperature. Here μ is fixed by the total particle number

$$N = \sum_{n_x,n_y,n_z} \frac{1}{e^{(\epsilon_{n_x,n_y,n_z}-\mu)/k_\mathrm{B}T}-1}, \tag{2.4}$$

but is still a function of the temperature T. To calculate the critical temperature one has first to determine the density of states $g(\epsilon)$. By integrating Eq. 2.4 one obtains the number of states $G(\epsilon)$ below energy ϵ (excluding the zero-point energy), and finally can calculate the density of states as $g(\epsilon) = dG/d\epsilon = \epsilon^2/(2\hbar^3\omega_x\omega_y\omega_z)$. As a next step the number of excited states for a vanishing chemical potential can be considered via

$$N_\mathrm{ex} = \int_0^\infty d\epsilon g(\epsilon)\langle n(\epsilon,\mu=0)\rangle. \tag{2.5}$$

With this condition the critical temperature T_c is defined as the highest temperature at which a macroscopical occupation of the lowest energy state appears, and the following holds:

$$N = N_\mathrm{ex}(T_\mathrm{c}) = \int_0^\infty d\epsilon g(\epsilon)\frac{1}{e^{\epsilon/k_\mathrm{B}T_\mathrm{c}}-1}. \tag{2.6}$$

Solving Eq. 2.6 leads to the critical temperature as

$$T_\mathrm{c} = \frac{\hbar}{k_\mathrm{B}}\left(\frac{\omega_x\omega_y\omega_z N}{\zeta(3)}\right)^{1/3} \approx 0{,}94\cdot\frac{\hbar\bar{\omega}}{k_\mathrm{B}}N^{1/3}. \tag{2.7}$$

where $\zeta(\alpha)$ is Riemann's Zeta function, and $\bar{\omega} = (\omega_x\omega_y\omega_z)^{1/3}$ is the geometric average of the oscillator frequencies. As long as the temperature is below the critical temperature T_c, a macroscopically occupation of the lowest energy level is possible. With in this experiment typical values for the mean trap frequency of about $\bar{\omega} = 2\pi\cdot 93\,\mathrm{Hz}$, and for the atom number of approximately $3.5\cdot 10^4$, the phase transition from an ideal Bose gas to a Bose-Einstein condensate should theoretically occur at a critical temperature of $T_\mathrm{c} = 136\,\mathrm{nK}$. The fraction of atoms in the condensate for temperatures below T_c can be calculated via the relation

$$\frac{N_0}{N} = 1 - \left(\frac{T}{T_\mathrm{c}}\right)^3, \tag{2.8}$$

where N_0 is the atom number in the ground state, N is the total atom number, and $T < T_\mathrm{c}$ is the temperature of the ensemble. For a temperature of $T = 0$ the gas would theoretically condensate completely.

Bosons can be considered as quantum mechanical objects that appear in the form of wavepackets with size in the order of the de-Broglie wavelength $\lambda_{\mathrm{dB}} = \sqrt{2\pi\hbar^2/(mk_{\mathrm{B}}T)}$. Near the critical temperature interparticle distances become comparable to λ_{dB}, and the wavepackets start to overlap. The phase space density ρ is an important marker in determing the current phase the ensemble exhibits. It is defined as the number of particles in a cube of edge length equal to the thermal de Broglie wavelength λ_{dB}:

$$\rho = n\lambda_{\mathrm{dB}}^3 = n\left(\frac{2\pi\hbar^2}{mk_{\mathrm{B}}T}\right)^{3/2}. \tag{2.9}$$

When the critical phase space density ρ_{c} is reached, the transition to quantum degeneracy occurs. The resulting macroscopical wavefunction from the overlapping wavepackets can be interpreted as the Bose-Einstein condensate. Assuming a uniform Bose gas in a three-dimensional box with volume V the critical temperature can be calculated as

$$T_{\mathrm{c}} = \frac{2\pi}{k_{\mathrm{B}}[\zeta(3/2)]^{3/2}}\frac{\hbar^2 n^{3/2}}{m} \approx 3.31 \cdot \frac{\hbar^2 n^{3/2}}{m}, \tag{2.10}$$

where $n = N/V$ is the particle number density. Using Eq. 2.9 and Eq. 2.10 one obtains the critical phase space density as

$$\rho_{\mathrm{c}} \approx 2.612. \tag{2.11}$$

Thus for the preparation of a Bose-Einstein condensate the atoms must be prepared as dense and cool as possible. On the other hand measurements of the phase space density can provide a neat way to experimentally verify if Bose-Einstein condensation occured.

2.2 Some properties of the atomic erbium system

Erbium is one of the chemical elements in the lanthanide series with atomic number of $Z = 68$ and atomic mass of 167.26 amu, with $1\,\mathrm{amu} = 1.6605402 \cdot 10^{-27}\,\mathrm{kg}$ [60], discovered in a mixture of rare earth metal elements, which show similar geochemical characteristics, in 1843, and first successfully isolated in 1934 [61–63]. Naturally, erbium occurs mostly in chemical compounds as e.g. monazites, a brown phosphate ore mineral. Pure solid erbium appears as a soft, silvery-white metal if kept away from air, as it would otherwise oxidize slowly to the tarnished erbium(III) oxide. It possesses a melting point of 1802 K and a boiling point of 3136 K [64].

Besides the many qualities of ionic erbium Er^{3+} as a doping agent for crystals in technical and scientific applications ranging from telecommunications to quantum storage and even medical therapies [65–69], another outstanding feature is found for atomic erbium with its high magnetic moment of $7\mu_{\mathrm{B}}$, where μ_{B} is the Bohr magneton [70], which belongs to the strongest magnetic moments in the periodic table, leading to interesting dipolar effects observable in the ultracold regime. In comparison alkali metals only possess a magnetic moment of $1\,\mu_{\mathrm{B}}$. In nature there exist six different stable isotopes of erbium, five bosonic and one fermionic, with

Isotope	Abundance [%]	Nuclear spin $I[\hbar]$
^{162}Er	0.14	0
^{164}Er	1.56	0
^{166}Er	33.4	0
^{167}Er	22.9	7/2
^{168}Er	**27.1**	**0**
^{170}Er	14.9	0

Tab. 2.1: Properties of the different erbium isotopes: Listed are the relative abundance and the nuclear spin which is 0 for all bosonic isotopes. ^{167}Er is the only fermionic isotope of erbium. Although ^{166}Er has the highest relative abundance, in this experiment the highlighted ^{168}Er is used as it exhibits favorable scattering properties beneficial for efficient evaporative cooling. Data from [56, 64].

their respective relative occurence listed in Tab. 2.1. Due to favorable scattering properties and therefore greater rethermalization rates in evaporative cooling processes the isotope of choice for Bose-Einstein condensation became ^{168}Er [71]. Commercially, bulk erbium with a purity of around 99.99 % with its natural relative abundance of all stable isotopes is readily available. Erbium exhibits getter properties acting beneficial on ultra-high vacuums employed in ultracold atoms experiments [72].

Erbium atoms feature 68 electrons that are distributed corresponding to the aufbau principle and the Madelung rule. The $6s$ orbital gets filled before the $4f$ orbital, leading to an inner partially unfilled shell, which for erbium results in the following electronic configuration:

$$[\mathrm{Xe}]\, 4f^{12}\, 6s^2, \tag{2.12}$$

where [Xe] indicates the electronic configuration of Xenon. In the atomic erbium ground state the $4f$ shell misses two electrons to be completey filled, leading to a so-called submerged shell structure, and the occurrence of a large orbital angular momentum quantum number $L = 5$, and spin quantum number $S = 1$. For the ground state LS-coupling is applicable, leading to an angular momentum quantum number of $J = 6$ and a ground state expression of

$$[\mathrm{Xe}]\, 4f^{12}\, 6s^2\, {}^3\mathrm{H}_6, \tag{2.13}$$

with the state notation $^{2S+1}L_J$. For the case of excited states of atomic erbium the jj-coupling becomes more prominent, at which here J_1J_2-coupling is applied, where the electrons in all inner shells, i.e. electrons in the [Xe] configuration, and all outer electrons in the $6s$ shell couple independently according to the LS-coupling to states with angular momentum quantum numbers J_1 and J_2. These states get summed up via quantum number J, denoted as $(J_1,J_2)_J$, to the total angular momentum quantum number $\mathbf{J} = \mathbf{J_1} + \mathbf{J_2}$ [73].

2.2.1 Energy level scheme and relevant transitions

Erbium displays a rich energy level scheme as a result of its complex submerged electronic shell structure, which is partly shown in Fig. 2.1, with all states up to an energy of 25000 cm^{-1}.

Wavelength [nm]	Energy $\left[\mathrm{cm}^{-1}\right]$	Natural linewidth
400.91	24943.272	(29.7 ± 0.6) MHz
582.84	17157.307	(186 ± 10) kHz
631.04	15846.549	(28 ± 7) kHz
841.22	11887.503	(8.0 ± 0.2) kHz

Tab. 2.2: Some prospective optical cooling transitions starting from the atomic erbium ground state [71,77–79], three of which are shown in Fig. 2.1. While the transitions near wavelength 400.91 nm and 582.84 nm are used for optical cooling in this experiment, the inner-shell transition near 841.22 nm will be utilized in the future for Raman manipulation within the scope of generating articial magnetic fields.

Erbium ionizes at $49262\,\mathrm{cm}^{-1}$, corresponding to the energy of a photon of about 203 nm wavelength. In total there exist 674 states, ranging from $J = 1$ to 12 [74], however it is assumed that the spectroscopic data is still to this date not complete, with more dipole allowed transitions of the ground state predicted [75]. Suitable optical transitions for laser cooling, as discussed later in this chapter, with $J \rightarrow J' = J + 1$, while also changing parity to yield a non-vanishing matrix element, have to be as optically closed as possible. Especially as some of erbium's states exhibit comparatively large lifetimes, called metastable states, decays from higher excited laser cooling states into these states would require the usage of repumping lasers to rescue the atoms to the ground state to make them again available for laser cooling, which for many metastable states can quickly become experimentally unfeasible [76]. In earlier work potentially usable cooling transition were studied [77], shown in Tab. 2.2.

In this experiment the transition near 400.91 nm wavelength is used for the Zeeman slower and transversal cooling process, as well as absorption imaging purposes, as it exhibits a broad natural linewidth providing a strong deceleration force acting on the atoms [52]. For the magneto-optical trap, however, the narrow-line transition near 582.84 nm wavelength is used, as it features a small natural linewidth and correspondingly a lower Doppler temperature, which is beneficial for reaching quantum degeneracy in later experimental steps as the starting conditions greatly improve in comparison to the broad blue erbium transition here only used for optimizing the atomic loading rate into the magneto-optical trap, similar to other work [30]. No repump lasers are needed for these transitions, as very few loss channels with small transition rates are present, especially for the transition near 582.84 nm [77, 80]. More details on the Zeeman slower and the magneto-optical trap can be found in Secs. 2.3.1 and 2.3.2. Laser systems and optical setups were mainly implemented within the scope of previous work at our experiment [55–57]. Wavelengths of laser light used in subsequent experimental steps for optical dipole trapping should in general be as far away as possible from any excited state transition to minimize off-resonant scattering, further discussed in 2.3.3.

The three relevant transitions highlighted in Fig. 2.1 are shortly discussed in the following. For the broad 400.91 nm transition with a natural linewidth of around 29.7 MHz an excited $6p$ electron couples with the remaining $6s$ electron to a $^1\mathrm{P}_1$ singlet state. The other inner electrons LS-couple to a $^3\mathrm{H}_6$ state. Both these states then jj-couple to a $(J_1,J_2)_J$ state, leading to an excited state $[\mathrm{Xe}]4f^{12}(^3\mathrm{H}_6)6s6p(^1\mathrm{P}_1)(6,1)_7$. Analog for the 582.84 nm transition the excited $6p$ electron couples with the remaining electron to a $^3\mathrm{P}_1$ triplet state, representing

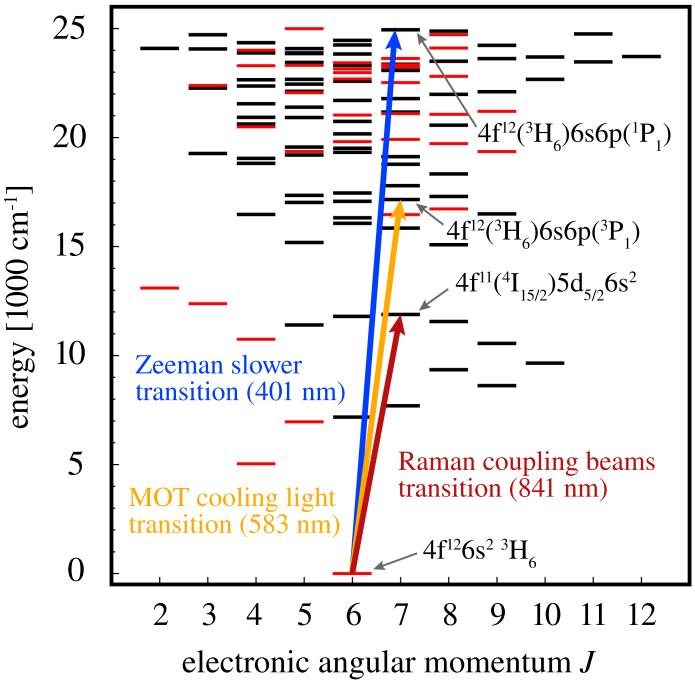

Fig. 2.1: Energy level scheme for atomic erbium. Shown are levels with even parity in red, and levels with odd parity in black respectively, up to an energy of 25000 cm^{-1}. Three transitions are illustrated, from which two are needed for optical cooling (blue and yellow), and an inner-shell one is needed for the experimental realization of optical Raman manipulation (dark red), for which theoretical considerations can be found in Chap. 5 of this thesis. Data from [74], image adapted from [52].

an intercombination line, i.e. an electric dipole transition that violates the spin-conserving selection rule, which features a narrow natural linewidth of about 186 kHz. Accordingly the resulting excited state is $[\mathrm{Xe}]4f^{12}(^3\mathrm{H}_6)6s6p(^3\mathrm{P}_1)(6,1)_7$. Now for the very narrow 841.22 nm transition with a natural linewidth of approximately 8 kHz an inner-shell electron from the $4f$ orbital is excited to the $5d_{5/2}$ state. Here the remaining electrons couple to a $^4\mathrm{I}_{15/2}$ state. The resulting excited state from the jj-coupling between those states is denoted as $[\mathrm{Xe}]4f^{11}(^4\mathrm{I}_{15/2})5d_{5/2}6s^2(15/2,5/2)_7$. Some relevant characteristics of the three transitions are listed in Tab. 2.3.

Several lanthanide elements feature extraordinary large magnetic moments, a property caused by the submerged shell structure and the corresponding electron spin-orbit coupling resulting in large total angular momentum quantum numbers J. As values of the magnetic quantum numbers m_J, indicating the projection of $\mathbf{J}$ on an externally set quantization axis, can range from $-J$ to J, the magnetic moment is then proportionally large according to

$$\mu = m_J g_J \mu_\mathrm{B}, \tag{2.14}$$

where μ_B is Bohr's magneton, and g_J is the atomic Landé g-factor. In the case of ground state erbium the Landé g-factor was experimentally determined to be $g_J = 1.163801(1)$ [81], with theoretical derivations showing similar results [71]. Lanthanides with the largest magnetic moment include terbium and dysprosium (about 10 μ_B each), holmium (approximately 9 μ_B),

Wavelength λ [nm]	400.91	582.84	841.22
Transition rate Γ $\left[\mathrm{s}^{-1}\right]$	$1.9 \cdot 10^8$	$1.2 \cdot 10^6$	$5.0 \cdot 10^4$
Natural linewidth $\Delta\nu$ [MHz]	29.7	0.186	0.008
Saturation intensity I_S [mW/cm^2]	60.3	0.13	0.002
Doppler temperature T_D [μK]	714	4.6	0.2
Recoil temperature T_R [nK]	717	339	81

Tab. 2.3: Characteristics of atomic erbium transitions used in the here presented work [71, 78, 79]. The saturation intensity is defined as $I_\mathrm{S} = \pi hc\Gamma/(3\lambda^3)$, with c being the speed of light, and λ being the transition wavelength. Doppler T_D and recoil temperatures T_R are discussed within Eq. 2.17 and Eq. 2.19 respectively. As the transition near 582.84 nm exhibits a Doppler temperature roughly 150 times smaller than the broad transition near 400.91 nm, the starting conditions for the generation of a Bose-Einstein condensate can be greatly improved by the use of a two-stage optical cooling process consisting of a broad-line Zeeman slower and transversal cooling stage, as well as a narrow-line magneto-optical trap.

and europium as well as erbium (roughly $7\,\mu_\mathrm{B}$ each) [70]. More precisely erbium's magnetic moment in the lowest magnetic state with $m_J = -6$, in which the prepared spin-polarized ultracold atomic erbium ensemble resides in this experiment, amounts to

$$\mu = -6.982806(6)\,\mu_\mathrm{B}. \tag{2.15}$$

Alkali metal atoms on the other hand possess a small magnetic moment of $\mu = 1\,\mu_\mathrm{B}$ in the ground state stemming from their single s-orbital electron.

In an external magnetic field B states with a total angular momentum quantum number J split into $2J+1$ states with magnetic quantum number m_J [82]. The Zeeman energy shift ΔE_Z relative to the energy at zero magnetic field is calculated via

$$\Delta E_\mathrm{Z} = m_J g_J \mu_\mathrm{B} B = \mu B. \tag{2.16}$$

For smaller external magnetic fields the energy splitting between two neighboring m_J states of atomic erbium shows linear behaviour with a slope of $g_J\mu_\mathrm{B} = 1.628879\,\mathrm{MHz/G}$ [71, 83]. Effectively, for all experimentally achievable magnetic field strengths employed within the scope of ultracold atom experiments, this linear dependency should hold due to erbium's large spin-orbit coupling constant [83]. To drive a transition between two Zeeman states $m_J \to m_J' = m_J \pm 1$, radio frequency (rf) fields can be applied to the atoms, which in this experiment is e.g. used to unambiguously verify the spin-polarization of the atomic ensemble after preparation in the magneto-optical trap.

2.3 Background on an experimental realization of a Bose-Einstein condensate

Here the various experimental ingredients needed for the generation of an atomic erbium Bose-Einstein condensate are introduced, and their theoretical background discussed. In

short the steps include first stage laser cooling of an atomic erbium beam via broad-line Zeeman slower and transversal cooling, second stage laser cooling via narrow-line magneto-optical trap, loading into single or hybrid optical dipole traps, and subsequent evaporative cooling until quantum degeneracy is reached. The ensemble is prepared inside an ultra-high vacuum chamber to minimize perturbations by the environment.

2.3.1 Laser cooling

Laser cooling is an experimental method to decelerate atoms, and thus for an equilibrium distribution to reduce the mean velocity of atoms, by the use of light, as in the following described via [84]. The mean kinetic energy of all particles of an ideal gas is proportional to its mean squared velocity $\overline{v^2}$ and temperature T, respectively [85], so that the temperature can be expressed via $T = m\overline{v^2}/(3k_\mathrm{B})$. The velocity of each atom inside the gas can be decreased by momentum transfer from photons with appropriate momentum of $|\mathbf{p}| = \hbar\,|\mathbf{k}|$ per photon, with $\mathbf{k}$ being the wavevector of the absorbed photon. After absorption the atom occupies an energetically excited state for a mean duration of the spontaneous lifetime, from which it can then relaxate into a lower state by stimulated or spontaneous emission of a photon. While for the case of stimulated emissions no net momentum transfer takes place, for spontaneous emissions a net momentum transfer occurs after many absorption and emission cycles as the sum of all momenta from emitted photons averages to zero over time, but the sum of all momenta from absorbed photons does not, leading to a so-called spontaneous force, which for the case of a magneto-optical trap in one dimension is shown in Eq. 2.21. Thus we can change the velocity $\mathbf{v} = \mathbf{p}/m$ of atoms by directed illumination with resonant photons from e.g. a laser beam. The spontaneous force can be mathematically derived from the description of a two-level system using the Bloch equations [84]. For atoms moving in opposite direction to the laser light propagation direction, the Doppler shift $\Delta\omega = \pm\omega_0 v/c = \mathbf{kv}$, where $\Delta\omega$ is the frequency shift away from the atomic resonance frequency ω_0 [86], has to be countered by red-detuning the light frequency.

For optical cooling of an atomic ensemble in a fixed position in space, three pairs of counter-propagating laser beams are necessary. The atomic ensemble, then also called optical molasses, only experiences a reduction of the mean velocity, but not a restoring force in position space, so that they can spatially diffuse out of the molasses [87]. The in Sec. 2.3.2 discussed upgrade, named magneto-optical trap, adds such a restoring force by applying a linear magnetic field gradient in each spatial dimension to make trapping of atoms without diffusion possible. In the idealized system of a two-level atom with the choice of a red-detuning of $\delta = -\Gamma/2$, where $\Gamma = 1/\tau$, and τ being the lifetime of the excited state, one obtains the so-called Doppler temperature, which acts as a lower limit for the standard optical cooling process, as

$$T_\mathrm{D} = \frac{\hbar\Gamma}{2k_\mathrm{B}}. \tag{2.17}$$

Other cooling techniques like polarization gradient cooling can reach even lower temperatures [88]. The fundamental limit stemming from the discrete momentum transfer of a single photon is represented by the recoil temperature [89]

$$T_{\mathrm{R}} = \frac{\hbar^2 \Gamma^2}{m k_{\mathrm{B}}}. \tag{2.18}$$

It should be noted that also techniques for subrecoil laser cooling have been demonstrated [90].

In the present experiment, erbium atoms are loaded from an atomic beam into the magneto-optical trap for the preparation of an ultracold atomic ensemble. As erbium exists as a solid at room temperature, it has to be heated greatly in a crucible, embedded in a two-stage effusion cell including apertures for collimation, as seen in a sketch in Fig. 2.2, and in a technical drawing in Fig. 3.2. The emerging atomic beam from the effusion cell can be further collimated by means of transversal cooling techniques [71,91], which reduces the mean transversal velocity of the atoms and therefore the divergence angle of the atomic beam [92,93]. Transversal cooling utilizes laser cooling in one dimension using two counter-propagating resonant laser beams perpendicular to the atomic beam. This is typically applied in both dimensions orthogonal to the atomic beam axis, so that in total two beam pairs (four beams) irradiate the atoms. Ideally elliptically shaped beam profiles are used to maximize the interaction area and therefore interaction time of the light with the passing atoms, leading to a stronger collimation effect. Ultimately the atomic flux is increased, as indicated in Fig. 2.2. It is however limited by the aperture with diameter d_{ct} of the next connecting tube in the vacuum system that leads to the Zeeman slower.

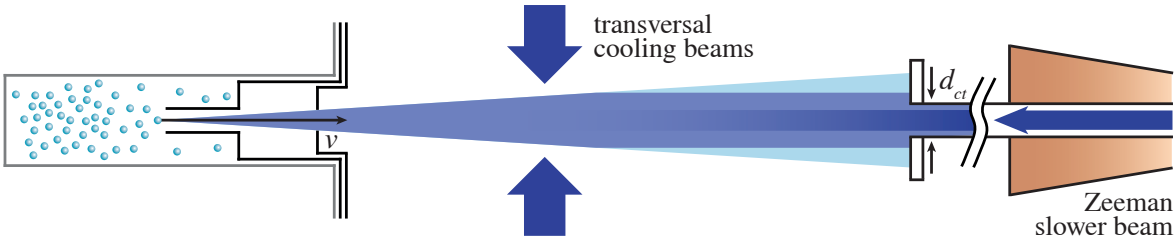

Fig. 2.2: Outline of the transversal cooling and Zeeman slower light setup. With two counter-propagating resonant laser beams in one dimension perpendicular to the atomic beam axis the latter can be collimated, i.e. the divergence angle can be reduced (here shown from cyan to lavender), leading to a higher atomic flux at the aperture with diameter d_{ct} of the connecting tube between effusion cell chamber and main vacuum chamber. The here used laser beams exhibit an elliptic beam profile to maximize the interaction area with the atomic beam. The Zeeman slower laser beam (shown in dark purple, with some part of the Zeeman slower coil profile here being indicated as coppery geometry) travels along the tube axis and counter-propagates the atomic beam. A portion of the collimated beam scatters light from the Zeeman slower beam and is continuously decelerated on the way to the main vacuum chamber inside the Zeeman slower. A complete view of the setup can be seen in Fig. 3.1. Transversal cooling sketch adapted from [56].

The transversal cooling stage only collimates the atomic beam, but does not slow the atoms in longitudinal direction. Due to a much higher mean velocity than the capture velocity of the magneto-optical trap, as briefly discussed in Sec. 3.2, such a longitudinal deceleration is needed and here provided by a so-called Zeeman slower [94]. A counter-propagating laser beam reduces the velocity of the atoms via optical cooling as sketched in Fig. 2.2. Because a somewhat slowed down atom soon would not be resonant with the laser beam of frequency ω anymore due to the Doppler effect, the resonance condition

$$\omega_0 - kv(z) + \frac{\tilde{\mu}}{\hbar} B(z) = \omega \tag{2.19}$$

has to be continuously met with the help of a spatially varying magnetic field $B(z)$ along the Zeeman slower axis in z-direction, which changes the energy levels of the atoms via the Zeeman effect at each position appropriately. $\tilde{\mu} = \mu_\mathrm{B}(g_e m_e - g_g m_g)$ is the difference between magnetic moments of excited and ground state. Here a long-standing spin-flip Zeeman slower with a maximum capture velocity of $v_\mathrm{max}^\mathrm{ZS} \approx 600\,\mathrm{m/s}$ and an arbitrarily low minimum capture velocity, respectively, is used [55].

2.3.2 Magneto-optical trap

In addition to the laser cooling effect possible in the optical molasses discussed in Sec. 2.3.1 to cover also a restoring force in position space and actually trap atoms spatially without the risk of diffusion, one can apply a magnetic quadrupole field resulting in a so-called magneto-optical trap (MOT) [76], where the theoretical description below follows [84]. The MOT consists of three pairs of red-detuned, counter-propagating and circularly polarized laser beams, with one pair along each spatial direction, and two magnetic field coils in anti-Helmholtz configuration, shown as a sketch in Fig. 2.3. The coils produce the magnetic quadrupole field with its point of origin lying at the intersection point of the laser beams, which exhibits an approximately linear behaviour in each spatial axis around the origin. For simplicity we consider only one spatial dimension and a two level system with a $J = 1$ excited state in the following. The inhomogeneous magnetic field of form $B(z) = bz$, with slope b and $B(0) = 0$, splits the three Zeeman levels $m_J = 0, \pm 1$ of the excited state energetically in respect to position z, while the single Zeeman level of the ground state with $J = 0$ and $m_J = 0$ is unaffected, as seen in Fig. 2.4(a).

If the two counter-propagating beams in direction of the magnetic field gradient are right (σ^+) and left circularly (σ^-) polarized respectively, due to the selection rules for electric dipole transitions they preferably excite the $m_J = +1$ and $m_J = -1$ transition respectively. If σ^+ polarized light is irradiated from the side with the $m_J = +1$ state being energetically lower and therefore closer to resonance with the laser light ($z < 0$), atoms further away from the center will experience an increased spontaneous force pushing them back to the center of the MOT. For the same considerations of the other side ($z > 0$) now with σ^- polarized light, one ascertains that the atoms will here also experience a spontaneous force directed to the MOT center region. Thus for a pair of counter-propagating beams along each of the three spatial axes the atoms can be trapped position-dependently in space. The spontaneous force along one axis, e.g. the z-axis, can be written as

$$F_z^\mathrm{MOT} = \frac{\hbar k \Gamma}{2} \left(\frac{s}{1 + s + \frac{4(\delta - kv_z + \tilde{\mu}\partial_z Bz/\hbar)^2}{\Gamma^2}} - \frac{s}{1 + s + \frac{4(\delta + kv_z - \tilde{\mu}\partial_z Bz/\hbar)^2}{\Gamma^2}} \right), \tag{2.20}$$

where $s = I/I_\mathrm{S}$ is the saturation parameter with I being the light intensity, and I_S being the saturation intensity respectively.

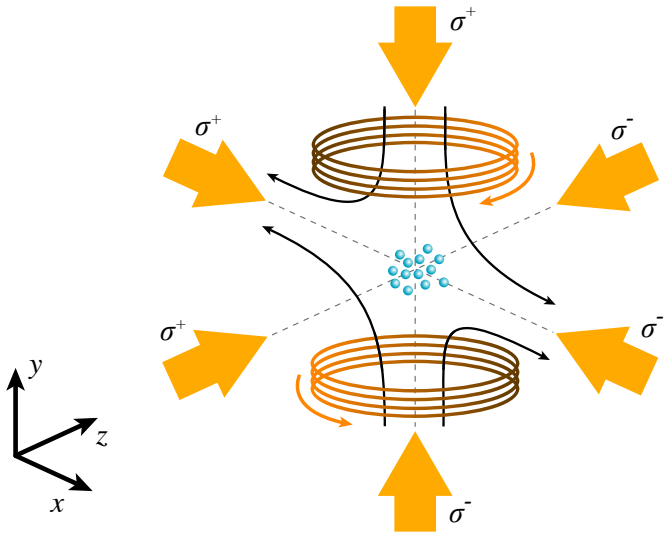

Fig. 2.3: Sketch of a magneto-optical trap setup, where atoms are trapped in the intersection volume of three counter-propagating laser beam pairs, that are arranged orthogonally in respect to each other along the x, y, and z-axis (suggested as dashed gray lines), respectively, with the beams on each axis being oppositely circularly polarized. The magnetic field coils in anti-Helmholtz configuration (with the current direction marked with orange arrows) generate a magnetic quadrupole field, which behaves approximately linearly in the center region of the trap. As an example the magnetic field lines (solid black) are here indicated for the x-y-plane, but can be imagined rotationally symmetric around the y-beam axis for the shown coil configuration.

Magneto-optical trap for erbium atoms with narrow-line transition light

The narrow-line erbium transition at $\lambda = 582.84\,\text{nm}$ offers a big advantage since the Doppler temperature of the atomic ensemble becomes much smaller than for a broader transition as e.g. the one at $\lambda = 400.91\,\text{nm}$ (cf. Tab. 2.3), leading to a much better starting point to reach quantum degeneracy in further experimental steps. This narrow-line transition is not completely optically closed, but possesses two sufficiently small loss channels into metastable states which permits successful MOT operation without the need for repumping [77, 80]. The use of a narrow-line cooling transition introduces a more sophisticated trapping behaviour, which is briefly discussed in this section, with more details to be found in [56, 71, 95].

Due to the narrow-line and therefore weak MOT transition, the comparatively strong light of the Zeeman slower would perturb the trapping (or so-called loading) of atoms into the MOT if both would be spatially overlayed as in typical configurations. One can utilize the weak force of the MOT light via a far detuning of several linewidths from resonance, in combination with a corresponding tuning of the MOT magnetic field gradient, to create a sphere of larger radius, effectively seperating Zeeman slower beam and magneto-optical trapping region [96]. Considering also gravitation, the atoms are then not trapped inside a sphere but gather in a gravitational sag of an ellipsoid, see sketched in Fig. 2.4(b) and photographed in Fig. 4.2(a). Thereby the atomic ensemble mostly interacts with the lower σ^- polarized MOT beam along y so that the ensemble becomes spin-polarized as most atoms will occupy the Zeeman state with $m_J = -6$, an effect that will be beneficial for the further experimental steps. The total force acting on an atom in the axis featuring gravitation, here the y-axis, with velocity v_y at

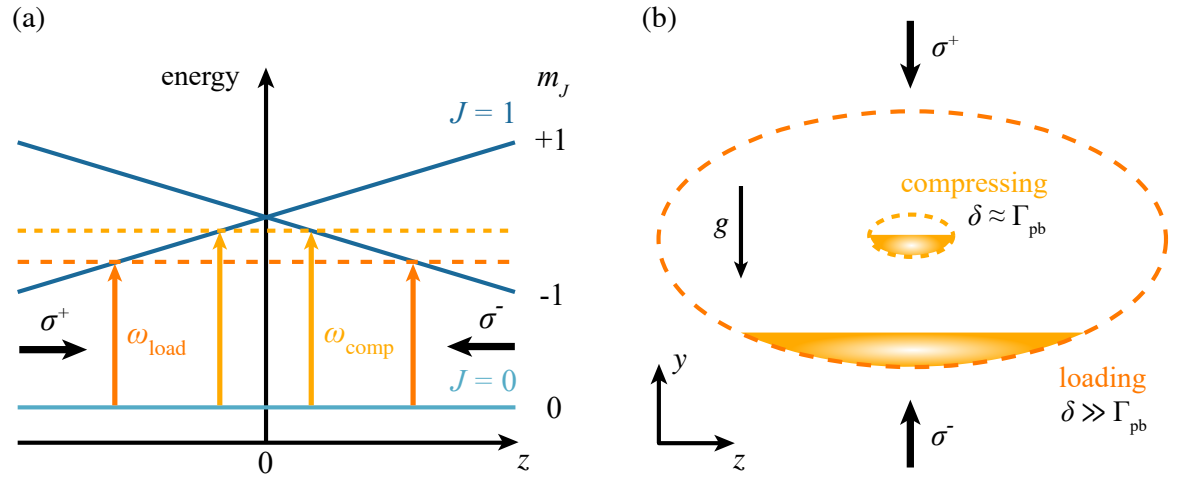

Fig. 2.4: Magneto-optical trap. (a) Operation principle of a magneto-optical trap in one dimension. σ^+ polarized light preferably excites atoms to the $m_J = +1$ state on the left side ($z < 0$) of the MOT, and vice versa σ^- polarized light preferably excites atoms to the $m_J = -1$ state on the right side ($z > 0$). Note that the $J = 1$, $m_J = 0$ level is not shown here. Overall the atoms experience a spontaneous force in direction to the MOT center region located at $z = 0$, however due to the narrow linewidth of the cooling light, this is for the one-dimensional case only true inside small regions around the illustrated arrows. After a loading phase with a somewhat larger red-detuned light several linewidths away from resonance (orange level with ω_{load}), the MOT is compressed in position space by reducing the detuning (yellow level with ω_{comp}) amongst other things as discussed in Sec. 4.1.2. (b) For detunings δ much larger than the power broadened transition linewidth $\Gamma_{\text{pb}} = \Gamma\sqrt{1+s}$ atoms experience a spontaneous force only in regions far away from the MOT center, similar to the case in (a), described in three dimensions by an ellipsoid. Atoms inside the narrow-line magneto-optical trap gather in a gravitational sag due to the weak transition exerting only a force comparable to the magnitude of the gravitational force mg. A welcomed effect of this configuration is the spin-polarization of the atomic ensemble as it mostly interacts with the lower σ^- polarized MOT beam along y. After reducing the detuning correspondingly to the scheme in (a), the atomic ensemble gets spatially compressed and lifted up to the center of the MOT region, which enhances the loading efficiency into the optical dipole trap. Images modified from [71].

position y can be written as

$$F_y = \tilde{F}_y^{\text{MOT}} + F_{\text{g}} = \frac{\hbar k \Gamma}{2} \left(\frac{s}{1 + s' + \frac{4(\delta + k v_y - \tilde{\mu} \partial_y B y/\hbar)^2}{\Gamma^2}} \right) - mg, \tag{2.21}$$

where m is the mass of an atom, g is the gravitational acceleration, and s' is an adjusted saturation parameter accounting for the beams in the other axes. Here the effective detuning $\delta - \tilde{\mu} \partial_y B y/\hbar$ stays constant, as for different light detunings δ the position y adjusts accordingly, meaning that dampening and diffusion processes, as well as equilibrium parameters of the atomic ensemble do not depend on δ. The equilibrium time τ_{eq} of the far-detuned MOT, a characteristic time length for the decrease of kinetic energy of the trapped atoms, can be expressed as

$$\tau_{\text{eq}} = \frac{m R^2 s}{4 \hbar k^2 \sqrt{Rs - s - 1}} \tag{2.22}$$

and the equilibrium temperature of the far-detuned loading MOT can be defined as

$$T_{\mathrm{eq}} = \frac{\hbar\Gamma\sqrt{s}}{2k_{\mathrm{B}}}\frac{R}{2\sqrt{R-2/s}}, \tag{2.23}$$

where $R = \hbar k\Gamma/(2mg)$, so that experimentally τ_{eq} and T_{eq} are only dependent on the saturation parameter s. For typical experimental parameters of the loading MOT, $T_{\mathrm{eq,load}}$ should lie in the region of 17 μK, while $\tau_{\mathrm{eq,load}}$ should amount to approximately 110 ms. After compressing, the values change for the equilibrium temperature to a few μK, concordantly with the Doppler temperature of 4.6 μK of the narrow-line transition, and for the equilibrium time to approximately 15 ms respectively, as the intensity of the MOT light is ramped down significantly during the compression phase (cf. Fig. 4.1). The maximum capture velocity of the far-detuned MOT can also be estimated via

$$v_{\mathrm{cap}}^{\mathrm{MOT}} = \frac{d}{\tau_{\mathrm{eq}}}, \tag{2.24}$$

where d is the diameter of the MOT light beams. With $d = 36$ mm one arrives at $v_{\mathrm{cap}}^{\mathrm{MOT}} = 3.3$ m/s, illustrating the need of a well-adjusted Zeeman slower. After loading atoms from the Zeeman slowed atomic beam into the far-detuned MOT, the MOT is subsequently compressed via changes of detuning δ and the magnetic field gradient $\partial_y B$ to achieve a much better overlapping with – and therefore increased loading into – the optical dipole trap used in the next experimental step. Details about the experimental MOT compression process can be found in Sec. 4.1.2.

2.3.3 Single and hybrid crossed optical dipole traps

To circumvent temperature and density limits of atom traps based on optical cooling techniques and ultimately reach quantum degeneracy, the atomic ensemble has to be transferred (or loaded) into other types of traps with high coherence times capable of performing evaporative cooling. Two of those types are magnetic traps and optical dipole traps, from which the latter is employed in this experiment and theoretically discussed in this section. An optical dipole trap is generally a laser field configuration with at least one point of stable equilibrium for the atomic motion, so that a mean restoring force is exterted on the atoms if they should be displaced from that point of stability. As this thesis describes the transition from a single optical dipole trap (SODT) to a hybrid crossed optical dipole trap (HCODT), both geometries, including trap depths and trap frequencies, are here studied and in Sec. 4.2 experimentally compared, respectively. The theoretical description follows [48, 97].

Dipole trap potential and scattering rate

Far-detuned light can induce an electric dipole moment in particles that then in turn interacts with the light field, leading to a so-called dipole force acting upon the particles. In the presence of an ac electric field $\mathbf{E}(\mathbf{r},t) = \hat{\mathbf{e}}\widetilde{E}(\mathbf{r})e^{-i\omega t}$ of amplitude $\widetilde{E}(\mathbf{r})$ and frequency ω according to the oscillator model the dipole moment $\mathbf{d}_{g,e}(\mathbf{r},t) = \hat{\mathbf{e}}\widetilde{d}_{g,e}(\mathbf{r})e^{-i\omega t}$ is induced on an atom, with $\hat{\mathbf{e}}$ being the unit polarization vector, and g and e denoting the ground state and excited state of the atom, respectively. Electric field amplitude and dipole moment are related via

$$\widetilde{d}_{g,e}(\mathbf{r}) = \alpha(\omega)\widetilde{E}(\mathbf{r}), \tag{2.25}$$

where $\alpha(\omega)$ is the frequency-dependent complex polarizability. The interaction or dipole potential can be expressed with the field intensity $I(\mathbf{r}) = 2\epsilon_0 c|\widetilde{E}(\mathbf{r})|^2$ as

$$U_{\mathrm{dip}}(\mathbf{r},\omega) = -\frac{1}{2}\langle \mathbf{d}_{g,e}(\mathbf{r},\omega)\mathbf{E}(\mathbf{r},\omega)\rangle = -\frac{1}{2\epsilon_0 c}\,\mathrm{Re}[\alpha(\omega)]I(\mathbf{r}). \tag{2.26}$$

As the potential is proportional to the light intensity, e.g. a red-detuned focused laser beam can be used for trapping cold atoms. The photon scattering rate is given by

$$\Gamma_{\mathrm{dip}}(\mathbf{r},\omega) = \frac{\langle \dot{\mathbf{d}}_{g,e}(\mathbf{r},\omega)\mathbf{E}(\mathbf{r},\omega)\rangle}{\hbar\omega} = \frac{1}{\hbar\epsilon_0 c}\,\mathrm{Im}[\alpha(\omega)]I(\mathbf{r}). \tag{2.27}$$

Here the imaginary part of the complex polarizability $\mathrm{Im}[\alpha(\omega)]$ relates to the number of phase-shifted dipole oscillations. As scattering events, i.e. absorption and emission cycles, and therefore heating processes take place, the atoms inside an optical dipole trap have a finite lifetime, which for a given atomic species is dependent on intensity and frequency of the light. The damping rate Γ_{d}, that describes to the spontaneous decay rate of the excited level $|e\rangle$ into the ground state $|g\rangle$, can be calculated by looking at the corresponding dipole matrix element μ via

$$\Gamma_{\mathrm{d}} = \frac{\omega_0^3}{3\pi\epsilon_0\hbar c^3}|\langle e|\mu|g\rangle|^2. \tag{2.28}$$

Optical dipole trapping of erbium atoms

The above discussion of the dipole trap potential implied an atomic two-level system consisting of a ground state and an excited state. In reality atoms possess multi-level structures, which for e.g. the erbium case can be highly complex, so that this idealization does not necessarily hold anymore as in general the dipole potential can depend on the substate of the atom, which e.g. can lead to laser light polarization dependencies. We first discuss a multi-level atom without degeneracy, after which the multi-level case with degeneracy follows. The effect of off-resonant laser light acting on atomic levels can be described using second-order perturbation theory. In a dressed states approach, the energy shift ΔE_i of state i stemming from a perturbation Hamiltonian $H_{\mathrm{int}} = -\hat{\mu}\cdot\mathbf{E}$, with eletric dipole operator $\hat{\mu}$, can be written as [98]

$$\Delta E_i = \sum_{j\neq i}\frac{|\langle j|H_{\mathrm{int}}|i\rangle|^2}{E_i - E_j}. \tag{2.29}$$

A dressing of the states with unperturbed energies E_i of the i-th state is applied by considering the overall system consisting of atom plus laser light field. Here $E_i = n\hbar\omega$ is the ground state energy that is fully provided by the laser field's energy as the internal ground state energy

amounts to zero. Photon absorption leads to an internal energy of $\hbar\omega_j$ of the excited atom and a field energy of $(n-1)\hbar\omega$, respectively. This results in the energy difference of states being $\hbar\Delta_{ij} = E_i - E_j = \hbar(\omega - \omega_j)$, and with Eq. 2.28 one arrives for a two-level system at the simplified expression

$$\Delta E = \pm\frac{|\langle e|\mu|g\rangle|^2}{\Delta_{eg}}|E|^2 = \pm\frac{3\pi c^2}{2\omega_0^3}\frac{\Gamma_\mathrm{d}}{\Delta_{eg}}I(\mathbf{r}), \tag{2.30}$$

which is known as the ac Stark shift, where the $\pm$ signs relate to the ground and excited state, respectively [99, 100]. Here $\Delta_{eg} = \omega - \omega_0$ is the light detuning from the atomic resonance frequency ω_0 of the two-level system. For low light saturation intensities the atoms mostly occupy the ground state, so that the ac Stark shifted ground state becomes the relevant dipole potential for the movement of the atoms.

When an electronic substructure is considered, one has to sum over all possible excited states $|e_j\rangle$ for a given ground state $|g_i\rangle$. For this the dipole matrix elements $\mu_{ij} = \langle e_j|\mu|g_i\rangle$ of the corresponding transitions have to be calculated, with specific transition elements

$$\mu_{ij} = c_{ij}||\mu||, \tag{2.31}$$

where $||\mu||$ is the reduced dipole matrix element which is dependent on the electronic orbital wavefunctions and can be expressed via Eq. 2.28. Here c_{ij} are the real transition coefficients, which define the coupling strength between sublevels i and j, and are dependent on the polarization of the trapping light as well as on the electronic and nuclear angular momenta, respectively. Considering Eq. 2.28, Eq. 2.29 and Eq. 2.31, the dipole potential for a ground state i in the case of large detunings and negligible saturation results as

$$U_{\mathrm{dip},i}(\mathbf{r},\omega) = -\sum_j \frac{3\pi c^2}{2\omega_j^3}\left(\frac{c_{ij}^2\Gamma_j}{\omega_j - \omega} + \frac{c_{ij}^2\Gamma_j}{\omega_j + \omega}\right)I(\mathbf{r}), \tag{2.32}$$

where ω_j is the resonance frequency, and Γ_j the damping rate respectively, for a transition from $|g_i\rangle$ to $|e_j\rangle$. For absolute values of detunings much smaller than the resonance frequency, i.e. $|\Delta_{ij}| \ll \omega_j$, the second so-called counter-rotating term inside the parentheses can be neglected within the scope of the rotating wave approximation. Importantly, for blue-detuned light with $\omega > \omega_j$ the potential is positive, and for red-detuned light with $\omega < \omega_j$ negative, respectively. With red-detuned light a dipole force in direction of maximum intensity is created, which presents a viable setting for a focused laser beam trap. For blue-detuned light the dipole force pushes particles out of regions with high intensity. The scattering rate is given by

$$\Gamma_{\mathrm{dip},i}(\mathbf{r},\omega) = \sum_j \frac{3\pi c^2}{2\hbar\omega_j^3}\left(\frac{\omega}{\omega_j}\right)^3\left(\frac{c_{ij}^2\Gamma_j}{\omega_j - \omega} + \frac{c_{ij}^2\Gamma_j}{\omega_j + \omega}\right)^2 I(\mathbf{r}), \tag{2.33}$$

where again the rotating wave approximation can be applied for $|\Delta_{ij}| \ll \omega_j$, eliminating the second counter-rotating term inside the parentheses.

Quasi-electrostatic optical dipole trapping

For the special case of very far-detuned laser light with $\omega \ll \omega_0$, as it is the case for CO_2 laser light at 10.6 μm wavelength used in this experiment as the beam of the SODT and the main beam of the HCODT respectively, the light field oscillates very slowly in respect to the atomic eigenfrequency. In this limit the induced dipole moment can follow the electric field essentially without a phase shift, i.e. statically. The rotating wave approximation as mentioned above is in this case not valid, however as now for e.g. the two-level case the approximation $\omega_0 - \omega \approx \omega_0 + \omega \approx \omega_0$ holds, a quasi-electrostatic expression can be found for a simplified dipole potential according to

$$U_{\mathrm{dip}}^{\mathrm{quest}}(\mathbf{r}) = -\frac{3\pi c^2}{\omega_0^3}\frac{\Gamma_d}{\omega_0} I(\mathbf{r}), \tag{2.34}$$

that is independent of ω. In general for the quasi-electrostatic approximation in the limit of $\omega \to 0$ the potential can also be expressed with the static polarizability $\alpha_{\mathrm{stat}} \to \alpha(0)$ as

$$U_{\mathrm{dip}}^{\mathrm{quest}}(\mathbf{r}) = -\alpha_{\mathrm{stat}} \frac{I(\mathbf{r})}{2\epsilon_0 c}. \tag{2.35}$$

In contrast to the treatment before the shifted potential for excited states is now also attractive. One advantage of such potentials is that even different atomic species and molecules could be simultaneously trapped independent of their internal state [101, 102], as the trap depth in Eq. 2.35 does not reference any specific transition frequency. Another advantage is the very small scattering rate obtainable due to the very large detuning from any atomic resonance. It can be calculated from its relation to the dipole potential as

$$\Gamma_{\mathrm{dip}}^{\mathrm{quest}}(\mathbf{r}, \omega) = 2\left(\frac{\omega}{\omega_0}\right)^3 \frac{\Gamma_d}{\hbar\omega_0} U_{\mathrm{dip}}^{\mathrm{quest}}(\mathbf{r}). \tag{2.36}$$

Typical scattering rates lie in the order of $10^{-3}\,\mathrm{s}^{-1}$ [103] with recoil energies of approximately $k_{\mathrm{B}} \cdot 1\,\mathrm{nK}$, so that a conservative trap with negligible decoherence effects by photon absorption can be realized. For such low scattering rates, the lifetime of the atoms will almost exlusively result from collisions with the background gas in the ultra-high vacuum chamber.

Atomic polarizabilities

As erbium is a multi-level atom with a rich electronic spectrum, Eq. 2.32 has to be applied. One can, however, express the dipole trap potential for an atom in a state with J and m_J by inserting the transition coefficients into that equation so that the atomic transition properties are captured in the atomic scalar α_{scal}, vector α_{vect}, and tensor polarizability α_{tens}, respectively, and parameters of the light field polarization are explicitely set via

$$\begin{aligned} U_{\mathrm{dip}}(\mathbf{r}, \omega, \mathcal{A}, \theta_k, \theta_p) = \frac{I(\mathbf{r})}{2\epsilon_0 c}\Bigg(& \mathrm{Re}\left[\alpha_{\mathrm{scal}}(\omega)\right] + \mathcal{A}\cos(\theta_k)\frac{m_J}{2J}\mathrm{Re}\left[\alpha_{\mathrm{vect}}(\omega)\right] \\ & + \frac{3m_J^2 - J(J+1)}{J(2J-1)} \cdot \frac{3\cos^2(\theta_p) - 1}{2}\mathrm{Re}\left[\alpha_{\mathrm{tens}}(\omega)\right]\Bigg), \end{aligned} \tag{2.37}$$

where $\mathcal{A}$ is the ellipticity parameter describing the polarization state of the light [75]. Here θ_k is the angle between quantization axis z and wavevector $\mathbf{k}$, and θ_p is chosen so that $|\hat{\mathbf{e}} \cdot \mathbf{e_z}| = \cos^2(\theta_p)$, where $\hat{\mathbf{e}}$ is the unit polarization vector. The scattering rate can be obtained by replacing all instances of $\mathrm{Re}\,[\alpha_\mathrm{i}(\omega)]$ in Eq. 2.37 with $\mathrm{Im}\,[\alpha_\mathrm{i}(\omega)]$. The values of the ground state erbium polarizabilities for both the CO_2 laser light main dipole trap beam at $\lambda = 10.6\,\mu$m (equaling $943.4\,\mathrm{cm}^{-1}$) as well as the Nd:YAG laser light cross dipole trap beam at $\lambda = 1064\,$nm (corresponding to $9398.5\,\mathrm{cm}^{-1}$) are given in Tab. 2.4.

	$\omega\,[\mathrm{cm}^{-1}]$		
Polarizability [a.u.]	0	943.40	9398.50
$\mathrm{Re}\,[\alpha_\mathrm{scal}]$	141	141	164
$\mathrm{Re}\,[\alpha_\mathrm{vect}]$	0	-0.084	-0.943
$\mathrm{Re}\,[\alpha_\mathrm{tens}]$	-2.52	-2.53	-3.93
$\mathrm{Im}\,[\alpha_\mathrm{scal}]\,/10^{-6}$	1.51	1.52	2.34
$\mathrm{Im}\,[\alpha_\mathrm{vect}]\,/10^{-6}$	0	-0.129	-1.74
$\mathrm{Im}\,[\alpha_\mathrm{tens}]\,/10^{-6}$	-0.421	0.421	-0.69

Tab. 2.4: Theoretical polarizability values of ground state erbium atoms at different light frequencies in atomic units of $4\pi\epsilon_0 a_0^3$ [55, 75], which especially for the scalar polarizability were experimentally verified to good agreement in [104]. Here values for the CO_2 laser light at $\omega = 943.40\,\mathrm{cm}^{-1}$ and the Nd:YAG laser light at $\omega = 9398.50\,\mathrm{cm}^{-1}$ are shown. The electrostatic case is depicted in the column with $\omega = 0\,\mathrm{cm}^{-1}$. The values for the imaginary part of the polarizability for the case of $\omega = 9398.50\,\mathrm{cm}^{-1}$ have to be taken with a pinch of salt, since due to the $(\omega/\omega_0)^3$ scaling of the phase-space factor, which possibly has not been taken into account, smaller values for the scattering rate are expected here.

For the case of the CO_2 laser light the frequency lies far below all atomic transition frequencies, as seen in Fig. 2.1 where the lowest excited state is located at energies of about $5000\,\mathrm{cm}^{-1}$, so that static and scalar polarizability are almost equal, with $\mathrm{Re}\,[\alpha_\mathrm{stat}] \approx \mathrm{Re}\,[\alpha_\mathrm{scal}(0)] = \mathrm{Re}\left[\alpha_\mathrm{scal}(943.4\,\mathrm{cm}^{-1})\right] = 141$, whereat this isotropic behaviour of the polarizability in the ground state seems to be a result of the completely filled $6s$ shell [75]. As the value for the scalar polarizability is much greater than all other contributions, the dipole potential in Eq. 2.35 can be well approximated by setting $\mathrm{Re}\,[\alpha_\mathrm{stat}] = \mathrm{Re}\,[\alpha_\mathrm{scal,CO_2}]$. It should be noted that vector and tensor polarizabilities can reach values comparable to α_stat for wavelengths associated with transitions of the incompletely filled submerged shell.

In comparison for the case of Nd:YAG laser light near $\lambda = 1.064\,\mu$m wavelength the polarizability values differ from the static case, although here $\mathrm{Re}\,[\alpha_\mathrm{scal}]$ also is the dominant quantity, so that the Nd:YAG light contribution to the overall dipole potential of the crossed trap hardly depends on the light polarization or atomic quantization axis, too, so that in good approximation Eq. 2.35 can be written with the replacement $\mathrm{Re}\,[\alpha_\mathrm{stat}] \to \mathrm{Re}\,[\alpha_\mathrm{scal,YAG}]$. On the other hand the imaginary parts of scalar, vector, and tensor polarizability respectively especially for the laser light near $\lambda = 1.064\,\mu$m wavelength are of the same order of magnitude so that the light polarization and atomic quantization axis have a strong influence on the scattering rate. A linear polarization of the dipole trapping beams seems to achieve longer

trap lifetimes [75].

Single optical dipole trap geometry

There are various dipole trap geometries feasible for capturing neutral atoms, with classic setups for red-detuned light being single focused Gaussian beam traps, crossed Gaussian beam traps, and standing wave traps [105–107]. From those mentioned the first two configurations are employed in this experiment and compared within this thesis. Starting with the simplest single Gaussian beam configuration, the intensity profile of such a beam propagating along z can be described as

$$I(r,z) = \frac{2P}{\pi w^2(z)} \exp\left(2\frac{r^2}{w^2(z)}\right), \tag{2.38}$$

where P is the beam power, and the radial coordinate $r = \sqrt{x^2+y^2}$ is the distance from the z axis, with y being the direction of gravity. The $1/e^2$ beam radius along z is given as

$$w(z) = w_0\sqrt{1+\left(\frac{z}{z_\mathrm{R}}\right)^2}, \tag{2.39}$$

where $\sqrt{2}w_0$ is the beam radius at which the Rayleigh length $z_\mathrm{R} = \pi\omega_0^2/\lambda$ is reached [108], which results for typical dipole trapping light wavelengths in the spatial confinement being in radial direction much stronger than in the axial direction. With Eq. 2.35 one obtains the dipole trap potential in the quasi-electrostatic case for the CO_2 laser beam as

$$U_\mathrm{dip}^\mathrm{quest}(r,z) = -\frac{\alpha_\mathrm{stat}}{2\epsilon_0 c}\frac{2P}{\pi w^2(z)} e^{-2r^2/w^2(z)}, \tag{2.40}$$

and the maximum trap potential depth as

$$U_0 = -U_\mathrm{dip}^\mathrm{quest}(r=0,z=0) = \frac{\alpha_\mathrm{stat}}{2\epsilon_0 c}\frac{2P}{\pi w_0^2} = \frac{\alpha_\mathrm{stat}}{2\epsilon_0 c} I_0, \tag{2.41}$$

where $I_0 = I(r=0,z=0)$ is the maximum intensity at the center of the Gaussian beam waist. For thermal energies $k_\mathrm{B}T$ of the atomic ensemble much smaller than the trap potential depth U_0, the spatial extent of the ensemble in radial direction is small compared to the beam waist, and in axial direction small compared to the Rayleigh range, respectively, so that the trap potential can be approximated as a cylindrically symmetric harmonic oscillator potential by means of a Taylor expansion around $z=0$ and $r=0$ up to second order, leading to

$$U_\mathrm{dip}^\mathrm{quest}(r,z) \approx -U_0\left(1-2\left(\frac{r}{w_0}\right)^2-\left(\frac{z}{z_R}\right)^2\right) \tag{2.42a}$$

$$= -U_0 + \frac{1}{2}m\omega_r^2 r^2 + \frac{1}{2}m\omega_z^2 z^2. \tag{2.42b}$$

The corresponding oscillator (or trap) frequencies, with which the atoms move inside the single beam optical dipole potential, are then found in the radial case as

$$\omega_r = \sqrt{\frac{4U_0}{mw_0^2}} = \omega_z \frac{\sqrt{2}\pi w_0}{\lambda}, \tag{2.43}$$

and in the axial (or longitudinal) case as

$$\omega_z = \sqrt{\frac{2U_0\lambda^2}{m\pi^2 w_0^4}} = \sqrt{\frac{2U_0}{mz_\mathrm{R}^2}}. \tag{2.44}$$

As seen in Sec. 3.4.2, measurements of the trap frequencies are crucial for the calculation of the phase space density inside the trap. Be it that an elliptic beam profile is prevalent one has to consider two different beam waists $w_{0,h}$ in horizontal and $w_{0,v}$ in vertical direction respectively, and their corresponding radial trap frequencies, as well as a modified axial trap frequency via an effective Rayleigh length [109]. For a not too large ellipticity, the beam waist can be approximated by $\tilde{w}_0 = \sqrt{w_{0,h} w_{0,v}}$.

Hybrid crossed optical dipole trap geometry

In this section properties of a hybrid crossed optical trap are discussed. The general idea is to increase the spatial confinement in each direction as single beam trapping can suffer from weak confinement in axial direction. The hybrid trap here consists of a Gaussian main dipole trap beam provided by a CO_2 laser with wavelength $\lambda = 10.6\,\mu$m, aligned in z-direction, and a Gaussian secondary dipole trap beam provided by a Nd:YAG laser with wavelength $\lambda = 1064\,$nm, which crosses the main trap beam at an angle of $67.5\,^\circ$ and is adjusted in a way so that the central regions of both the respective beam waists overlap, s. Fig. 2.5. For maximum confinement a crossing angle of $90\,^\circ$ would be optimal, however this was in the present work technically not possible due to the available vacuum chamber setup. Characteristic properties of the two trapping beams are listed in Tab. 2.5 and 2.6. As the two individual potentials are additive, the complete spatial profile of the hybrid crossed optical dipole trap potential can be described as

$$\begin{aligned} U_\mathrm{dip}^\mathrm{cross}(x,y,z) &= U_\mathrm{YAG}(x,y,z) + U_{\mathrm{CO}_2}(x,y,z) \\ &= \frac{U_{0,\mathrm{YAG}} w_{0,\mathrm{YAG}}^2}{w_\mathrm{YAG}^2(x,z)} \exp\left(-2\frac{(x\cos(3\pi/8) + z\sin(3\pi/8))^2 + y^2}{w_\mathrm{YAG}^2(x,z)}\right) \\ &+ \frac{U_{0,\mathrm{CO}_2} w_{0,\mathrm{CO}_2}^2}{w_{\mathrm{CO}_2}^2(z)} \exp\left(-2\frac{x^2+y^2}{w_{\mathrm{CO}_2}^2(z)}\right). \end{aligned} \tag{2.45}$$

For a perfect overlap of the beam waists of both beams, the maximum trap depth can be obtained by just adding the individual maximum trap depths of the beams, as $U_{0,\mathrm{dip}}^\mathrm{cross} = U_{0,\mathrm{YAG}} + U_{0,\mathrm{CO}_2}$. A Taylor expansion of Eq. 2.45 for the potential near the trap bottom, i.e. around $x = y = z = 0$, leads to

$$
\begin{aligned}
U_{\mathrm{dip}}^{\mathrm{cross}}(x,y,z) \approx\ & U_{0,\mathrm{CO_2}} + U_{0,\mathrm{YAG}} \\
& - \left(\frac{2U_{0,\mathrm{CO_2}}}{w_{0,\mathrm{CO_2}}^2} + \frac{2\cos^2(3\pi/8)U_{0,\mathrm{YAG}}}{w_{0,\mathrm{YAG}}^2} + \frac{\sin^2(3\pi/8)U_{0,\mathrm{YAG}}}{z_{\mathrm{R,YAG}}^2} \right) x^2 \\
& - \left(\frac{2U_{0,\mathrm{CO_2}}}{w_{0,\mathrm{CO_2}}^2} + \frac{2U_{0,\mathrm{YAG}}}{w_{0,\mathrm{YAG}}^2} \right) y^2 \\
& - \left(\frac{U_{0,\mathrm{CO_2}}}{z_{\mathrm{R,CO_2}}^2} + \frac{2\sin^2(3\pi/8)U_{0,\mathrm{YAG}}}{w_{0,\mathrm{YAG}}^2} + \frac{\cos^2(3\pi/8)U_{0,\mathrm{YAG}}}{z_{\mathrm{R,YAG}}^2} \right) z^2.
\end{aligned}
\tag{2.46}
$$

From this the total trap frequencies of the hybrid crossed optical dipole trap in x-, y-, and z-direction respectively are determined as

$$
\omega_x = 2\sqrt{\frac{U_{0,\mathrm{CO_2}}}{m w_{0,\mathrm{CO_2}}^2} + \frac{\cos^2(3\pi/8)U_{0,\mathrm{YAG}}}{m w_{0,\mathrm{YAG}}^2} + \frac{\sin^2(3\pi/8)U_{0,\mathrm{YAG}}}{2m z_{\mathrm{R,YAG}}^2}} \tag{2.47a}
$$

$$
\omega_y = 2\sqrt{\frac{U_{0,\mathrm{CO_2}}}{m w_{0,\mathrm{CO_2}}^2} + \frac{U_{0,\mathrm{YAG}}}{m w_{0,\mathrm{YAG}}^2}} \tag{2.47b}
$$

$$
\omega_z = \sqrt{\frac{2U_{0,\mathrm{CO_2}}}{m z_{\mathrm{R,CO_2}}^2} + \frac{\sin^2(3\pi/8)U_{0,\mathrm{YAG}}}{m w_{0,\mathrm{YAG}}^2} + \frac{2\cos^2(3\pi/8)U_{0,\mathrm{YAG}}}{m z_{\mathrm{R,YAG}}^2}}. \tag{2.47c}
$$

The smallest trap frequency for a given setup corresponds to the weakest confinement in that spatial axis. Note that due to the use of two different wavelengths for the trapping beams, interference effects on the optical dipole potential can be neglected here. Those are present for crossed beams of the same wavelength, which often is an unwanted effect that, however, can be mitigated by detuning one of the trap beams, but can also be utilizied for e.g. investigations of Raman or sideband cooling [110, 111].

Exp. values	Nd:YAG laser trap	CO_2 laser trap
$\lambda\,[\mu\mathrm{m}]$	1.064	10.6
$\alpha_{\mathrm{stat}}\,[4\pi\epsilon_0 a_0^3]$	164	141
$w_0\,[\mu\mathrm{m}]$	55.6	36.2
$P_{\mathrm{init}}\,[\mathrm{W}]$	1.59	72.6
Propagation in (z,x) plane	$\left(\cos\left(\frac{3\pi}{8}\right), -\sin\left(\frac{3\pi}{8}\right)\right)$	(1,0)

Tab. 2.5: Experimental values for the CO_2 and Nd:YAG laser beams, respectively. The static polarizabilities α_{stat} are fixed by choice of the laser wavelengths λ. Experimental quantities that can be controlled are the beam waists w_0, initial beam powers P_{init} and propagation pathways. Beam waists were measured in [97].

2.3.4 Evaporative cooling

Phase space densities of atomic ensembles captured in magneto-optical traps or in optical dipole traps directly after loading are generally to small to reach Bose-Einstein condensation.

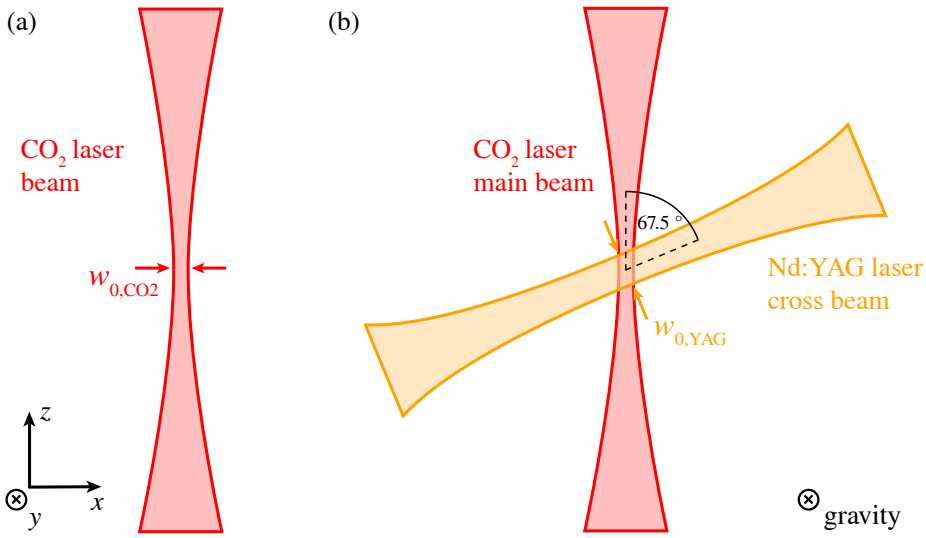

Fig. 2.5: (a) Sketch of the single (SODT) and (b) hybrid crossed optical dipole trap (HCODT) geometry, respectively. For the HCODT the Gaussian secondary Nd:YAG laser beam crosses the Gaussian CO_2 laser main beam at an angle of 67.5 °. Here gravity points into the drawing plane. Characteristic values of the two trapping beams can be found in Tab. 2.5 and 2.6.

Theo. geometry	Nd:YAG laser trap	CO_2 laser trap
Beam waist	$w_{0,\mathrm{YAG}}\sqrt{1+\left(\frac{z\cos\frac{3\pi}{8}-x\sin\frac{3\pi}{8}}{z_{\mathrm{R,YAG}}}\right)^2}$	$w_{0,\mathrm{CO_2}}\sqrt{1+\left(\frac{z}{z_{\mathrm{R,CO_2}}}\right)^2}$
$U(x,y,z)$	$\frac{U_{0,\mathrm{YAG}}w_{0,\mathrm{YAG}}^2}{w_{\mathrm{YAG}}^2(x,z)}\exp\left(-2\frac{(x\cos\frac{3\pi}{8}+z\sin\frac{3\pi}{8})^2+y^2}{w_{\mathrm{YAG}}^2(x,z)}\right)$	$\frac{U_{0,\mathrm{CO_2}}w_{0,\mathrm{CO_2}}^2}{w_{\mathrm{CO_2}}^2(z)}\exp\left(-2\frac{x^2+y^2}{w_{\mathrm{CO_2}}^2(z)}\right)$

Tab. 2.6: Theoretical geometry, i.e. calculated beam waists and dipole trap potentials, for two Gaussian trapping beams with different wavelength and propagation pathways chosen as in Tab. 2.5 and shown in Fig. 2.5.

To reduce the temperature of an ensemble further, the evaporative cooling technique can be employed [112]. For this the Maxwell-Boltzmann distribution gets truncated by removing atoms in the high-energy tail of the thermal distribution from the trap, followed by rethermalization of the remaining atoms via elastic collisions, leading to a velocity distribution of now smaller temperature, i.e. a colder atomic ensemble, as sketched in Fig. 2.6 [105]. That is typically achieved by lowering the optical dipole potential more and more until a satisfactory phase space density is reached. Theoretical considerations in this section follow [113].

For efficient evaporative cooling the optical dipole trap potential depth has to be lowered quickly enough so that the process does not stagnate, as a drop of temperature also reduces the rethermalization rate drastically, but slow enough so that the atoms have the chance to rethermalize at all. The efficiency of evaporative cooling is characterized by the cut-off parameter $\eta = U/(k_\mathrm{B}T)$. For very cold atoms in comparison to the potential depth, $k_\mathrm{B}T < U$, the number of colliding pairs of atoms with high enough energy for one atom to leave the trap is proportional to $e^{-\eta}$. After loading atoms into the optical dipole trap, a short period

of so-called natural evaporation in the order of seconds takes place, and latest when this effect tapers off the potential U has to be continuously lowered, if one wants to avoid a rapid decrease of the rethermalization rate. For optimal results, the lowering process should run adiabatically, and η should be kept constant. For this so-called induced evaporation one then yields a temporal evolution of the atom number as

$$\frac{N(t)}{N_{\mathrm{init}}} = \left(\frac{U(t)}{U_{\mathrm{init}}}\right)^{3/[2(\eta'-3)]}, \tag{2.48}$$

where $\eta' = \eta + (\eta-5)/(\eta-4)$ can be used in the case of an approximate harmonic potential [114]. For a constant η the temperature should change proportionally with the potential depth. Most interesting is the temporal evolution of the phase space density ρ, which can be expressed via

$$\frac{\rho(t)}{\rho_{\mathrm{init}}} = \left(\frac{U_{\mathrm{init}}}{U(t)}\right)^{3(\eta'-4)/[2(\eta'-3)]}. \tag{2.49}$$

The for the experimental implementation important temporal evolution of the trap depth can be written with help of the time constant τ_{evap} for evaporation as

$$\frac{U(t)}{U_{\mathrm{init}}} = \left(1 + \frac{t}{\tau_{\mathrm{evap}}}\right)^{-2(\eta'-3)/\eta'}, \tag{2.50}$$

where $1/\tau_{\mathrm{evap}} = 2\eta'(\eta-4)\exp(-\eta)\gamma_{\mathrm{init}}/3$ is then the rethermalization rate, and γ_{init} is the initial collision rate between atoms. As one has also to consider atom losses from the trap due to collisions with the residual background gas of the ultra-high vacuum, the replacement $t \to 1 - \exp(t \cdot \Gamma_{\mathrm{loss}})/\Gamma_{\mathrm{loss}}$, with the collision loss rate Γ_{loss}, has to be applied in Eq. 2.50.

Additionally the gravitation has to be considered, which becomes relevant for small trap depths near the end of the evaporative cooling process. The total potential acting on the atomic ensemble is then for a HCODT via Eq. 2.45 given by

$$U_{\mathrm{dip}}^{\mathrm{tot}}(x,y,z) = U_{\mathrm{dip}}^{\mathrm{cross}}(x,y,z) - mgy, \tag{2.51}$$

with g as the gravitational acceleration. Thus gravity introduces modifications to the potential, which lead to a reduced effective trap depth, as one side of the potential well gets lowered, resulting in a faster evaporation process at low trap potential depths in the order of the gravitational potential, as indicated in Fig. 2.7(b). This effect, however, can be increased by an applied magnetic field gradient adjusted so that the Stern-Gerlach force acts in the same direction as the gravitational force, which then results in an even faster evaporation process that can be tuned experimentally [115], and was first implemented in our experiment within the scope of a previous thesis [56]. The total acceleration amounts then to $a_{\mathrm{tot}} = a_{\mathrm{SG}} + g$, where $a_{\mathrm{SG}} = m_J g_J \mu_{\mathrm{B}} \partial_y B y/m$ is the Stern-Gerlach acceleration in y-direction [116], which modifies Eq. 2.51 via $g \to a_{\mathrm{tot}}$. The advantage here is that for the same effective potential depth the spatial occlusion is stronger, leading to higher phase space densities, as indicated in

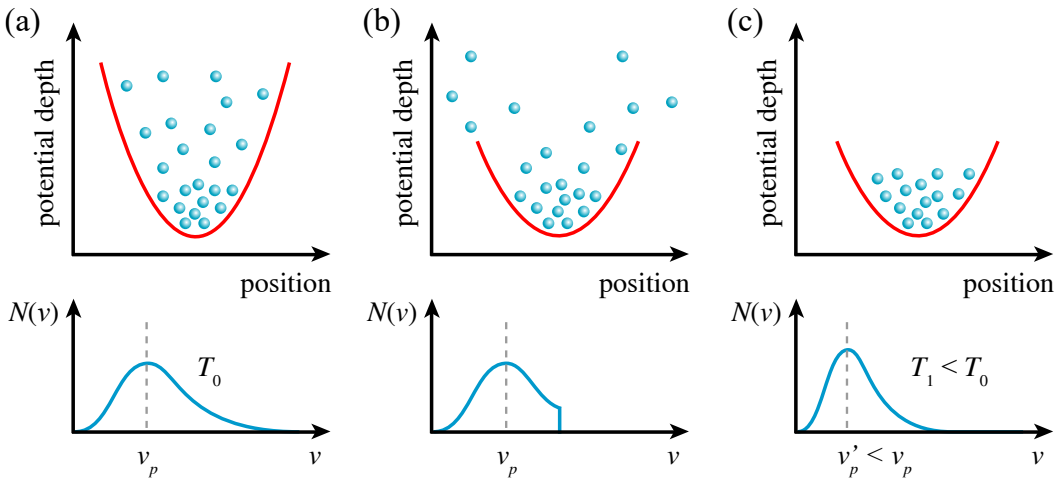

Fig. 2.6: Basic concept of induced evaporative cooling. (a) Shown is a harmonically trapped thermalized atomic ensemble with temperature T_0. In the panel below the associated Maxwell-Boltzmann velocity distribution $N(v)$ can be seen, with the most probable velocity being marked as v_p. (b) A lowered trap depth leads to an escape of atoms of highest kinetic energy, indicated as a removal of the high-energy tail of the velocity distribution. (c) Rethermalization of the remaining atoms via elastic collisions leads to a lower temperature $T_1 < T_0$ of the ensemble, with a correspondingly lower most probable velocity v_p' of an altered Maxwell-Boltzmann distribution. Image modified from [55].

Fig. 2.7(c). For calculations of trap frequencies when considering small potential trap depths, modifications by gravitation and applied magnetic field gradients have to be considered by using the effective trap depths.

For the experimental realization of an efficient evaporative cooling process all parameters are initially set according to the given experimental properties as e.g. the determined trap depth U and temperature T of the atomic ensemble inside the optical dipole trap, and are then optimized for highest phase space density at end of evaporation. More details on the implementation of the evaporation ramp for the case of the hybrid crossed optical dipole trap are given in Sec. 4.3.1.

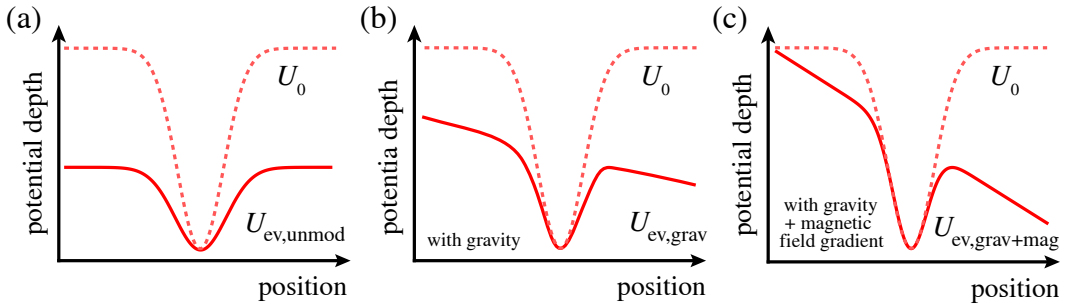

Fig. 2.7: Modification of the dipole trap potential during evaporation via gravity and applied magnetic field gradient. (a) Shown is a schematic of the trap potential for two different trap beam powers: U_0 as the primordial trap potential with maximum power P_0 before evaporation, and $U_{\mathrm{ev,unmod}}$ as the trap potential at the end of the evaporation process with a much lower power P_{ev}, here unmodified, i.e. without any influence of gravity or an applied magnetic field gradient. The spatial confinement in the bottom region of the trap potential lessens as the trap potential depth is lowered. (b) When accounting for gravity one side of the trap potential gets lifted while the other decreases, leading to a lowered effective trap depth. This effect is only noticeable for small potential depths (here $U_{\mathrm{ev,grav}}$) in the order of the gravitational potential. For effective trap depths that are comparable to the case in (a) the spatial confinement in the lower part of the potential is stronger. (c) For an additionally applied magnetic field gradient with Stern-Gerlach force pointing in the same direction as gravity, the effects discussed in (b) increase. Note that in these schematics the potential depths are not to scale.

3 Experimental setup

Here the experimental apparatus and used techniques for the generation as well as characterization of an atomic erbium Bose-Einstein condensate (BEC) are presented. The core setup consisting of the vacuum chamber including the effusion cell and Zeeman slower, as well as the blue and yellow laser light setups for optical cooling were constructed within the scope of previous works [56, 117–119], so that these topics are discussed only briefly, while more attention is paid to the updated setup of the single (SODT) and hybrid crossed optical dipole traps (HCODT), respectively.

3.1 Experimental overview

Initially erbium atoms in the metallic state are heated in an atomic beam oven to form an effusive atomic beam. A transversal cooling stage reduces its transverse velocity spread, while a Zeeman slower decelerates a portion of the atoms to sufficiently low velocities so that they can get captured by the narrow-line MOT. Once trapped inside the MOT, the trap is spatially compressed (cMOT) to achieve a higher atom transfer efficiency into the next stage: the optical dipole trap (either in SODT or HCODT configuration). After successful loading into the optical dipole trap, evaporative cooling is performed until Bose-Einstein condensation is accomplished. The whole setup described is set into an ultra-high vacuum chamber with a pressure of order of 10^{-10} mbar, leading to a lifetime in the optical dipole trap that should only be limited by collisions with residual background particles [120]. Fig. 3.4 indicates the overall setup including sketches of the laser pathways, where all components are placed onto three optical tables (with the two larger ones featuring pneumatically damped bed-plates to suppress mechanical vibrations). The light for laser cooling purposes is connected to the main table with the main vacuum chamber via optical fibers, which ensures an uncoupling of the optical setup on the main table from maintenance adjustments of the laser systems on other tables.

In this experiment the process of trapping atoms and cooling them down to quantum degeneracy followed by a measurement is performed periodically, as a) measurements are typically invasive so that the atoms are heated or even lost during that process, and b) often one experimental parameter is varied from measurement to measurement. The experimental cycle is controlled by an electronic real-time controller (*ADwin Pro II*, manufactured by *Jäger Messtechnik*) with a temporal resolution of 1 μs by delivering trigger signals and analog control signals to many experimental components as e.g. rf electronics and mechanical shutters. The experimental cycle can be customized via a graphical interface[1] on PC, which is connected by ethernet to the controller. Many measurements are done via optical imaging with the help of a camera that sends the recorded images to the PC for further analysis.

[1] Programmed by C. Geckeler in python for an *ADwin Pro* system.

3.2 Vacuum system

The stainless steel ultra-high vacuum chamber consists of an oven chamber, a Zeeman slower tube, and a main vacuum chamber, respectively, which are discussed shortly in this section. The used vacuum chamber was constructed in earlier works, with more information available in [56, 119].

The oven chamber consists of the effusion cell, the corresponding inset crucible, and a sixfold crosspiece, which is used for four purposes: optical access for transversal cooling, connection of an ion getter vacuum pump (75 L/s, supplier: *Varian*), connection of a pressure gauge (model *Ionivac*, supplier: *Oerlikon*), and connection of a valve that can be used to connect a turbo vacuum pump, and is shown in Fig. 3.1. Connections can be made via Con-Flat (CF) flanges. The crosspiece includes another 10 mm aperture to suppress atomic erbium contamination of the following acccess optics. The described oven vacuum chamber can be sealed off from the Zeeman slower tube and main vacuum chamber with the help of an ultra-high vacuum valve, so that e.g. bulk erbium can be refilled in the crucible without having to break the ultra-high vacuum in the main chamber. Typical pressures inside the oven chamber lie in the region of $2.5 \cdot 10^{-10}$ mbar.

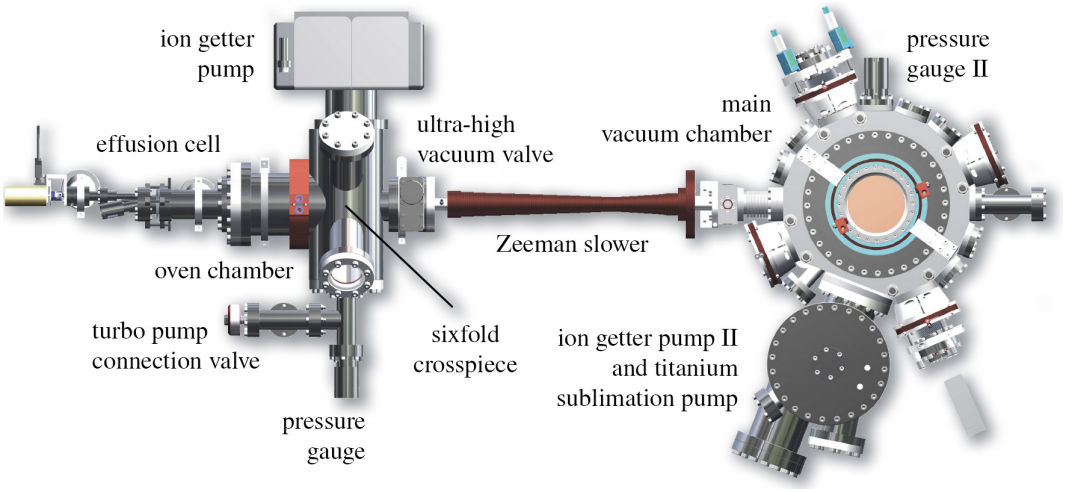

Fig. 3.1: Technical drawing of the complete ultra-high vacuum setup. Shown on the left is the oven chamber with effusion cell and sixfold crosspiece, with the transversal cooling stage built into the latter one. The oven chamber is connected with the main vacuum chamber via the Zeeman slower tube. Left of the Zeeman slower is an ultra-high vacuum valve located so that the oven chamber can be cut off from the remaining vacuum setup. In the main vacuum chamber the magneto-optical trap and optical dipole traps are set up. The ultra-high vacuum is maintained by two ion getter pumps, as well as a titanium sublimation pump, and monitored by two pressure gauges. Drawing was provided by the *Feinmechanik-Werkstatt* of the *Institut für Angewandte Physik, Bonn.*

Employed is a commercial effusion cell (model *DFC-40-10-284-SHE*, supplier: *CreaTec Fischer & Co. GmbH*), shown in Fig. 3.2(a), whose crucible gets filled with up to 25 g of metallic bulk erbium (99.99 % purity, offered by *smart-elements GmbH*) and closed with two inlets including apertures. Several components are made from tantalum, which exhibits a very high melting point of about 3300 K: the crucible, both inlet parts, the two-stage heating filaments,

and thermal isolation sheetings that surround the heating filaments. All those parts are enclosed inside a double-walled stainless steel vacuum cylinder tube which is water-cooled. With the two-stage heating configuration two different temperatures can be set along the oven, and monitored by temperature sensors, with an operation temperature in the deeper part of the effusion cell sufficient for sublimation of erbium, and a slightly higher temperature within the inlet construction (also called hot-lip) near the shutter, so that condensation of atomic erbium at the inlet apertures can be minimized. The atomic oven shutter can be used to block or release the atomic beam, with opening and closing times of about 150 ms each.

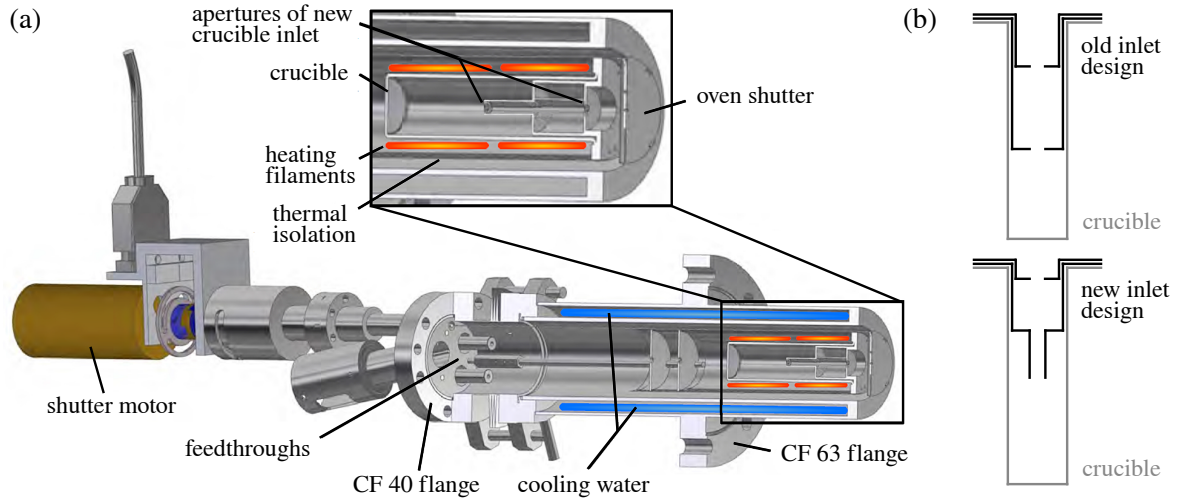

Fig. 3.2: (a) Technical drawing of the effusion cell. On the right side, the water-cooled effusion cell can be seen. The crucible is located at the front of the effusion cell, surrounded by heating filaments. An oven shutter can block or release the atomic beam fast within roughly 150 ms. Additionally electrical and mechanical feedthroughs as well as the shutter motor are sketched. The original drawing was provided by the manufacturer, modified in [56], and has been updated here for the new inlet design. (b) Due to condensation issues of atomic erbium in older crucible versions, the design had to be changed several times until a satisfactory operation without clogging of the apertures could be found, here labeled as the new inlet design.

When the bulk erbium sublimates, a vapor pressure depending on the vapor temperature T is created. With apertures a stream of fast moving, i.e. hot, atoms can be formed, where the atomic flux denotes the number of atoms that pass an area during a time interval. The higher the flux is, the higher the loading rate into the magneto-optical trap and therefore the number of trapped atoms can be [55]. A theoretical description of the atomic flux can be found in [121] and [122], with a short treatment relevant to the vacuuum setup of this experiment presented in [56]. Under the assumption that the atomic erbium vapor behaves as an ideal gas and the atoms roughly follow a Maxwell-Boltzmann distribution, the width of the velocity distribution is obtained as $\xi = \sqrt{2k_\mathrm{B}T/m}$, where k_B is the Boltzmann constant, and m is the atomic mass of erbium. For a characterization typically the mean $\bar{v} = 3\sqrt{\pi}\xi/4$ as well as the most probable velocity $v_p = \sqrt{3/2}\xi$ are given. In this thesis the oven was typically operated at a temperature of 1373 K, leading to values of $\xi = 369\,\mathrm{m/s}$, $\bar{v} = 490\,\mathrm{m/s}$, and $v_p = 452\,\mathrm{m/s}$. With such an atomic beam a magneto-optical trap can be loaded, although due to the high mean velocity $\bar{v}$ of the atoms and a much smaller capture velocity of the

magneto-optical trap of roughly $v_{\mathrm{cap}}^{\mathrm{MOT}} = 3.3\,\mathrm{m/s}$ precooling methods like Zeeman slowing, and potentially also transversal cooling, are needed.

Although efforts were made to minimize the condensation of erbium at the apertures with the two-stage heating setup, there still emerged the issue of erbium clogged-up apertures, and consequently a decreased atomic beam flux. Additionally several breakdowns of the atomic oven seemingly due to excessive sublimation of bulk erbium lead to short-circuits of the heating filaments, and malfunctioning temperature sensors and oven shutter respectively, which prompted a redesign of the crucible inlet. With a sketch of the final version shown in Fig. 3.2(b) condensation effects could be reduced to a satisfactory level. Together with a reduction of the effusion cell operation temperature to 1373 K further breakdowns could be prevented.

Between oven chamber and main chamber the Zeeman slower tube including a 60 cm long magnetic field coil segment is located, as seen in Fig. 3.1. The tube is double-walled to allow water-cooling of the attached coils. All coils are winded with double coated copper wire of 1 mm core diameter, and are attached to the tube as well as to already wrapped wire via thermally conductive glue. Coils include an offset coil, the Zeeman slower profile coil, two high current coils (for varying the maximum capture velocity of the Zeeman slower, and for varying the outcoupling velocity towards the main chamber respectively), and a compensation coil (to set the total Zeeman slower magnetic field to roughly zero at the position of the MOT).

More details about the required and eventually implemented magnetic coil profile can be found in [55], while the construction and characterization of the Zeeman slower is documented in [117]. The preparation of the Zeeman slower light is also briefly discussed in Sec. 3.3.1.

The main vacuum chamber is of flat cylindrical form with a diameter of 380 mm and a height of 100 mm, and originates from a previous ultracold potassium experiment [123] (made and modified for our purposes by *Vab Vakuum Anlagenbau GmbH*). It possesses 15 radial access drill holes, as well as one large central axial drilling of 256 mm diameter along the cylinder axis which provides the chamber volume. All access holes can be closed via CF flanges of various sizes. For most of the optical accesses 7056 glass is used, while for some silica glass is employed which provides less wavefront perturbations needed for the operation of absorption imaging and (planned) optical lattices. The optical access glasses are coated with anti-reflex coating for the used optical beams with wavelengths $\lambda = 400.91\,\mathrm{nm}$, 582.84 nm, and 1064 nm, respectively. For the CO_2 laser dipole trap beam, however, all optics have to be made from zinc selenide, which includes the corresponding viewports in the trap beam axis as well as two spherically corrected lenses (supplier: *II-VI Deutschland GmbH*). Those lenses are each mounted to one of two stainless steel tubes which themselves are each attached to a stainless steel membrane bellow. With the help of a tripod construction the lenses can be positioned inside the chamber [124]. A technical drawing including sketches of the here used optical pathways in the main vacuum chamber can be seen in Fig. 3.3.

The remaining flanges are used for another pressure probe (model *Ionivac*, supplier: *Oerlikon*), a blank flange, and a viewport for a photomultiplier typically used for calibration measurements. Both larger flanges in axial direction are closed with viewports of 122 mm

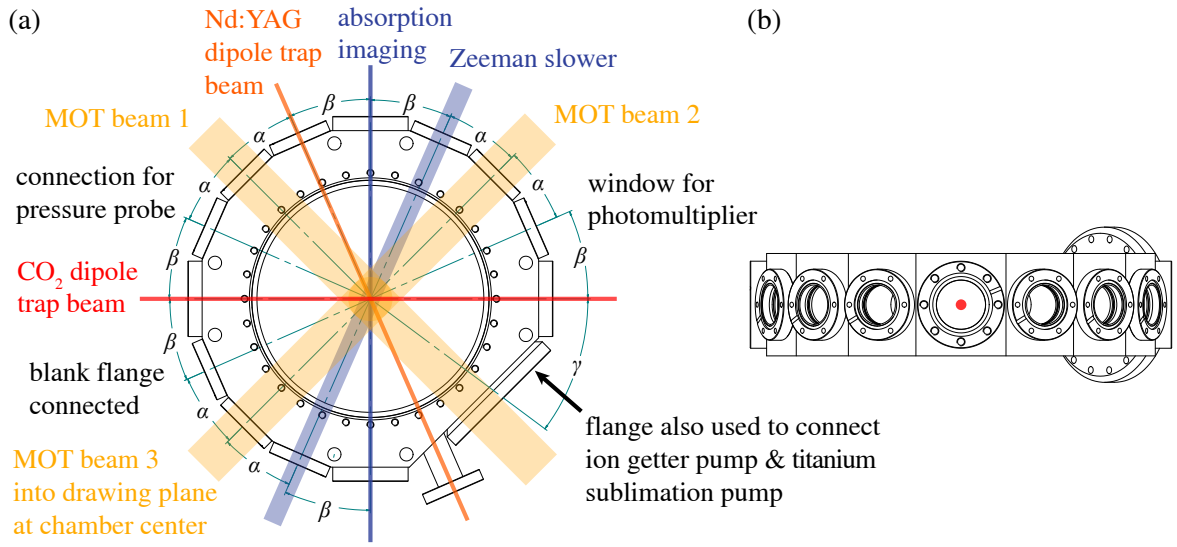

Fig. 3.3: Technical drawing of the main vacuum chamber. (a) Shown is the view from above including sketches of the optical pathways inside the chamber. Details on all optical setups can be found in the following sections. The plotted angles amount to $\alpha = 21.3\,°$, $\beta = 23.7\,°$, and $\gamma = 36.7\,°$. (b) Side view of the main chamber. The front access from this perspective is used as an entry of the CO_2 laser dipole trap beam (marked red). Modified images, with the original drawings provided by the manufacturer.

window diameter. The coils for the quadrupole magnetic field employed in the magneto-optical trap are positioned on the top (bottom) of the chamber above (below) the viewport. They can generate a magnetic field gradient of about 0.2 G/(A cm) at the center of the main chamber. Additionally there are in total six coils placed around the main chamber for the generation of offset magnetic fields in each spatial direction. Two coils in Helmholtz configuration are attached to the MOT coils that generate a homogeneous offset magnetic field of (2.7 ± 0.3) G/A at the center of the main chamber. Placed at four of the CF50 flanges (in CO_2 laser dipole trap beam and absorption imaging axis respectively, cf. Fig. 3.3(a)), two Helmholtz offset coil pairs generate magnetic fields of (0.30 ± 0.03) G/A each at the main chamber center. More details on the characterization of these magnetic field coils can be found in [119]. At the larger CF100 flange another ion getter pump (100 L/s, model *IGP*, supplier: *Schwarz Vakuumtechnik KG*), as well as a titanium sublimation pump stemming from an earlier experiment [123] are connected. The pressure inside the main chamber usually lies in the order of $1 \cdot 10^{-10}$ mbar.

3.3 Optical setup

In this section all laser systems and corresponding optical setups used in this experiment are described. Emphasis is laid on the preparation of light for the single and hybrid crossed optical dipole traps respectively. An overview of all laser systems including sketches of the optical pathways can be found in Fig. 3.4. The various laser systems are used in the following way:

- Blue laser light: transversal cooling, Zeeman slower, absorption imaging
- Yellow laser light: magneto-optical trap

- CO_2 laser light: single and hybrid crossed optical dipole trap
- Nd:YAG laser light: hybrid crossed optical dipole trap (together with CO_2 laser light)

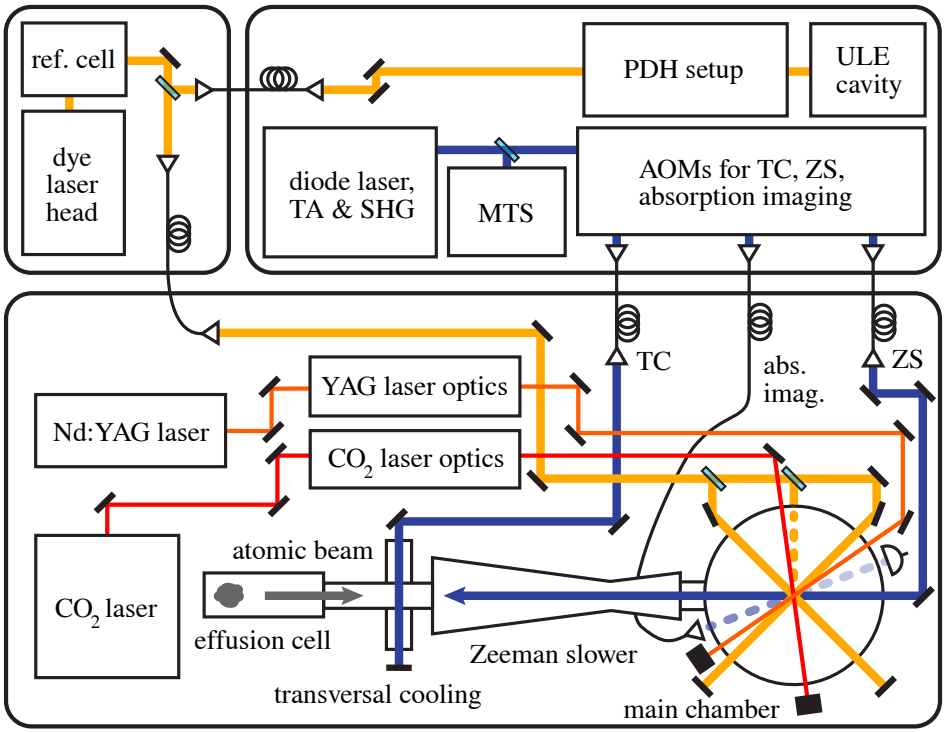

Fig. 3.4: Sketched overview of all laser systems used to generate an atomic erbium Bose-Einstein condensate. Shown in the upper left is the dye laser (consisting of head and reference cell), which is locked to an ultra low expansion (ULE) cavity via the Pound-Drever-Hall (PDH) method (upper right), and provides the yellow laser light near 582.84 nm wavelength for the magneto-optical trap. Blue light near 400.91 nm wavelength used for transversal cooling (TC), Zeeman slower (ZS) and absorption imaging respectively is provided by a diode laser whose light output is subsequently amplified via a tapered amplifier (TA) and frequency-doubled via a second-harmonic generation (SHG) cavity. The diode laser system frequency is locked with the help of modulation transfer spectroscopy (MTS). Light of both dye laser and diode laser are transferred to the main optical table via optical fibers. The CO_2 and Nd:YAG lasers used for the single and hybrid optical dipole trap respectively are already placed on the main table and are guided via optical elements to the main chamber.

3.3.1 Blue laser light setup

For transversal cooling, Zeeman slower and absorption imaging, respectively, blue laser light at 400.91 nm near the $4f^{12}6s^2\,(^3\mathrm{H}_6) \rightarrow 4f^{12}(^3\mathrm{H}_6)6s6p(^1\mathrm{P}_1)(6,1)_7$ atomic erbium transition is used, provided by a commercial diode laser consisting of a grating-stabilized laser diode, whose output at 801.82 nm is amplified via a semiconductor tapered amplifier (TA) and subsequently frequency-doubled with the help of a second-harmonic generation (SHG) ring cavity (model *DLC TA-SHG PRO*, supplier: *TOPTICA Photonics AG*), leading to a light output power near 401 nm of 1.4 W. As a result of an internal locking process the linewidth of the output light amounts to approximately 200 kHz, which is much lower than the natural linewidth of the considered atomic transition of about 29.7 MHz. However long-term frequency drifts are still larger (in the order of 2.5 MHz/min) and have to be suppressed using a stable reference.

Here the laser frequency is shifted by an acousto-optic modulator (AOM) (model *3200-125*, supplier: *Gooch & Housego PLC*) and locked to an atomic resonance of ^{168}Er by means of modulation transfer spectroscopy (MTS) [125,126] on an erbium hollow cathode lamp (model *3QQAYEr*, supplier: *Heraeus Noblelight GmbH*). The error signal stemming from the spectroscopy can be fed directly into the diode laser electronics, which then stabilizes the laser frequency against long-term drifts via the Pound-Drever-Hall technique [127]. Details on the characterization of the diode laser and the locking procedure via MTS can be found in [128].

The light for absorption imaging, Zeeman slower, and transversal cooling respectively has to be prepared before it is sent via optical fibers to the main optical table (as sketched in Fig. 3.4 in the upper right corner). For this each optical pathway includes another AOM used to appropriately shift the light frequency. As the laser light frequency is locked by MTS to a value shifted from atomic resonance by an AOM (see above), another AOM (model *3307-121*, supplier: *Gooch & Housego PLC*) employed for absorption imaging light preparation has to cancel this shift to make the probing light again approximately resonant with the atomic ensemble. After transferring the absorption imaging light to the main table via an optical fiber it propagates through the main vacuum chamber and is subsequently guided onto a camera sensor (model *5.5 sCMOS*, supplier: *Andor Technology Ltd.*) to image the shadow of the atomic cloud, as discussed in Sec. 3.4.1.

Preparation of the Zeeman slower light is done with the help of an AOM (model *3220-120*, supplier: *Crystal Technology, Inc.*) by red-shifting the light about 600 MHz ($\approx$ 20 natural linewidths) away from the atomic erbium resonance near 400.91 nm wavelength. Afterwards the shifted light is coupled into a high power optical fiber (model *aeroGUIDE-10-PM-APC*, supplier: *NKT Photonics GmbH*) and delivered to the main optical table, where the output beam with a typical power of 300 mW is widened with a telescope to a beam radius of approximately 4 mm and guided into the main chamber to counterpropagate the atomic beam axis.

Light for the transversal cooling stage is prepared with an AOM (model *3307-121*, supplier: *Gooch & Housego PLC*), red-shifting the frequency roughly 20 MHz (equaling 0.7 natural linewidths) away from atomic resonance. After transfer of the light to the main optical table via optical fiber, its transversal beam profile is transformed from a circular to an elliptical shape via a telescope consisting of cylindrical lenses to increase the interaction length of the light with the atomic beam. The beam with a power of about 80 mW is then lead into the sixfold crosspiece of the oven vacuum chamber in a way so that two counterpropagating laser beam pairs orthogonal to each other each illuminate the atomic beam transversally. More details on the light preparation and the particular transversal cooling setup can be found in [56].

3.3.2 Yellow laser light setup

Laser light near 582.84 nm wavelength is employed for the magneto-optical trap, while utilizing the $4f^{12}6s^2\,(^3\mathrm{H}_6) \rightarrow 4f^{12}(^3\mathrm{H}_6)6s6p(^3\mathrm{P}_1)(6,1)_7$ atomic erbium transition, provided by a commercial dye laser system (model *Matisse DX*, supplier: *Sirah Lasertechnik GmbH*). Here the active dye medium is Rhodamin 6G (type *Rhodamin 590 Chlorid*, supplier: *Exciton, Inc.*) solved in ethylene glycole with a mass concentration of 0.75 g/L, which is optically pumped

by a frequency-doubled Nd:YAG laser (model *Verdi G12*, supplier: *Coherent, Inc.*) with output power of 12 W at 532 nm. The dye laser system consists of a head where the light near 582.84 nm wavelength is generated from the optically pumped dye in a ring cavity, and a reference cell which is used for internal frequency stabilization via Pound-Drever-Hall (PDH) locking [127], leading to a linewidth of approximately 35 kHz. The output power amounts to roughly 1.7 W.

The output light's linewidth is smaller than the atomic transition's natural linewidth of 186 kHz, so that the laser light exhibits sufficient short term stability. However a large long-term drift of about 100 MHz per hour made it necessary to lock the frequency of the laser onto a stable reference, that additionally has to feature a linewidth in the region of the natural linewidth. Unfortunately, spectroscopy techniques as the MTS performed on a hot atomic ensemble (and successfully used for the blue light setup) are not precise enough in view of the here smaller natural linewidth, as typical frequency uncertainties lie in the region of 1 MHz due to pressure broadened transition linewidths.

For long-term frequency stabilization an external, ultra low expansion (ULE) cavity of high stability was built. The plano-spherical ULE cavity, consisting of a 150.9 mm long spacer and two mirrors, is made from an extremely temperature-insensitive glass (type *Corning ULE premium grade, Corning Code 7972*, supplier: *Corning, Inc.*) with a very small coefficient of thermal expansion of $(0 \pm 30) \cdot 10^{-9}\,\mathrm{K}^{-1}$. It is placed inside a separate vacuum chamber with pressure in the order of 10^{-8} mbar, including active (temperature stabilization) and passive (several thermal shieldings) temperature control as well as vibrations damping elements. The dye laser light is frequency-shifted by two AOMs (model *3200-125* each, supplier: *Crystal Technology, Inc.*) and then locked to an appropriately set cavity resonance peak (with cavity linewidth of (220.5 ± 1.0) kHz) via PDH technique [127]. As the daily frequency drift of the ULE cavity amounted to only (1.23 ± 0.01) kHz in 2014 (and is projected to become smaller over the years due to reduced material creep), a stable operation of the magneto-optical trap can be assured. More details on the dye laser system, the setup and characterization of the ULE cavity as well as the external laser lock can be found in [118]. Extant locking issues mentioned in that work could be resolved shortly after with the introduction of a modified hardware module from the manufacturer.

The main portion of the dye laser light output is frequency-shifted by an AOM (model *3080-125*, supplier: *Crystal Technology, Inc.*), subsequently coupled into an optical fiber and guided onto the main optical table. There a small percentage of the light is seperated for an intensity stabilization scheme. Most of the light, however, is widened with a telescope to a large beam diameter, and subsequently cut via an aperture to get a laser beam of radius of 36 mm with a nearly homogeneous intensity profile. This beam is split into three parts with the help of half-wave plates and polarizing beam splitters, which together with their retroreflected counterparts form the magneto-optical trap (MOT) and are adjusted orthogonally to each other inside the main vacuum chamber, as sketched in Figs. 3.3 and 3.4. Quarter-wave plates are put at the entry and exit viewports on each MOT axis to provide the appropriate light polarizations shown in Fig. 2.3. Details on the experimental setup of the MOT can be found in [56]. A newly added feature is the artificial broadening of the MOT light from 35 kHz to about 1 MHz in the early stages of the loading process to increase the trapped atom number, realized by the application of an rf modulation signal onto the main rf input of the MOT

AOM. Such techniques were previously successfully implemented in other works [129].

3.3.3 CO_2 laser radiation setup

Here the CO_2 laser light setup, used for the single optical dipole trap (SODT), and as the main beam for the hybrid crossed optical dipole trap (HCODT), is discussed. The cross beam for the HCODT is provided by a Nd:YAG laser and its setup is reviewed in Sec. 3.3.4.

The used CO_2 laser system (model *GEM-100*, supplier: *Coherent, Inc.*) emits light at 10.6 μm wavelength with a typical output power of 118 W, and is driven by a radio frequency source (model *D-1000*, supplier: *Coherent, Inc.*). Both components have to be water-cooled and temperature-stabilized by a chiller (model *WWK 14/17706*, supplier: *DELTATHERM Hirmer GmbH*). If the temperature remains sufficiently constant, lasing occurs in a single mode, which is monitored via a Fabry-Perot interferometer setup, and is typically obtained approximately 1 hour after turning on the laser.

The main portion of the output beam is guided through a water-cooled AOM (model *AGM-406B1M*, supplier: *Intra Action Corp.*) which is driven with a radio frequency input of 40 MHz, controlling the intensity in the 1st diffraction order. In contrast to older setups, where also an additional driving at 30 MHz was employed to suppress thermal drifts and therefore unwanted beam walks by keeping the radio frequency power in the AOM constant when the main rf power (in that case at 30 MHz) was ramped down during evaporative cooling [56], here no additional frequency input is used. Instead the CO_2 laser beam path was significantly shortened which also reduced unwanted beam walks to sufficiently low levels.

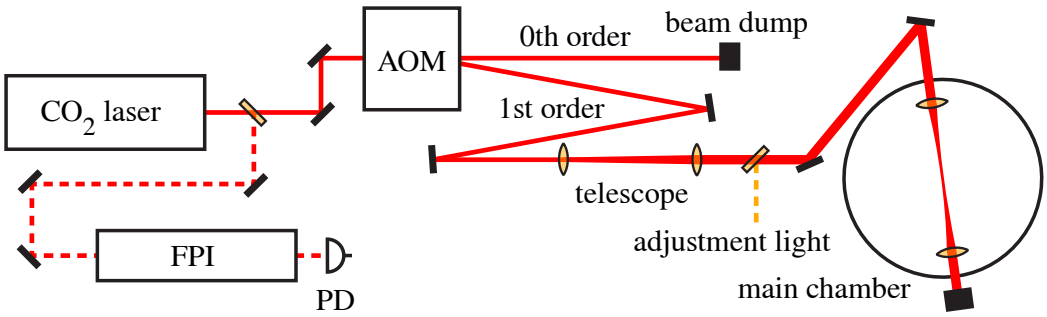

Fig. 3.5: Sketch of the CO_2 laser light setup used for the single optical dipole trap (SODT), and for the main beam of the hybrid crossed optical dipole trap (HCODT). The output laser beam is seperated into a weak beam (dashed line), led to a Fabry-Perot interferometer (FPI) where single mode operation is monitored via a photodiode (PD) on an oscilloscope, and a strong beam (solid line) that is guided through an AOM, where the 1st order beam is subsequently widened by a telescope and led into the main vacuum chamber where it is focused onto the position of the cMOT. All optical plates and lenses used here are made of zinc selenide (ZnSe). Light at 582.84 nm wavelength can be overlayed for adjustment purposes.

The 1st order beam diameter is then widened and collimated by a ZnSe telescope, and subsequently guided into the main vacuum chamber. Here it is first focused on the region of the MOT by a ZnSe lens, and afterwards collimated again by a ZnSe lens of same focal length. The beam leaves the main chamber through a viewport and ends in a beam dump. The

maximum power directly before the main chamber amounts to approximately 73 W. For adjustment purposes light at 582.84 nm can be overlayed with the CO_2 beam. The complete setup is sketched in Fig. 3.5.

The beam waist w_0 of the CO_2 laser light was determined by a razor-edge measurement outside the vacuum chamber with a proxy setup identical to the setup inside the main chamber, accessible via a flip mirror [97]. For this the collimated beam radius w at the lens position is measured, from which the beam waist at the trapping site can be estimated via $w_0 = \lambda f/(\pi w)$, where λ is the wavelength of the light, and $f = 63.5\,\mathrm{mm}$ is the focal length of the lens [130]. To check for an eventual ellipticity of the transversal beam profile, horizontal $w_{0,\mathrm{h}}$ as well as vertical beam waists $w_{0,\mathrm{v}}$ were measured. A slightly elliptically-shaped Gaussian beam can be approximated by an ideal Gaussian beam via $\tilde{w}_0 = \sqrt{w_{0,\mathrm{h}} w_{0,\mathrm{v}}}$. This approximation avoids to overcomplexify especially the already dense formulas describing the trapping potential and trapping frequencies of the HCODT (cf. Eqs. 2.46 and 2.47). The CO_2 laser light beam waists showed indeed a flattening of $(w_{0,\mathrm{h}} - w_{0,\mathrm{v}})/w_{0,\mathrm{v}} \approx 0.67$, where the effective beam waist was obtained as $\tilde{w}_0 \approx 36\,\mu\mathrm{m}$. This value (together with that of the effective beam waist of the Nd:YAG trap beam) is later used for the theoretical determination of trap frequencies of the SODT and HCODT, as well as the phase space density of the atomic ensemble inside the trap. Experimental determination of those quantities is done via different measurement methods described in Sec. 3.4.

Intensity control

The intensity of the 1st diffracted order beam can be controlled via the AOM radio frequency (rf) power input, which is proportional to the diffraction efficiency, up to a saturation regime. High rf powers lead to a heating of the germanium crystal inside the AOM, causing a change of the refractive index and subsequently a beam walk in the order of several mm for a length of 2 m. Therefore in earlier iterations of the experiment an additional driving frequency had to be implemented to keep the temperature of the germanium crystal stable while changing the main driving rf power at in that case 30 MHz [56]. Here the path length of the CO_2 laser beam was significantly reduced so that the influence of thermal drifts of the non-stabilized AOM on the spatial beam stability became negligible for the operation of an optical dipole trap.

The intensity control setup for the CO_2 laser light is shown in Fig. 3.6, with the rf path (indicated with yellow arrows) that leads to the AOM for continuous operation consisting of the following parts in the installed order (if not stated otherwise the rf components are supplied by *Mini-Circuits, Inc.*):

- Signal generator (model *SMY 01*, supplier: *Rohde & Schwarz GmbH & Co. KG*) with a 40 MHz rf output
- Switch (model *ZYSWA-2-50DR*)
- Amplifier (model *LZY-1+*)
- Voltage variable attenuator (VVA, custom model from the *Elektronikwerkstatt Physikalisches Institut Tübingen*)
- Mixer (model *ZSC-2-1*)
- Switch (same switch model as before)

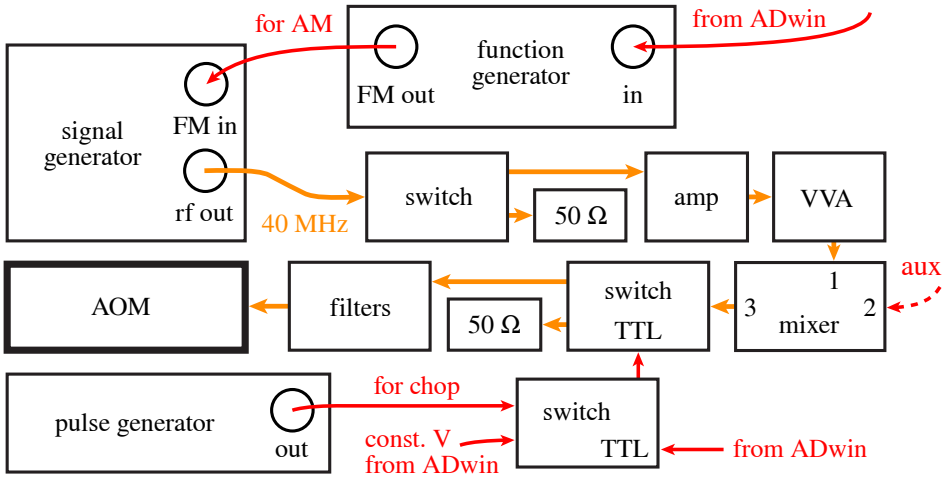

Fig. 3.6: Intensity control of the CO_2 laser light via AOM. A signal generator outputs a radio frequency (rf) signal at 40 MHz, which is passed through a switch used for turning the signal on and off, is then amplified and can subsequently be attentuated via a voltage variable attentuator (VVA). Auxiliary signals (e.g. a second driving frequency at 30 MHz) can then be added by a mixer, but this is typically not done in this experiment anymore. After passing a second switch and a filter stage, the signal arrives at the AOM. Another switch is implemented, which is given a TTL signal stemming from either a constant voltage source (*ADwin* channel) for normal optical dipole operation, or from a pulse generator for a chop mode during the atom loading phase from MOT to dipole trap (s. Sec. 4.2.1). For measurements which require an amplitude modulation (AM) of the light, a function generator can be employed which modulates the rf output amplitude of the signal generator.

- One high pass as well as two low pass filters (models *BHP-25* and *BLP-50* respectively)

The resulting rf signal is then coupled into the AOM. Optionally a function generator (model *AFG3102*, supplier: *Tektronix, Inc.*) is used to modulate the rf output signal amplitude of the signal generator for amplitude modulation (AM) measurements needed to determine the trap frequencies of the SODT and HCODT.

A pulse generator (model *9520*, supplier: *Quantum Composer*) is employed to perform a chopping (fast alternating on- and off-switching) of MOT and optical dipole trap light for better loading efficiency from the MOT into the optical dipole trap (s. Sec. 4.2.1 for the exact chopping sequence). This chop signal is put into a switch (same model as before). Another signal which is fed into the second input of the switch is a constant voltage signal stemming from an *ADwin* channel, which is used for the regular continuous operation of the optical dipole trap. The switch can therefore quickly toggle between constant and chop mode by using its output as a TTL signal for the second switch in the rf path mentioned above. This toggle process between chop and constant mode is in turn triggered by a TTL signal coming from another *ADwin* channel.

3.3.4 Nd:YAG laser light setup

The cross beam for the HCODT is provided by a Nd:YAG laser (model *Mephisto 2000NE*, supplier: *Coherent, Inc.*) run at a wavelength of 1064 nm. The laser operates in single longitudinal as well as single transverse mode, and the emission is nearly linearly polarized. The

output power amounts to 2 W. Similar to the case of the CO_2 laser, the intensity control is here realized by an AOM. For this an rf signal at 80 MHz is applied to the AOM according to the scheme shown in Fig. 3.8.

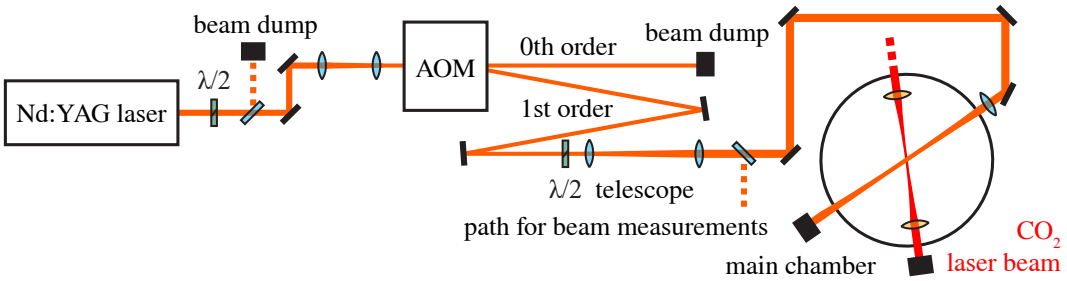

Fig. 3.7: Sketch of the Nd:YAG laser light setup used for the cross beam of the hybrid crossed optical dipole trap (HCODT). The slightly eliptically polarized output laser beam is linearly polarized via half-wave plate ($\lambda/2$) and polarizing beam splitter, as well as collimated to a smaller beam diameter via telescope for better AOM diffraction efficiency. The AOM is used for intensity control of the Nd:YAG laser light. The 1st order diffracted beam is subsequently widened by a telescope and again linearly polarized to ensure optimized scattering rates in the trap. Light can be coupled out to be used for e.g. beam waist measurements. The primary beam is led into the main vacuum chamber where it is focused onto the position of the atomic ensemble inside the SODT.

The optical setup is sketched in Fig. 3.7. After linearization by a half-wave plate and a polarizing beam splitter, and passing the AOM, the 0th order beam is sent into a beam dump, while the 1st order beam is widened by a telescope. Another half-wave plate and polarizing beam splitter are then used to couple a portion of the light out, so that it can be used for e.g. beam waist measurements, where an exact copy of the main beam path leading into the main vacuum chamber is set up. The main beam is focused onto the spatial volume in which the atomic ensemble in the SODT sits by a lens with focal length of 250 mm. Here the beam exhibits a maximum power of 1.59 W and an effective beam waist of $\tilde{w}_0 \approx 55.56\,\mu$m. The transversal Nd:YAG light beam profile at the position of the lens showed only a very small flattening of $(w_{0,\mathrm{h}} - w_{0,\mathrm{v}})/w_{0,\mathrm{v}} \approx 0.03$, meaning that the beam shape is in very good approximation circular.

Intensity control

Analog to the intensity control scheme for the CO_2 laser light, here it is also realized by setting the rf driving signal of an AOM. The rf path leading to the AOM (indicated with yellow arrows in Fig. 3.8) consists of the following parts in the implemented order (if not stated otherwise the rf components are supplied by *Mini-Circuits, Inc.*):

- Voltage controlled oscillator (VCO, model *ZOS-100+*) with an rf output at about 80 MHz
- Mixer (custom model built at this experiment)
- Bias tee (to again add DC parts that get blocked in the previous mixer)
- Switch (model *ZYSWA-2-50DR*)
- Pre-amplifier (model *ZFL-500-BNC*)

- Voltage variable attenuator (VVA, custom model from the *Elektronikwerkstatt Physikalisches Institut Tübingen*)
- Amplifier (model *LZY-1+*)

The prepared rf signal is then coupled into the AOM. The initial rf signal stemming from the VCO can also be combined with a signal from a function generator (model *AFG3102*, supplier: *Tektronix, Inc.*) for amplitude modulation (AM).

The Nd:YAG laser beam does not have to be chopped like the CO_2 laser beam, as it is only employed in the later stage of the evaporative cooling process, after loading of the atomic ensemble from the MOT into the optical dipole trap already took place.

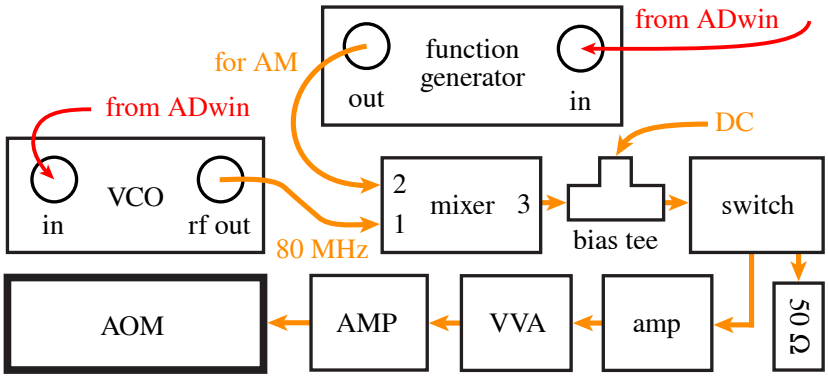

Fig. 3.8: Intensity control of the Nd:YAG laser light via AOM. A voltage controlled oscillator (VCO) outputs a radio frequency (rf) signal at about 80 MHz. For measurements which require an amplitude modulation (AM) of the light, a function generator can be employed which modulates the rf output amplitude of the VCO by combining the rf signals (and blocking the direct current (DC) part). A bias tee is used to add a DC signal again. The resulting signal is passed through a switch used for turning AOM diffraction on and off. It is then pre-amplified (amp), subsequently attentuated via a voltage variable attentuator (VVA), and amplified again (AMP). Afterwards the resulting signal is coupled into the AOM.

3.4 Measurement methods

In this section measurement methods used for the characterization of atomic clouds, i.e. their spatial extend as well as atom number, and of optical dipole traps, i.e. their trap frequencies, respectively, are briefly discussed.

3.4.1 Absorption imaging

To determine the optical density and thus the atom number of the atomic cloud the absorption imaging technique can be utilized [131]. The atomic cloud is illuminated with a spatially filtered, collimated, resonant and linearly polarized light beam (typically after turning the current trap potential off), which is partly absorbed by the atoms, and the shadow casted by the atomic ensemble is imaged onto a camera by a lens, as seen in Fig. 3.9.

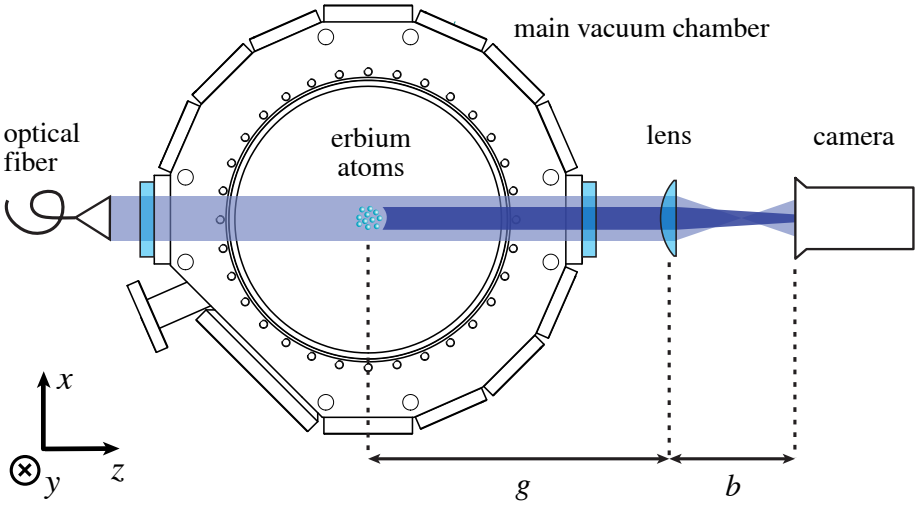

Fig. 3.9: Sketch of the absorption imaging setup. The atomic ensemble gets illuminated with resonant light traversing through the main vacuum chamber along the z-axis, and its shadow is imaged by a lens onto a camera and subsequently detected, leading to an intensity distribution in the x-y-plane. The spatial resolution of the absorption imaging is limited to $(4 \pm 1)\,\mu$m, given by the object distance g of approximately 270 mm.

According to Lambert-Beer's law the spatial intensity distribution $I(x, y)$ of a beam, after traversing along z through some volume with an optical density distribution $D(x, y)$, is obtained from an initial spatial intensity distribution $I_0(x, y)$ by [132]

$$I(x,y) = I_0(x, y)e^{-D(x,y)}. \tag{3.1}$$

Knowing the optical density distribution, the atom number N can then be calculated via

$$N = \int n(x, y, z)\,\mathrm{d}x\mathrm{d}y\mathrm{d}z = \frac{1}{\sigma_\pi}\int D(x, y)\mathrm{d}x\mathrm{d}y, \tag{3.2}$$

where $n(x, y, z)$ is the atomic density distribution, and the photon absorption cross section for linearly polarized light σ_π is obtained as

$$\sigma_\pi = C^2\frac{3\lambda^2}{2\pi}\frac{1}{1 + (2\delta/\Gamma)^2}, \tag{3.3}$$

with $C^2 = 0.385$ being the mean square of the Clebsch-Gordan coefficients for the transition probabilities of the different m_J states from -6 to $+6$ for the transition near 400.91 nm wavelength. The above treatment is valid in an intensity regime of negligible saturation. By measuring the intensity distribution $I_{\mathrm{abs}}(x, y)$ with, and the distribution $I_{0,\mathrm{abs}}(x, y)$ without atomic ensemble, respectively, one can obtain the optical density distribution. To account for background illumination of the camera sensor, a third background intensity distribution measurement $I_{\mathrm{bg}}(x, y)$ without absorption imaging light is performed. All three images are taken successively with an exposure time of 80 μs for each individual image. The optical density distribution can then be expressed as

$$D(x,y) = -\ln\left(\frac{I(x,y)}{I_0(x,y)}\right) = -\ln\left(\frac{I_{\mathrm{abs}}(x,y) - I_{\mathrm{bg}}(x,y)}{I_{0,\mathrm{abs}}(x,y) - I_{\mathrm{bg}}(x,y)}\right). \tag{3.4}$$

The spatial resolution of the absorption imaging amounts to $(4 \pm 1)\,\mu$m. By taking absorption images at different points in time (while for each image a new experimental cycle has to be conducted as the method is destructive), the temporal evolution of e.g. expanding clouds after trap release can be documented (called time of flight measurement), which for this example can be used to determine the temperature of the atomic ensemble, as further discussed in Sec. 4.1.2.

3.4.2 Trap frequency measurements and phase space density determination

The atomic density has to be known for the determination of the phase space density, and can be calculated from the trap frequencies [48]. We here assume a Gaussian atomic density distribution according to

$$n(x,y,z) = n_0 \exp\left(-\frac{x^2}{2\sigma_x^2} - \frac{y^2}{2\sigma_y^2} - \frac{z^2}{2\sigma_z^2}\right), \tag{3.5}$$

where σ_i is the $1/e^2$ atomic cloud radius in direction along i, with $i = x, y, z$, and $n_0 = N/((2\pi)^{3/2}\sigma_x\sigma_y\sigma_z)$ is the central atomic density. The total atom number N is obtained via Eq. 3.2. The cloud radii can be calculated by means of the virial theorem, which connects the temporal mean of potential and kinetic energy, respectively, the latter here provided by the thermal motion of the atoms in the considered spatial direction i [133]. For a harmonic potential and a Gaussian density distribution it follows that

$$\sigma_i = \sqrt{\frac{k_{\mathrm{B}}T}{m\omega_i^2}}. \tag{3.6}$$

With Eq. 2.9 and the central atomic density n_0, the phase space density is obtained as

$$\rho = \frac{\hbar^3 N}{k_{\mathrm{B}}^3 T^3}\omega_r^2\omega_z, \tag{3.7}$$

where $\omega_x = \omega_y = \omega_r$ is assumed. The trap frequencies can be measured by means of parametric excitations of the trap. Two methods are used in this thesis and discussed below. Together with the temperature T, the phase space density can therefore be calculated from measurable quantities in the experiment.

Amplitude modulation

Here the amplitude of the optical dipole trap potential is sinusoidally modulated to find the trap frequencies $\nu_{\mathrm{trap}} = \omega_{\mathrm{trap}}/(2\pi)$ of the optical dipole trap. For this the atomic ensemble is first loaded from the MOT into the dipole trap, then evaporatively cooled up to a set point

(e.g. until 10.00 % of the initially used power is reached, as is the case in Fig. 3.10), and subsequently subjected to the trap potential while its amplitude is modulated around the set point, realized by the modulation of the CO_2 laser light power via modulation of the AOM rf driving power, or in the case of a hybrid crossed dipole trap additionally by synchronous Nd:YAG laser light modulation via its corresponding AOM rf driving. The amplitude modulation (AM) is performed with a fixed number of modulation periods, here 100 times, for each modulation frequency that is used in the measurements. Parametric excitation occurs for modulation frequencies equal to the doubled trap frequency $\nu_{\mathrm{mod}} = 2\nu_{\mathrm{trap}}$ or to a harmonic multiple $\nu_{\mathrm{mod}} = 2\nu_{\mathrm{trap}}/n$, with $n \in \mathbb{N}$, given an adequate phasing, so that the atoms receive so much energy that they can leave the trap.

If one measures the atom number via absorption imaging after amplitude modulation for different modulation frequencies, one observes strong dips at the resonance frequencies, as seen in Fig. 3.10(a). The depth of modulation was individually set for each end power measurement series to obtain observable dips, typically ranging from 5.5 to 30 %, with greater depths for higher end powers. As the number of modulation periods is fixed, for very small modulation frequencies the total modulation time $t = 100/\nu_{\mathrm{mod}}$ becomes so large that the atom's lifetime inside the trap becomes relevant. To get a baseline measurement showing only the atom losses due to the finite trap lifetime, the same measurement, but without amplitude modulation, is performed, s. Fig. 3.10(b). With the amplitude modulation technique one can measure trap frequencies in all spatial directions [48, 107].

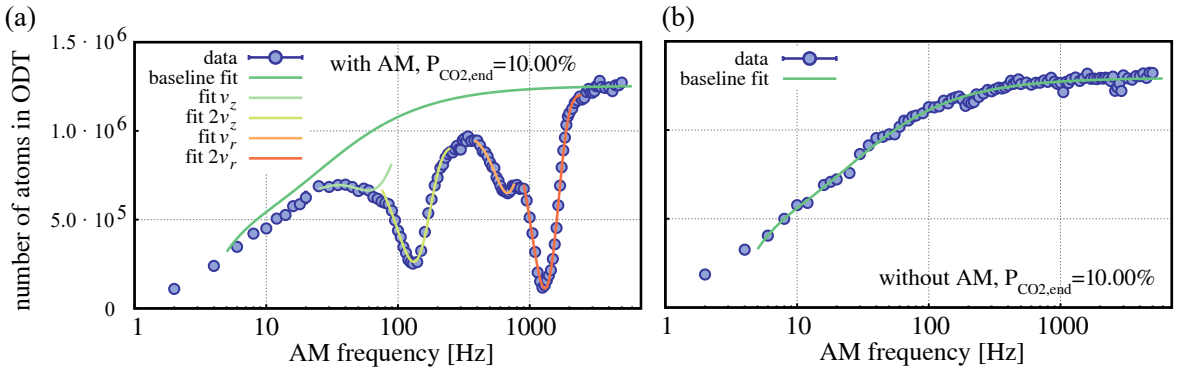

Fig. 3.10: Measurement of trap frequencies via amplitude modulation (AM) of the trap depth, here for the single optical dipole trap (SODT) at 10.00 % of the maximum possible power of roughly 73 W. (a) Several resonances can be seen which could be identified as the radial trap frequency $2\nu_r$ at (1303 ± 4) Hz, the harmonic multiple with $n = 2$ of the radial trap frequency ν_r at (678 ± 4) Hz, the axial trap frequency $2\nu_z$ at (132 ± 1) Hz, and the harmonic multiple with $n = 2$ of the axial trap frequency ν_z at (68 ± 10) Hz. Note that for approximately circularly shaped beams in transversal direction the trap frequencies ν_x and ν_y overlap strongly and merge into one radial trap frequency ν_r for both directions. Here the systematic errors are estimated to lie in the same order of magnitude as the given errors stemming from the fit. (b) A baseline measurement without AM was performed to account for the finite lifetime of the atoms inside the trap, and also, as one measurement series for a specific AM set point takes several hours to perform, to account for possible thermal drifts in the experiment which could change the atom number in the MOT or optical dipole trap in later experimental cycles slightly over long periods of time. Especially for small modulation frequencies the total modulation times reached sizes comparable to the trap lifetime. The baseline fit function was chosen by convenience.

Kohn breathing mode

For the Kohn breathing mode method to determine the trap frequency in the axis of gravity, here the y-axis, one first turns the potential of the optical dipole trap off for a short period of time of 500 μs, to allow the atoms to acquire kinetic energy by falling down due to the gravitational force. Subsequently the trap is turned on again, recapturing the atoms, leading to an oscillation of the atoms inside the trap with the trap frequency $\nu_r = \omega_r/(2\pi)$. The atoms are released after a variable holding time and are allowed to freely expand, effectively enlarging the periodic movement of the atoms so that it can be seen on camera. After a fixed time of free expansion, absorption imaging is performed to determine the position of the atomic ensemble. Measurements show a cosine-like behaviour of the position over time, together with an exponential damping as the atoms lose kinetic energy due to friction and losses into other spatial dimensions, as seen for the case of the HCODT in Fig. 3.11. Note that here only the radial trap frequency can be determined [59, 134], which however can be utilized to unambiguously establish the correct trap frequency labeling of the atom number dips seen in amplitude modulation measurements.

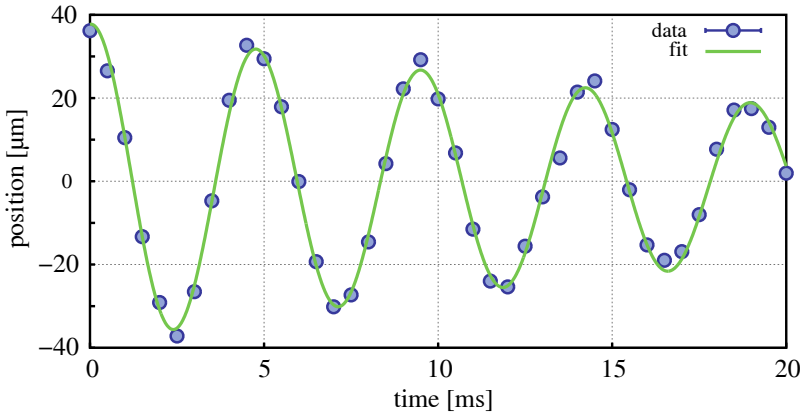

Fig. 3.11: Measurement of trap frequencies via Kohn breathing mode method, here for the hybrid crossed optical dipole trap (HCODT) at 0.52 % of the maximum possible CO_2 laser power of about 73 W, and at 42 % of the maximum possible Nd:YAG laser power of roughly 1.6 W. This corresponds to a scaling factor $\mathrm{scal}_U = U_{0,\mathrm{YAG}}/U_{0,\mathrm{CO_2}} = 0.5$ between the trap depths of both beams. Atoms are allowed to acquire kinetic energy by turning the HCODT off for a short period of time so that the atoms can drop due to gravity, after which they are recaptured and begin to oscillate in the trap potential. Following a variable holding time inside the trap, the atoms are released again for a fixed period of free expansion. Absorption imaging is performed to determine the position after free expansion vs the holding time. A cosine function with exponential damping is fitted to the data, leading here to a radial trap frequency ν_r of (211 ± 1) Hz.

4 Characterization of the setup and experimental results

In this chapter results regarding the characterization of the experimental setup for the generation of an atomic erbium Bose-Einstein condensate (BEC) in a hybrid crossed dipole trap are presented. Starting with the narrow-line magneto-optical trap (MOT), properties as the temperature of the atomic ensemble and the total atom number, as well as the compressing process are shown. Next the atom loading procedure from the compressed MOT into the optical dipole trap is described. Following this, many properties of the trap, as e.g. the trap frequencies, in single optical dipole trap (SODT) configuration and in hybrid crossed optical dipole trap (HCODT) configuration, respectively, are discussed and compared. Here the second (cross) beam for the hybrid crossed optical dipole trap is only used in the later stages of the experimental cycle after the evaporative cooling process has already started. This evaporation process is then as well compared for both possible setups (SODT/HCODT). Emphasis is also put on the spin-polarization of the atomic ensemble inside the optical dipole trap, measured via an Stern-Gerlach type experiment. In the end proof of Bose-Einstein condensation, including a determination of the phase space density and the lifetime in the different trap configurations, is presented.

4.1 Magneto-optical trap

Atoms decelerated by the Zeeman slower are captured in the magneto-optical trap. A characterization of the atomic beam including the efficiency of the Zeeman slower can be found in [56] and is not repeated here as the corresponding part of the setup remained mainly unchanged. The atoms leave the atomic oven with a mean velocity of 490 m/s. Here the operation temperature of the effusion cell was reduced by 100 K to 1373 K in comparison to older iterations of the experiment to preserve the atomic oven against further breakdowns mentioned in Sec. 3.2. Due to the capture velocity of the MOT of $v_{\mathrm{cap}}^{\mathrm{MOT}} = 3.3\,\mathrm{m/s}$ a portion of the atoms in the atomic beam has to be slowed down considerably. For this the Zeeman slower beam operated at about 400.91 nm wavelength is roughly aligned by maximizing its decelarating influence on the atomic beam observable via velocity-sensitive fluorescence imaging [56]. After that, fine-tuning of the Zeeman slower takes place by maximizing the loading rate of the MOT and therefore the maximal number of trapped atoms after a fixed loading period. The transversal cooling stage efficiency is optimized in the same manner. The in this way pre-cooled atoms are then loaded into the MOT which is roughly located at the center of the main vacuum chamber.

4.1.1 Loading of the magneto-optical trap

More precisely, there exist two MOT phases: a loading phase where atoms from the decelerated atomic beam are captured, operated with light of large detuning from resonance near

582.84 nm wavelength, resulting in a large spherical trapping volume (called MOT in the following), and a compressing phase where the detuning and intensity of the MOT light is decreased, leading to a spatial shrinking of the MOT volume (called cMOT in the following), utilized to maximize the efficiency of the following step, a transfer process into the optical dipole trap. The temporal evolution of the corresponding experimental parameters can be seen in Fig. 4.1, and in situ images of the atomic fluorescence during the different MOT phases are shown in Fig. 4.2. In this section measurements for the characterization of the loading process of the magneto-optical trap are presented.

Atom numbers in the loading MOT during this thesis amount up to $5 \cdot 10^7$ after a loading time of 10 s. Here the use of a transversal cooling stage increased the final atom number in the MOT roughly by a factor 2, comparable to earlier works [56]. The loading MOT light is operated at a detuning of -44 natural linewidths away from resonance. The magnetic field gradient is set to 3.8 G/cm. The light intensity per axis amounts to roughly $8\,\mathrm{mW/cm^2}$. Due to the large detuning the atoms gather in a gravitational sag below the Zeeman slower beam.

Then the number of atoms could be increased by another factor of 1.5 compared to earlier work [56] by modulating the MOT light at the beginning of the loading phase, leading to a very broad linewidth of the light of approximately 3.2 MHz. This is done by applying an rf modulation signal onto the AOM originally used for intensity control of the MOT light. Due to the increased linewidth, MOT light scattering and therefore optical cooling takes place for a broader velocity class of atoms from the atomic beam. The broadening is ramped down linearly in time and vanishes during the loading phase.

The qualitative loading behaviour is discussed in [56] and is not further examined here for brevity. The holding time in the MOT after turning off the Zeeman slower light also has not changed significantly from earlier setups and lies in the region of a few minutes, which is more than sufficient for trapping and subsequent loading into the optical dipole trap. Typical equilibrium temperatures lie theoretically in the region of 20 μK, but are in practice difficult to determine, as the trapping volume has to be estimated. A more interesting quantity is the temperature in the cMOT after the compression phase ended, which is discussed in the next section.

4.1.2 Compressing process

For a good spatial overlap of the atomic cloud inside the MOT and the comparatively small beam volume of the optical dipole trap, the MOT is compressed by changing the light frequency and intensity, as well as the magnetic field gradient linearly over time. This also changes the absolute position of the atomic ensemble inside the MOT, which is in the loading process below the center height of the main vacuum chamber and therefore the optical dipole trapping laser beams, but after the compressing phase on the correct height. The detuning of the MOT light frequency is ramped to approximately -3 natural linewidths, while the light intensity per axis is lowered to $0.13\,\mathrm{mW/cm^2}$, both within a time interval of 400 ms, which is much bigger than the equilibrium time of 15 ms, as discussed in Sec. 2.3.2, and thus should not cause any additional heating of the atoms. For an overview of all parameters changed during the compressing phase, see Fig. 4.1. The cMOT encompasses about $5 \cdot 10^7$ atoms with a radius of approximately 160 μm in both horizontal axes, and 60 μm in the vertical

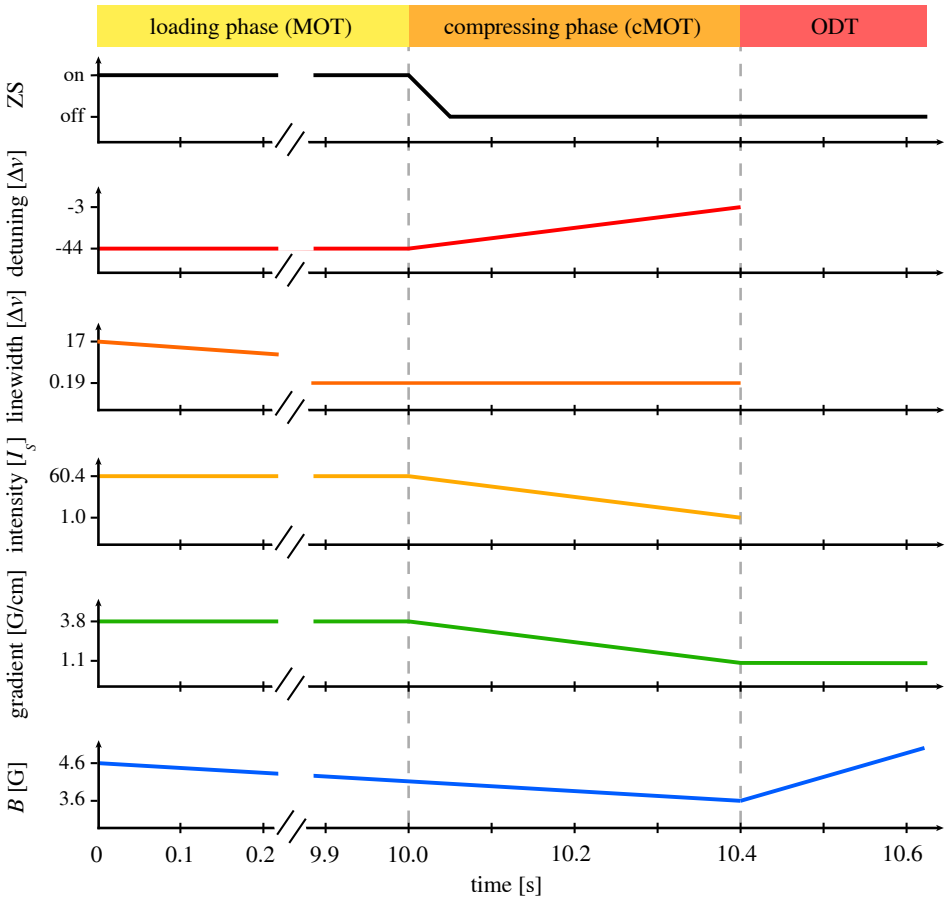

Fig. 4.1: Schedule for magneto-optical trap operation. The overall MOT phase consists of a loading phase (with conventional MOT operation), and a compressing phase (called cMOT). The MOT is loaded from an atomic beam, partially decelerated by a Zeeman slower, for 10 s. Here the frequency of the loading MOT light is detuned about -44 natural linewidths $\Delta\nu$ from the atomic resonance, and the intensity per axis amounts to roughly 60 saturation intensities I_S. A short artificial broadening segment at the beginning of the loading phase increases the linewidth of the light to approximately 17 natural linewidths, which is then linearly ramped down to the laser linewidth of about 35 kHz $\approx 0.19\,\Delta\nu$. The magnetic field gradient is set to 3.8 G/cm, and the constant offset magnetic field B, used as a preference axis for the spin-polarization, is first set to 4.6 G and ramped slightly down to eventually 3.6 G. After the loading procedure, the Zeeman slower light is turned off and the atomic beam is blocked by a mechanical shutter. For compressing, in 400 ms the detuning of the MOT light is ramped to approximately -3 natural linewidths, its intensity per axis is reduced to a value of $1.0\,I_S$, and the magnetic field gradient is changed to approximately 1.1 G/cm. After the compression phase has ended, the atoms are loaded into the optical dipole trap (ODT), with more details to be found in Fig. 4.4.

axis, assuming an oblate spheroid for the cMOT volume.

The temperature of the spatially compact ensemble inside the cMOT can be determined with good accuracy via the time of flight (TOF) technique [135]. Here the trapping potential is turned off, followed by absorption imaging of the atomic ensemble for varying times of free flight, which delivers the temporal evolution of the density distribution $n(x, y)$, showing a spatial expansion of the thermal cloud that is related to its temperature via the Maxwell-

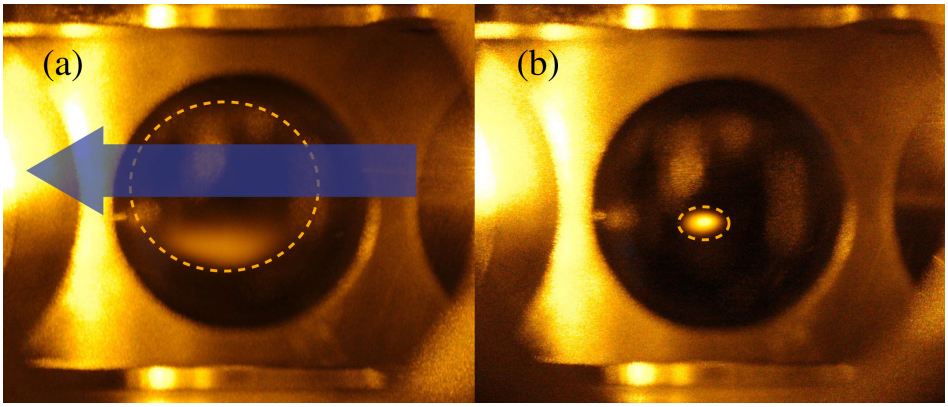

Fig. 4.2: Images of the fluorescence from atoms trapped inside the magneto-optical trap taken with a digital single-lens reflex camera (DSLR). (a) Shown is the fluorescence during the loading phase. Here the frequency of the MOT light is operated several natural linewidths away from resonance. As a blue arrow the Zeeman slower beam is sketched, indicating that the atoms gather in a gravitational sag below it. (b) Shown is the fluorescence near the end of the compression phase. Here the detuning to resonance and intensity of the light are each much smaller than in the loading phase. The atomic cloud is compressed and spatially pulled to the center of the main vacuum chamber. During this phase the Zeeman slower light and atomic beam are already shut off, so that atoms in the compressed MOT do not receive a momentum transfer by blue light or collide with fast atoms, as both would lead to losses in the trap.

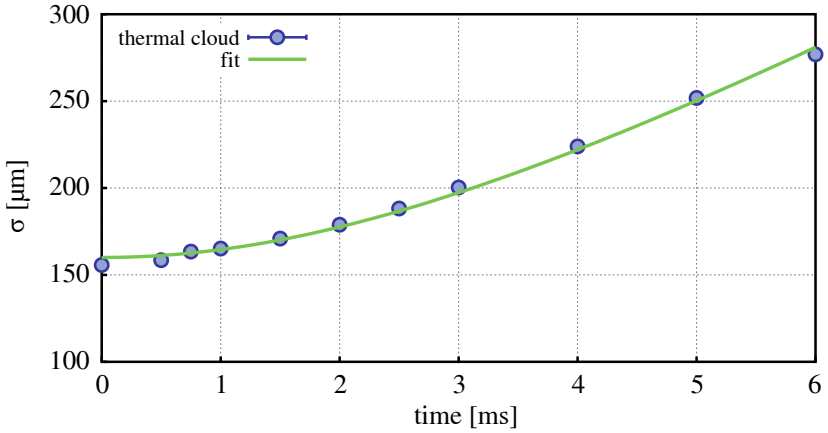

Fig. 4.3: Time of flight (TOF) measurement of the compressed MOT (cMOT) already optimized for loading into the optical dipole trap. To determine the temperature of the atomic ensemble, Eq. 4.1 is fitted to the measured data, resulting in a temperature of $(29.8 \pm 0.7)\,\mu$K.

Boltzmann velocity distribution. For an atomic cloud initially trapped inside a harmonic trap potential the density distribution exhibits a Gaussian profile according to $n(x, y, t) \propto \exp[-r^2/(2\sigma^2(t))]$, with $r = \sqrt{x^2 + y^2}$, and thus the $1/e^2$ radius σ of the atomic cloud can be extracted from the absorption measurement. The temporal evolution of the radius is described by

$$\sigma(t) = \sqrt{\sigma_0^2 + \frac{k_\mathrm{B} T}{m} t^2}, \tag{4.1}$$

where $\sigma_0 = \sigma(t = 0)$ is the initial radius. A fit of Eq. 4.1 yields the temperature T of the ensemble as a fit parameter [131], with a TOF measurement of the cMOT shown in Fig. 4.3, resulting in temperatures of around $30\,\mu$K, laying roughly two orders of magnitude below values for a broad-line atomic erbium MOT operated at a wavelength of 400.91 nm [55]. Under the assumption of an approximately oblate spheroidal volume of the cMOT, with long radii of $160\,\mu$m and a short radius of $60\,\mu$m, the phase space density can be calculated according to Eq. 2.9 to roughly $1.2 \cdot 10^{-4}$, which compares to similar experiments as well as earlier iterations of this experiment [56], but is still 4 orders of magnitude smaller than needed for a phase transition to a BEC [80]. To increase the phase space density further, atoms are loaded into an optical dipole trap, where evaporative cooling is employed, as discussed within the next sections.

4.2 Characterization of single and hybrid crossed dipole trap

In this section the optical dipole trap (ODT) in single (SODT) and hybrid crossed (HCODT) configuration, used for evaporative cooling of the atomic ensemble, is characterized. For this, first the loading process from the cMOT into the CO_2 laser dipole trap is discussed, after which measurements of characteristic quantities are shown. Measurements include the trap frequencies, holding times, temperatures and spin-polarization of the atomic ensemble. Lastly the phase space density is calculated from measurement outcomes. Results are compared for the single beam trap and hybrid crossed beam trap case.

4.2.1 Loading process

A portion of the atomic ensemble is loaded from the cMOT into the optical dipole trap. In the beginning of either SODT or HCODT operation, only the CO_2 laser beam is let into the main vacuum chamber. Early attempts to just overlay cMOT and ODT turned out to be unfeasible due to the ac Stark effect, treated in Sec. 2.3.3, as the atomic states shift negated the resonance condition for the cMOT light, and the atoms were repelled, leading then to no transfer into the ODT. This issue could be resolved by fast alternating off- and on-switching, so-called chopping, of cMOT and ODT light during the loading process [136].

The chopping procedure is sketched in Fig. 4.4. The MOT and ODT light are alternately turned on- and off respectively for $20\,\mu$s each, with a very short phase of $2\,\mu$s between each reversal in which both lights are kept off. With chopping the influence from the ac Stark shift by the CO_2 laser light is dispelled. The exact sequence was found by optimizing the loading efficiency into the ODT. The loading efficiency compared to a transfer without chopping but abrupt conversion from cMOT to ODT was increased by roughly 20 %. After loading into the ODT and a holding time of 15 ms typically $7 \cdot 10^6$ atoms reside in the trap. Due to an overlap with the atomic cloud from the cMOT an earlier precise measurement of the atom number inside the ODT is not possible, but has to be postponed to times in which the cMOT ensemble dropped outside the absorption imaging area near the ODT due to gravity. Absorption images showing the transfer from cMOT to ODT, alongside the dropping of the non-loaded atoms, are depicted in the first 5 panels of Fig. 4.5.

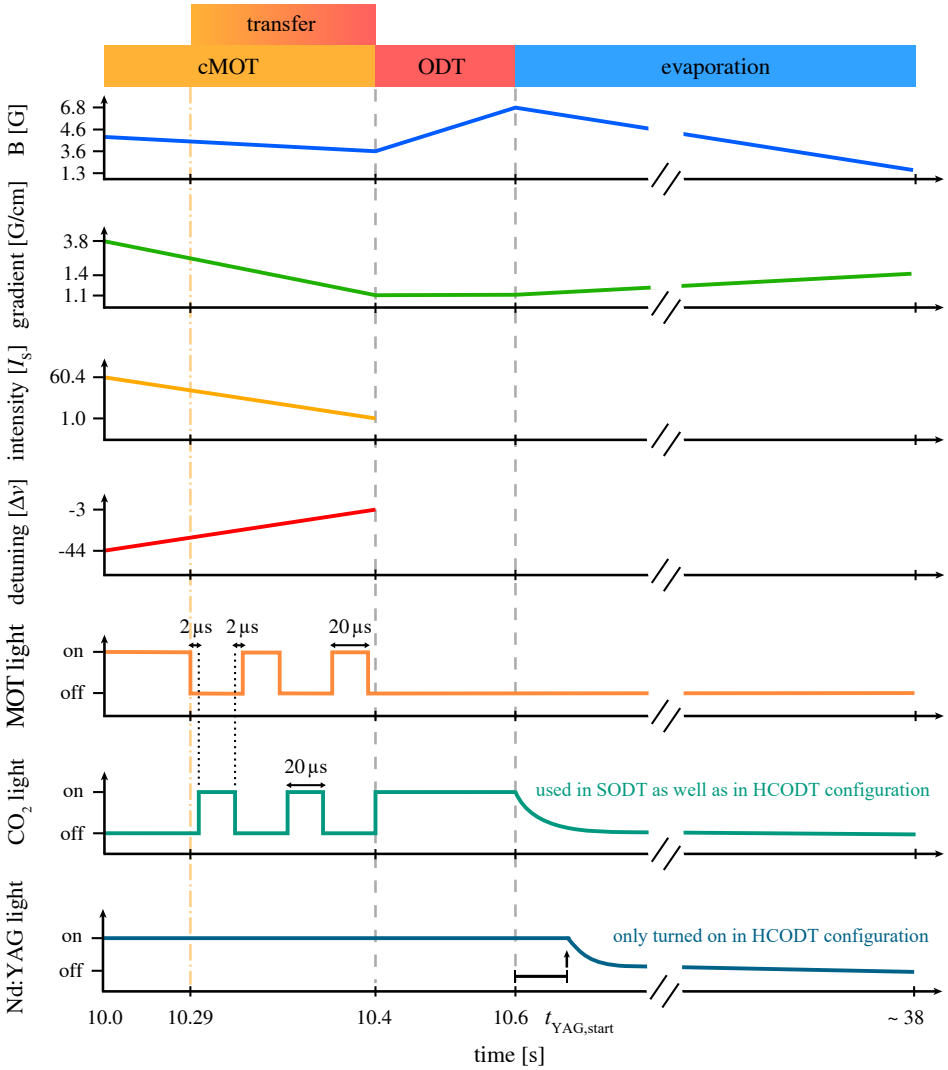

Fig. 4.4: Schedule of the atom transfer from cMOT to the optical dipole trap (ODT). To load atoms efficiently, cMOT and ODT are alternately turned on and off respectively during a 110 ms long transfer period (equaling 2500 chopping cycles). There cMOT and ODT are each turned on for 20 μs, with a 2 μs long pause in between where neither light is turned on to ensure no temporal overlap. The MOT compressing, i.e. linear ramping of experimental parameters, is still performed during chopping, and at the end of transfer, the cMOT light is turned off. After a holding time of 200 ms inside the ODT provided by the CO_2 laser beam the evaporation process begins by lowering its beam power. In SODT configuration no second beam is turned on. In HCODT configuration however a cross beam provided by a Nd:YAG laser is added after a variable time $t_{\mathrm{YAG,start}}$, which depends amongst others on the final CO_2 laser beam power at end of evaporation and the desired ratio between individual dipole trap depths, $\mathrm{scal}_U = U_{0,\mathrm{YAG}}/U_{0,\mathrm{CO_2}}$, see Eq. 4.2. The power of the Nd:YAG trapping beam is continuously adjusted so that scal_U stays constant during the remaining evaporation process. During evaporation the magnetic field gradient is linearly ramped back up to 1.4 G/cm. The offset magnetic field is first ramped to 6.8 G during the holding phase inside the ODT, and subsequently ramped down to a value of roughly 1.3 G during evaporation. All parameters are optimized for a maximum Bose-Einstein condensate atom number at end of evaporation.

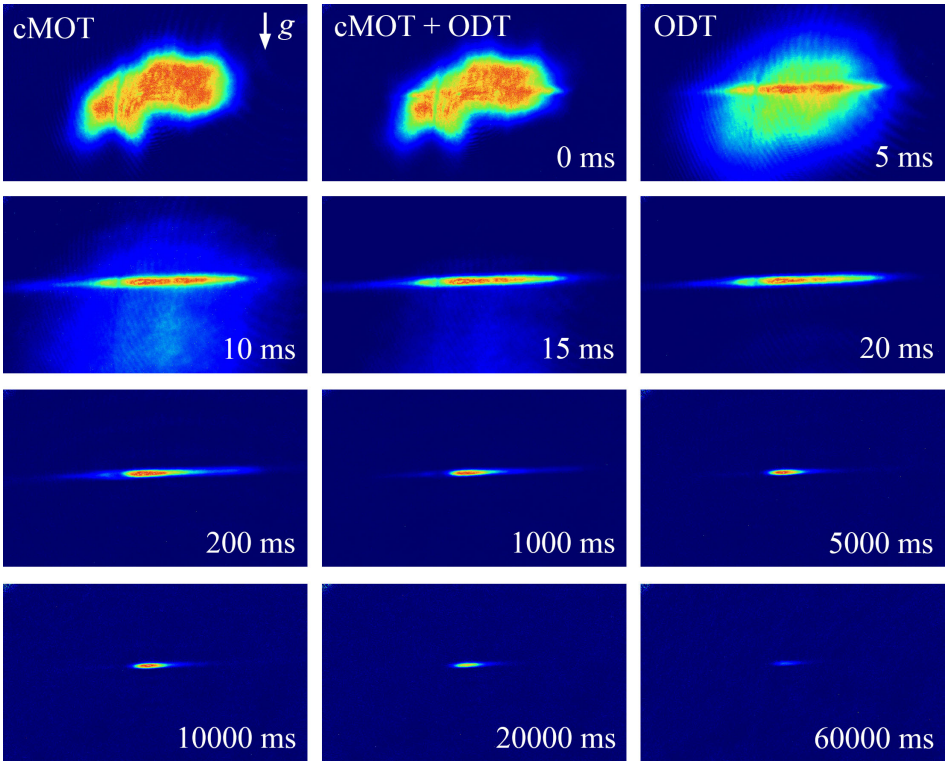

Fig. 4.5: Absorption images showing loading from cMOT into ODT as well as subsequent holding in SODT configuration. Here gravitation points downwards. The first panel shows roughly $5 \cdot 10^7$ atoms trapped in the cMOT at the end of the compression phase. In the second panel the same point in time is shown, but now with an enabled CO_2 laser beam for the ODT. In the bottom right of all ODT panels the holding time since the start of the ODT phase (depicted in Fig. 4.4) is denoted. Note that no forced evaporation is employed here, and thus the power of the CO_2 laser beam stays constant after enabling it. Approximately $7 \cdot 10^6$ atoms are trapped inside the ODT after 15 ms holding time. One can see in the last panel that after a 60 s holding sequence still about 35000 atoms remain inside the SODT. Each panel image is averaged from three individual measurements. The color scale denoting the optical density is set the same for all images and was not recalibrated while measuring.

4.2.2 Trap frequencies

Trap frequencies were measured via amplitude modulation (AM) and Kohn breathing mode methods (cf. Sec. 3.4.2). Fig. 4.6 shows results for the AM measurements for both SODT and HCODT configuration. Fitted are functions of form $\nu(P_{\text{end}}) \propto \sqrt{P_{\text{end}}}$ to each data series, with P_{end} being the power of the CO_2 laser beam at the end of evaporation. Notably while the radial trap frequencies are not significantly altered by the addition of the Nd:YAG laser trap beam, the axial trap frequencies are muchly increased. This is understood as the radial confinement by the CO_2 laser beam is much stronger than its axial confinement.

Fig. 4.7 shows results for the Kohn breathing mode measurements, that are directly compared to the AM measurement results from Fig. 4.6. The measurement comparison shows a general agreement between AM and Kohn breathing mode method with a discrepancy of the (solid) fit functions $\nu(P_{\text{end}}) \propto \sqrt{P_{\text{end}}}$ for each data series, with P_{end} being the power of the CO_2 laser beam at the end of evaporation, of approximately 7 %. Note that only the radial trap

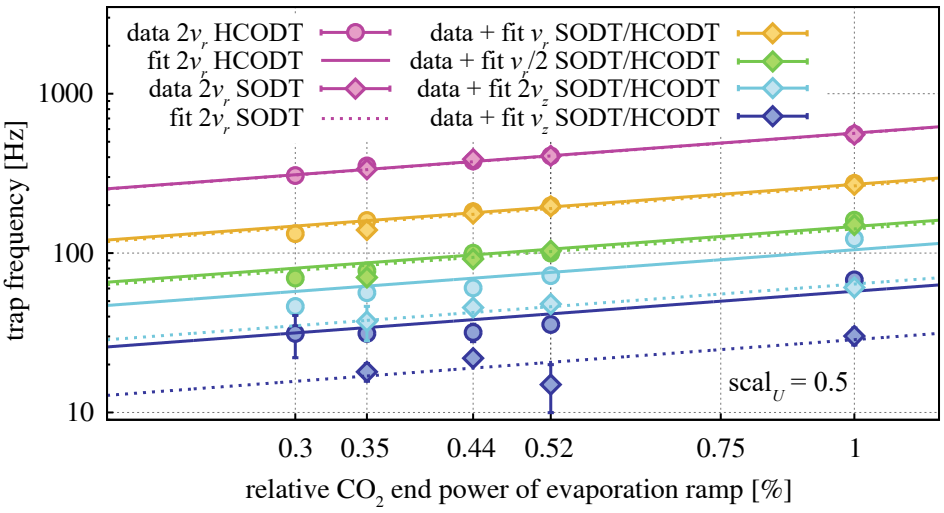

Fig. 4.6: Trap frequency measurements via amplitude modulation (AM) method for SODT and HCODT configuration, plotted in double logarithmic scale. Shown is data for the radial trap frequency ν_r and harmonics $2\nu_r$ as well as $\nu_r/2$, and the axial trap frequency ν_z and harmonic $2\nu_z$. Data points for SODT (HCODT) configuration are depicted as diamonds (circles). Fit function of form $\nu(P_{\mathrm{end}}) \propto \sqrt{P_{\mathrm{end}}}$ for each data series, with P_{end} being the power of the CO_2 laser beam at end of evaporation, and $P_{\mathrm{init}} = 72.6\,\mathrm{W}$ being the initial power, are also depicted for SODT (dotted lines) and HCODT (solid lines) configuration. The scaling factor between individual trap depths was set to $\mathrm{scal}_U = U_{0,\mathrm{YAG}}/U_{0,\mathrm{CO_2}} = 0.5$ in the HCODT case. While the radial trap frequencies are not changed significantly when the Nd:YAG laser beam is added (HCODT), the axial trap frequencies are increased notably.

frequency ν_r is evaluated here as it is the only one that can be measured via Kohn breathing mode. This fact can, however, be used to undoubtedly identify ν_r and subsequently all other trap frequencies in the AM measurement. It should also be noted that the discrepancy could stem from the circumstance that the Kohn breathing mode measurement in practice determines ν_y, while the AM measurement maps ν_r which arises from an overlap of ν_x and ν_y for transversally non-spherically shaped beams. Values for the trap frequencies obtained from the AM measurements can be found in Tab. 4.1.

4.2.3 Holding time and temperature

For characterization of the atomic ensemble inside the SODT and HCODT respectively, the holding times, temperatures and phase space densities for each configuration was determined. In the case of the holding time measurement, the atoms were loaded from cMOT into the optical dipole trap (here in SODT configuration) and held for a variable time. After that the trap was turned off, followed by absorption imaging. Here no evaporative cooling took place as the CO_2 laser beam power was kept constant at its maximum. The number of atoms can be obtained from the absorption images for different holding times, shown in Fig. 4.8(a), revealing a double exponential progress. The first decay with time constant $\tau_1 = 0.60$ s at the beginning of the holding process is caused by natural evaporation. The second decay was expected to be only caused by collisions with the background gas, which would result in very long holding times in the order of at least 30 s [123]. Instead, the time constant only amounts to $\tau_2 = 12.71$ s, indicating either further natural evaporation processes [56] or possibly three-

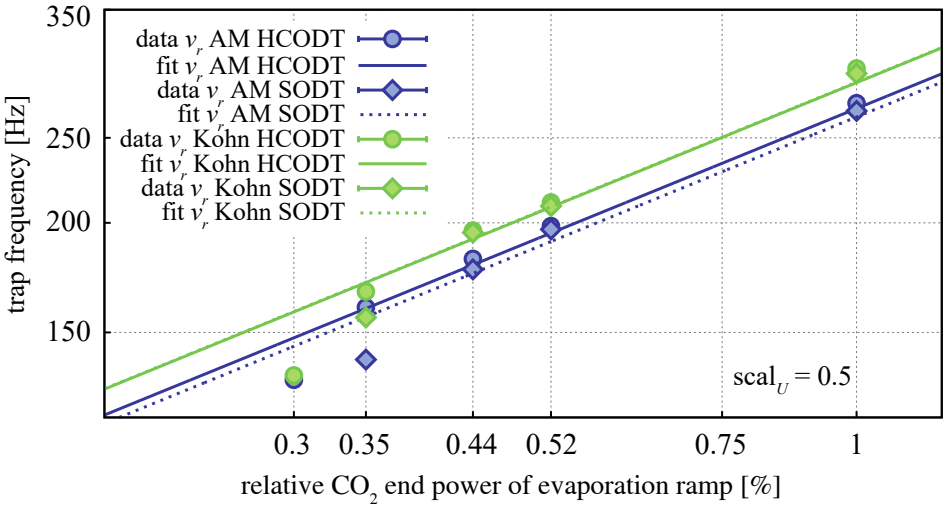

Fig. 4.7: Trap frequency measurements via Kohn breathing mode method, compared to AM measurement results for SODT and HCODT configuration, plotted in double logarithmic scale. Shown is data for the radial trap frequency ν_r. Data points for SODT (HCODT) configuration are depicted as diamonds (circles). Fit functions of form $\nu(P_{\mathrm{end}}) \propto \sqrt{P_{\mathrm{end}}}$ for each data series, with P_{end} being the power of the CO_2 laser beam at end of evaporation, and $P_{\mathrm{init}} = 72.6\,\mathrm{W}$ being the initial power, are also depicted for SODT (dotted lines) and HCODT (solid lines) configuration. The scaling factor between individual trap depths was set to $\mathrm{scal}_U = U_{0,\mathrm{YAG}}/U_{0,\mathrm{CO_2}} = 0.5$ in the HCODT case. A good agreement between AM and Kohn breathing mode measurement was found, with a discrepancy of the (solid) fit functions of only 7 %.

body losses, which can become relevant at high atomic densities [48].

A temperature measurement via TOF, depicted in Fig. 4.8(b), shows a higher temperature of the atomic ensemble of $(103.6 \pm 5.2)\,\mu\mathrm{K}$ in the optical dipole trap in SODT configuration at maximum power of $P_{\mathrm{init,CO_2}} = 72.6\,\mathrm{W}$ after a holding time of 200 ms, compared to the temperature found in the cMOT (cf. Fig. 4.3). The temperature here is, however, still much lower than the trap potential depth $U_{0,\mathrm{init,CO_2}}$ which amounts to typical values of $2.1\,\mathrm{mK/k_B}$ in this experiment. Note that the measurements presented in this section were only performed for SODT configuration as the Nd:YAG cross laser beam is only employed in the later stages of the evaporation process, as discussed in Sec. 4.3.

4.2.4 Spin-polarization

To verify spin-polarization of the atomic ensemble, it is evaporatively cooled to an ultracold thermal ensemble (in this case without reaching quantum degeneracy), and is subsequently exposed to a Stern-Gerlach type experiment. For this the optical dipole trap (in HCODT configuration) is turned off after evaporation and a short holding time, while a magnetic field gradient of roughly 3.8 G/cm is applied, and the atomic ensemble is allowed to freely expand. After a fixed time after trap release, absorption imaging takes place [137]. The magnetic field gradient causes a spin-dependent force, which spatially separates atoms in different m_J states, so that for an in very good approximation spin-polarized ensemble, i.e. virtually all atoms being in the same m_J state, no measurable separation occurs, with the here obtained experimental result shown in the upper panel of Fig. 4.9(a). A weak homogeneous magnetic field,

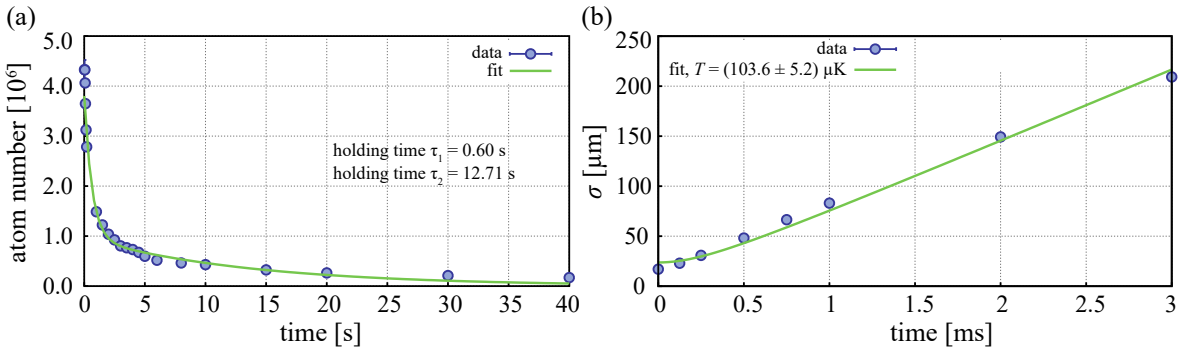

Fig. 4.8: (a) Measurement of the holding time inside the optical dipole trap in SODT configuration with 100 % of the available power of 72.6 W, showing a double exponential progression of the atom number vs holding time. The fast decay caused by natural evaporation exhibits a time constant of $\tau_1 = 0.60$ s, while the causes for the slower decay with time constant $\tau_2 = 12.71$ s were not entirely understood (see text). (b) Temperature measurement of the atomic ensemble inside the SODT after a holding time of 200 ms at maximum power of $P_{\text{init}} = 72.6$ W via TOF. The atoms get heated (cf. Fig. 4.3) to a temperature of $(103.6 \pm 5.2)\,\mu$K during loading.

turned on at the beginning of the compression phase of the MOT, aligns the atomic dipoles and preserves the spin-polarization that formed in the cMOT, as described in Sec. 2.3.2.

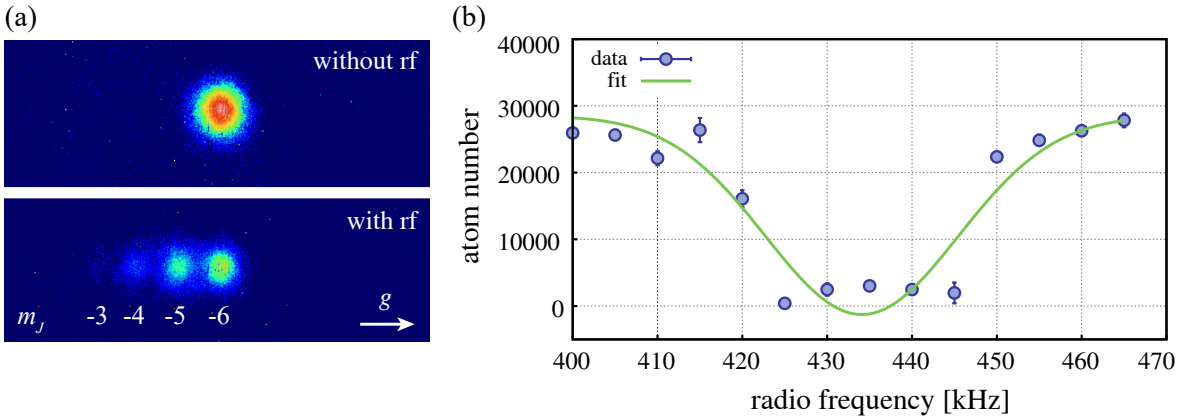

Fig. 4.9: (a) Stern-Gerlach type experiment for an ultracold erbium atomic ensemble without (upper panel) and with applied rf signal (lower panel). After an evaporation process and subsequent switch-off of the ODT the atoms freely expand while a magnetic field gradient of roughly 3.8 G/cm is applied, followed by absorption imaging. If no rf signal is applied, the atoms do not spatially separate, indicating full spin-polarization of the ensemble. For confirmation an rf signal is applied during the same measurement process as before, now transferring atoms into other m_J states, leading to a spatial splitting of the atomic ensemble by the magnetic field gradient. In both panels gravity points in the right direction. (b) Measurement of the radio frequency resonance for which most atoms are transferred into other m_J states. For this the frequency of the rf signal is varied for each Stern-Gerlach measurement. The here obtained result of (434 ± 1) kHz can be used to determine the absolute magnetic field at the position of the atomic ensemble, yielding (0.267 ± 0.001) G.

To further investigate this behaviour a radio frequency (rf) signal was additionally applied to the atoms during the Stern-Gerlach type experiment via a coil sitting centrally on top of

the main vacuum chamber. Here the rf signal at a frequency of 434 kHz with an amplitude of −4 dBm was applied for 2 ms during a portion of the holding time. The rf signal transfers the atoms from the $m_J = -6$ state into other Zeeman states mainly with $m_J = -5, -4$ and -3 respectively, leading to a Stern-Gerlach separation that can be seen in the lower panel of Fig. 4.9(a). This measurement confirms the assumption that the atomic ensemble exhibits full $m_J = -6$ spin-polarization.

Additionally it is possible to determine the absolute magnetic field at the position of the atomic cloud, which is relevant to know, if one, for example, wants to avoid Feshbach resonances of atomic erbium that start at 0.9 G [30, 36, 71], as those can act detrimentally on the ODT holding time via increase of collision rates as well as inelastic processes [31]. The radio frequency reducing the atom number of the ensemble in $m_J = -6$ states most effectively was found by varying the frequency and fitting a Lorentzian to the measured data, shown in Fig. 4.9(b). With the resulting center frequency of 434 kHz the absolute magnetic field can be calculated via Eq. 2.16 as approximately 0.267 G, which is sufficiently low to not experience any Feshbach resonances. Note that the offset magnetic fields employed during the experimental cycle in the region of several G (cf. Figs. 4.1 and 4.4) do not reflect the absolute magnetic field in the main chamber as they are used to counter strong residual magnetic fields. As this measurement reveals, those offset magnetic fields reduce the overall magnetic field successfully to a value much below field strengths required for Feshbach resonances in the atomic erbium case.

Another experimental investigation involved the question if the atomic ensemble can be transferred from the $m_J = -6$ state to a fully spin-polarized sample in the $m_J = +6$ state without too much losses, if for any reasons this configuration might become convenient in future experimental steps or a comparison between different spin-polarized samples becomes an area of interest. For this the amplitude of the rf signal at 434 kHz was increased to approximately +1.2 dBm. Fig. 4.10(a) shows a normal absorption image of the ultracold atomic ensemble without neither magnetic field gradient nor rf signal, which defines the zero position in space. Fig. 4.10(b) depicts a Stern-Gerlach type experiment with applied magnetic field gradient, with the atomic ensemble being in the $m_J = -6$ Zeeman state, similar to the upper panel of Fig. 4.9(a), showing a displacement from the zero position defined in Fig. 4.10(a). If the strong rf signal is additionally applied approximately all atoms that are not lost in the rf driving process are transferred into the $m_J = +6$ Zeeman state, leading to the same absolute displacement, but now in the opposite direction, as seen in Fig. 4.10(c). The observed transfer efficiency from $m_J = -6$ to +6 amounts to roughly 33 %.

4.3 Evaporative cooling of atoms

To reach the phase transition to a Bose-Einstein condensate (BEC), spin-polarized atoms loaded from the cMOT into the ODT are evaporatively cooled by ramping down the trap potential according to Eq. 2.50, with details for SODT and HCODT configuration respectively found below. A phase transition to a BEC is indicated, and further discussed in Sec. 4.4.

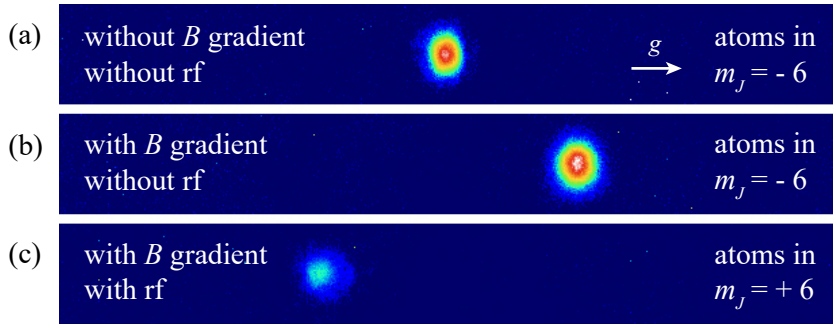

Fig. 4.10: (a) Absorption image of an atomic ensemble after evaporation without added magnetic field gradient or rf signal, defining a zero point in space. Atoms are spin-polarized in the $m_J = -6$ Zeeman state. (b) Stern-Gerlach type experiment similar to the case depicted in the upper panel of Fig. 4.9(a), showing a displacement from the zero point. As no rf signal is applied here, the atoms remain in the $m_J = -6$ state. (c) Stern-Gerlach type experiment with added strong rf signal, transferring a portion of approximately 33 % of the atoms into the $m_J = +6$ Zeeman state. This is confirmed by the position of the atomic ensemble, which exhibits the same absolute displacement from the zero point, but now in the opposite direction, while considering the influence of gravity. In all panels gravity points in the right direction.

4.3.1 Evaporation ramp

The used temporal evolution of the CO_2 laser beam trapping potential is given by Eq. 2.50 and therefore dependent on the cut-off parameter η, the collision rate γ, the initial trap depth U_0, and the end trap depth $U(t_{\mathrm{end}})$. The cut-off parameter should stay constant during the complete evaporation process, as discussed in Sec. 2.3.4. As the maximal trap depth provided by the CO_2 laser beam amounts to approximately $U_{0,\mathrm{init,CO_2}} = 2.1\,\mathrm{mK/k_B}$, and the temperature of the atomic ensemble in the SODT right after loading from the cMOT lies in the region of $100\,\mu$K (cf. Fig. 4.8), initial optimization started with $\eta = 21$, and was finally set to 7.25. Due to the addition of the Nd:YAG beam in HCODT configuration and therefore an relative increase of the total potential depth in the later stages of the evaporation cycle, and the fact that collisions with the residual background gas modify the temporal evolution, it is imperative to optimize η experimentally. The order of magnitude for the starting parameter of γ is known from previous work [56] and gets also experimentally optimized to a final value of 325.

In HCODT configuration the Nd:YAG laser beam joins the evaporation process at a variable time $t_{\mathrm{YAG,start}}$ after the evaporation process via lowering of the CO_2 laser beam power has started (cf. Fig. 4.4), calculated by

$$t_{\mathrm{YAG,start}} = -\left(\frac{U_{0,\mathrm{init,YAG}}}{\mathrm{scal}_U U_{0,\mathrm{init,CO_2}}}\right)^{-1/\beta}\left(\frac{U_{0,\mathrm{init,YAG}}}{\mathrm{scal}_U U_{0,\mathrm{init,CO_2}}}\right)^{1/\beta-1}\tau_{\mathrm{evap}}, \tag{4.2}$$

where $\beta = 2(\eta' - 3)/\eta'$, and $\mathrm{scal}_U = U_{0,\mathrm{YAG}}/U_{0,\mathrm{CO_2}}$ which (if not stated otherwise) is set to 0.5. The full temporal evolution of the trap potential depth provided by the Nd:YAG laser beam is chosen as

$$U_{0,\mathrm{YAG}}(t) = \begin{cases} U_{0,\mathrm{init,YAG}}, & t < t_{\mathrm{YAG,start}} \\ \mathrm{scal}_U U_{0,\mathrm{CO_2}}(t), & t \geq t_{\mathrm{YAG,start}} \end{cases}. \tag{4.3}$$

A constant scaling factor scal_U was introduced so that the trap potential shape does not vary significantly during the evaporation power ramp of both beams. The temporal evolution of the crossed beam trap potential $U_{\mathrm{dip}}^{\mathrm{cross}}(x,y,z,t)$ (HCODT configuration) as seen in Eq. 2.45 for the static case is then given by $U_{\mathrm{YAG}}(x,y,z,t)+U_{\mathrm{CO_2}}(x,y,z,t)$, where $U_{0,\mathrm{CO_2}}$ and $U_{0,\mathrm{YAG}}$ become time-dependent. The needed power of both laser beams during evaporation can be calculated via Eq. 2.41. From the cutoff parameter η and Eq. 2.50 the temperature T of the atomic ensemble inside the optical trap potential should follow according to $T(t)/T_{\mathrm{init}} = U_0(t)/U_{0,\mathrm{init}}$.

As mentioned in Sec. 2.3.4 the optical trap potential stemming from the CO_2 and Nd:YAG laser beams is modified by gravity and an external magnetic field gradient, which can have an effect for small trap potential depths. The resulting effective trap potential can be determined experimentally by measuring the acceleration $a_{\mathrm{tot}} = g + a_{\mathrm{SG}}$ caused by gravitation and applied magnetic field gradient in free fall. As g is known, the Stern-Gerlach like acceleration a_{SG} can be obtained. Within the scope of earlier work for the here presented setup this magnetic acceleration was determined to be $a_{\mathrm{SG}} = (0.74 \pm 0.08)\,\mathrm{m/s^2}$, although also a measured acceleration of $(0.57 \pm 0.01)\,\mathrm{m/s^2}$ without applied magnetic field gradient indicated the presence of a weak residual magnetic field gradient inside the main chamber [97]. Interestingly in older works of our group without a supplementary Nd:YAG laser trapping beam, the magnetic acceleration amounted to a much higher value of $(8.93 \pm 1.80)\,\mathrm{m/s^2}$, which had to be employed to deal with the weaker spatial confinement of the single beam trap [56]. The total trap potential is modified as described at the end of Sec. 2.3.4.

4.3.2 Characterization of the atomic ensemble during evaporation

After loading from the cMOT into the ODT and a subsequent holding time of 200 ms the erbium atomic ensemble was evaporatively cooled as described in Sec. 4.3.1. For the characterization of this evaporation process the atom number as well as the temperature of the atomic ensemble were measured at different points in time during evaporation.

Atom number during evaporation

The temporal evolution of the atom number during the evaporation phase is depicted in Fig. 4.11 for the case of the hybrid crossed optical dipole trap for the full evaporation scheme in (a), as well as only the later part of evaporation with the CO_2 laser beam's power below 1 % of its initial power in (b), and Fig. 4.12 for both configurations (single and hybrid crossed optical dipole trap respectively) for the later part of evaporation. Atom numbers were in all cases measured via absorption imaging. At the same end power of the CO_2 laser beam the HCODT configuration provides a higher number of trapped atoms due to additional trap depth contributions from the Nd:YAG laser beam and a stronger confinement respectively. For higher end powers the SODT traps a higher amount of atoms, which might be due to the fact that the introduction of the Nd:YAG cross trap beam separates the colder atoms in the center (or beam waist) region of the CO_2 laser beam from hotter atoms located further away from the beam waist of the cigar-shaped CO_2 laser beam, which are then not trapped in the HCODT and rethermalize to a higher temperature, thus leaving the trap.

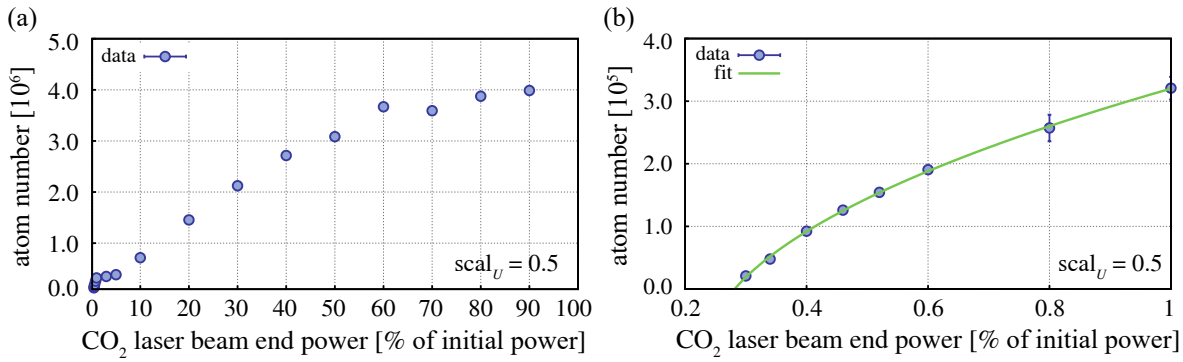

Fig. 4.11: (a) Measurement of the atom number as a function of the CO_2 laser beam power P_{end} at the end of evaporation, with initial power of $P_{\mathrm{init}} = 72.6\,\mathrm{W}$, in HCODT configuration (with $\mathrm{scal}_U = 0.5$), showing the full range of the evaporation phase. (b) Same measurement settings as in (a), but now with a detailed view on the later stages of the evaporation phase with low CO_2 laser beam end powers. A function of form $N_{\mathrm{atom}}(P_{\mathrm{end}}) \propto \sqrt{P_{\mathrm{end}} - P_{\mathrm{zero}}}$ is fitted to the measured data, with P_{zero} being the (theoretical) end power at which no atoms are trapped anymore.

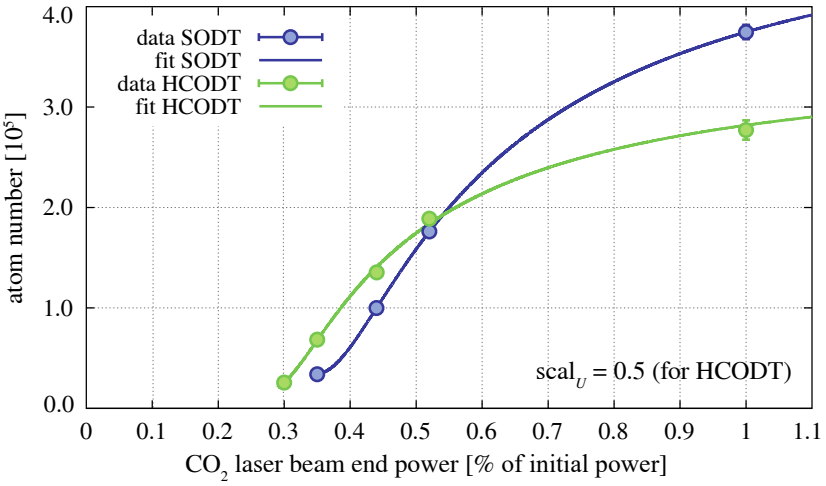

Fig. 4.12: Measurement of the atom number as a function of the CO_2 laser beam power P_{end} at the end of evaporation, with initial power of $P_{\mathrm{init}} = 72.6\,\mathrm{W}$, in SODT (blue) as well as HCODT (green) configuration (with $\mathrm{scal}_U = 0.5$) respectively. In contrast to Fig. 4.11 the data here was aggregated from various measurements (e.g. of trap frequencies, ensemble temperatures, ensemble lifetimes and condensate fractions respectively) which as a by-product yielded the corresponding atom numbers. The data of those measurements was then averaged, with the standard deviation used as the error. Functions of form $N_{\mathrm{atom}}(P_{\mathrm{end}}) = N_{\mathrm{init}} \cdot (e^{-a/(P_{\mathrm{end}}-P_{\mathrm{zero}})} + 1 - e^{-b/P_{\mathrm{end}}})$ were fitted to each data series, chosen by convenience to accurately illustrate the progression. Here P_{zero} is the (theoretical) evaporation end power at which no atoms are trapped anymore, and a and b are fit coefficients respectively. The HCODT configuration shows a higher atom number for CO_2 laser beam powers below 0.52 % of P_{end} in comparison to the SODT configuration, while for higher end powers this effect reverses (for possible reasons, see text).

Temperature during evaporation

Time-of-flight (TOF) measurements were performed, similar to the case in Fig. 4.3, only here for different powers P_{end} of the CO_2 laser beam at the end of evaporation, to determine

the temporal progression of the temperature of the atomic ensemble during the evaporation process. Fig. 4.13 shows the results for three different configurations in the low end power regime: single optical dipole trap ($\mathrm{scal}_U = 0.0$) and hybrid crossed optical dipole trap for two different scaling factors between the trap depths of both beams ($\mathrm{scal}_U = 0.5$ and 1.0) respectively. As the start of the phase transition to a BEC was observed in this measurement, the critical temperature could be determined to be $T_{\mathrm{c,exp}} = (169.3 \pm 20.9)\,\mathrm{nK}$.

With the knowledge of the progress of trap frequencies (cf. Sec. 4.2.2), atom number and temperature of the atomic ensemble during evaporation, the phase space density during this experimental phase can be determined, with the results presented in Sec. 4.4.2.

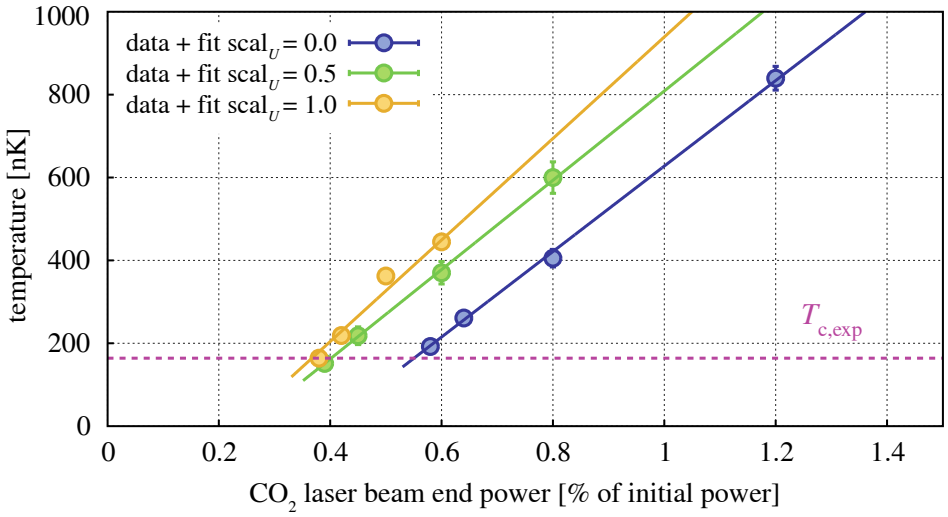

Fig. 4.13: Measurement results for the temperature of the atomic ensemble during the evaporation process. Each plotted data point was obtained from a TOF measurement after reaching the corresponding CO_2 laser beam power P_{end} at the end of evaporation, performed for three different settings: in SODT configuration (with $\mathrm{scal}_U = 0.0$), as well as in HCODT configuration with two different trap depth ratios $\mathrm{scal}_U = 0.5$ and 1.0 respectively. Atoms trapped in HCODT configuration possess a higher temperature for the same CO_2 laser beam end power, which is understood as the total trap depth is higher due to the contribution of the Nd:YAG laser beam. Linear functions of form $T(P_{\mathrm{end}}) = m_T P_{\mathrm{end}} + T_{\mathrm{off}}$ were fitted to each data set, where m_T denotes the slope and T_{off} the temperature offset at which the fitted function crosses the y-axis respectively. Measurements were performed until a transition to a BEC became noticable due to the emergence of a bimodal density distribution (s. Sec. 4.4.1 for details). From this the (averaged) critical temperature $T_{\mathrm{c,exp}}$ can be estimated as $(169.3 \pm 20.9)\,\mathrm{nK}$, where the error was obtained from the standard deviation of the three data sets. This is slightly above the theoretical value, calculated from Eq. 2.10 to be $T_{\mathrm{c,theo}} = 136\,\mathrm{nK}$. Finite-size effects would decrease the theoretical result by roughly $4\,\mathrm{nK}$, while interaction effects can in principle be larger, but would also only reduce the theoretical critical temperature. Density fluctuations however increase the theoretical critical temperature, in the case of s-wave scattering by about $4\,\mathrm{nK}$ [138], cancelling finite size effects in this case, so that these effects should not play a role for the discrepancy. Systematic measurement errors on the one hand as well as d-wave scattering contributions on the other hand could, however, be a cause for the observed discrepancy.

4.4 Bose-Einstein condensation of erbium atoms

By means of the evaporation process characterized in the previous section, the transition to quantum degeneracy was successful, leading to the generation of an erbium atomic Bose-Einstein condensate (BEC) in an optical dipole trap either consisting of a single CO_2 laser beam (SODT configuration), or of a hybrid crossed beam setup provided by the CO_2 laser beam and an additional Nd:YAG laser beam (HCODT configuration). Atom numbers in the pure condensate usually amount up to $3.5 \cdot 10^4$. This section presents work to search for signatures of the phase transition to a BEC, namely by bimodal density distribution measurements as well as phase space density calculations from measurement data. Subsequently the lifetime of the ultracold atomic ensemble is characterized, and a brief note regarding the long-term stability of the experiment is given.

4.4.1 Bimodal density distribution

To verify the successful generation of a BEC, the spatial density distribution can be measured for different times during the evaporation process. If a transition to quantum degeneracy occurs, the density distribution should change from a Maxwell-Boltzmann distribution to a bimodal distribution, which should then revert back to a monomodal distribution when all trapped atoms reach quantum degeneracy during evaporation [6]. Fig. 4.14 shows four such measurements during evaporation, i.e. for different end powers of the trapping beams, in HCODT configuration. One clearly observes the emergence of bimodality in panels (b) and (c), while for further evaporation shown in (d) the density distribution reverts back to a monomodal distribution, indicating a macroscopic occupation of the ground state. The form of the density distribution for a BEC is determined by the trap potential shape [6]. As here the harmonic trap potential exhibits a nearly parabolic shape for cold atoms sitting in the bottom region of the potential, the resulting density distribution is of inverted parabolic form (yellow curves).

If one plots the condensate fractions obtained via measurement methods discussed in Fig. 4.14 for various trap depth ratios $\mathrm{scal}_U = U_{0,\mathrm{YAG}}/U_{0,\mathrm{CO_2}}$, one obtains the results depicted in Fig. 4.15.

4.4.2 Phase space density

The phase space density can be determined via several experimentally accessible parameters according to Eq. 3.7. As shown in Fig. 4.16, it exceeds the critical phase space density of 2.612 during evaporation with a sudden increase, and reaches values of up to 61 ± 55 in SODT configuration, and 9.8 ± 6.5 in HCODT configuration respectively, confirming the generation of an atomic erbium Bose-Einstein condensate, which was observed in situ in Fig. 4.14. Corresponding measured experimental quantities are listed in Tab. 4.1.

A third method to detect the generation of a BEC, the observation of a radius inversion after free expansion of the condensate due to a repulsive interaction between the atoms [40, 59], could for the here used crossed dipole trapping geometry not be reliably observed, other than in earlier measurements with a single CO_2 laser beam dipole trap [56]. In the hybrid crossed optical dipole trap setup the spatial distribution of atoms is more spherically symmetric, while

P_{CO_2} [%]	0.35	0.44	0.52	1.00	3.00	10.00
scal_U	0.0	0.0	0.0	0.0	0.0	0.0
N [10^3]	33.9 ± 0.8	100.0 ± 0.9	176.0 ± 2.0	374.7 ± 7.0	686.9 ± 13.7	1305 ± 15
$\nu_{y,\text{K}}$ [Hz]	156 ± 2	195 ± 1	209 ± 1	296 ± 1	467 ± 7	700 ± 15
$2\nu_{r,\text{AM}}$ [Hz]	336 ± 1	388 ± 3	407 ± 1	554 ± 1	844 ± 3	1303 ± 3
$\nu_{r,\text{AM}}$ [Hz]	140 ± 1	177 ± 3	197 ± 1	268 ± 1	452 ± 2	678 ± 4
$2\nu_{z,\text{AM}}$ [Hz]	37 ± 9	46 ± 1	48 ± 1	61 ± 1	85 ± 1	132 ± 1
$\nu_{z,\text{AM}}$ [Hz]	18 ± 2	22 ± 1	15 ± 5	30 ± 4	53 ± 16	68 ± 10
T (nK)	–	50 ± 14	133 ± 16	628 ± 31	2690 ± 94	–
ρ	–	61 ± 55	4.8 ± 3.4	0.36 ± 0.11	0.041 ± 0.013	–
P_{CO_2} [%]	0.30	0.35	0.44	0.52	1.00	
scal_U	0.5	0.5	0.5	0.5	0.5	
N [10^3]	25.7 ± 1.2	68.4 ± 1.9	135.4 ± 3.8	188.7 ± 3.9	277.1 ± 9.6	
$\nu_{y,\text{K}}$ [Hz]	134 ± 1	167 ± 1	196 ± 1	211 ± 1	300 ± 1	
$2\nu_{r,\text{AM}}$ [Hz]	307 ± 2	353 ± 2	378 ± 1	407 ± 1	557 ± 2	
$\nu_{r,\text{AM}}$ [Hz]	132 ± 1	160 ± 1	182 ± 1	198 ± 1	274 ± 4	
$2\nu_{z,\text{AM}}$ [Hz]	46 ± 5	56 ± 1	61 ± 4	72 ± 1	123 ± 1	
$\nu_{z,\text{AM}}$ [Hz]	31 ± 9	31 ± 2	32 ± 4	36 ± 1	68 ± 2	
T [nK]	54 ± 6	108 ± 7	205 ± 9	291 ± 10	809 ± 20	
ρ	9.8 ± 6.5	4.8 ± 1.4	1.8 ± 0.5	1.2 ± 0.2	0.30 ± 0.01	

Tab. 4.1: Relevant quantities of the atomic ensemble captured in the optical dipole trap during evaporation for different CO_2 laser beam end powers P_{CO_2}, given as a percentage from the initial power of $P_{CO_2,\text{init}} = 72.6\,\text{W}$, for SODT ($\text{scal}_U = 0.0$) and for HCODT ($\text{scal}_U = 0.5$) configuration respectively. The measured number of atoms N, the trap frequencies ν_i stemming from Kohn breathing mode (K) as well as from amplitude modulation (AM) measurements respectively, and the temperatures T extracted from time-of-flight measurements are given. From those values the phase-space densities ρ were calculated via Eq. 3.7. Errors on the temperature values come from the propagation of uncertainty of the linear temperature fits (cf. Fig. 4.13), and errors on the trap frequencies stem from the fitting process, while errors on the atom number are of statistical nature. These lead due to propagation to the given errors on the phase space density. Systematic uncertainties are not provided in this table, but are expected to lie in the same order of magnitude as the listed errors.

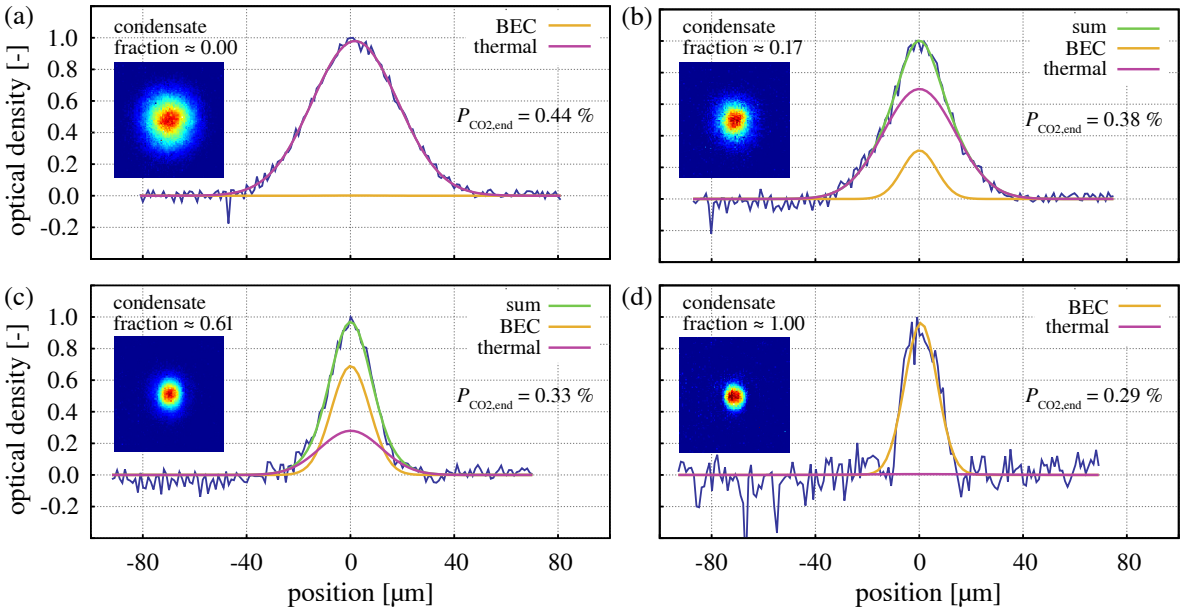

Fig. 4.14: Measurement of the optical density distribution for various CO_2 laser beam evaporation end powers in HCODT configuration (with $\mathrm{scal}_U = 0.5$). Shown are intersections of the radial density distribution of the trapped atomic ensemble (blue). All measurements were normalized to 1 for maximum optical density. Condensate fractions $A_{\mathrm{BEC}}/(A_{\mathrm{BEC}} + A_{\mathrm{thermal}})$ were determined from the areas A_i below curves i. The insets show averaged absorption images over five measurements, with the plotted intersections corresponding to a single measurement from each series. (a) Optical density distribution for a CO_2 laser beam end power $P_{\mathrm{CO_2,end}} = 0.44\,\%$ of the initial beam power of 72.6 W, showing a Maxwell-Boltzmann distribution (purple curve) of the purely thermal atomic ensemble. (b) Emergence of bimodality in the density distribution in form of a parabolically shaped portion (yellow curve) sitting on top of the Maxwell-Boltzmann distributed thermal cloud, here shown for a CO_2 laser beam end power of 0.38 %. The sum of Maxwell-Boltzmann and parabolic distribution is plotted as the green bimodal density distribution curve. (c) Further increase of the condensate fraction by lowering the trap depth during the evaporation phase, here with an end power of 0.33 %. (d) Fully condensed atomic ensemble with a monomodal parabolic density distribution at an end power of 0.29 %.

in single beam optical dipole traps the atomic cloud is more cigar-shaped, which might be a reason for no clear radius inversion to occur here. Another possible explanation could be the specific arrangement of homogeneous (offset) magnetic fields and magnetic field gradients inside the main vacuum chamber, which differs significantly from the previous setup, and the resulting change of dipolar interaction effects in the atomic ensemble, possibly leading to spatial distortions of the cloud, as also observed in other work [30]. For ultracold erbium atoms, the van-der-Waals interaction, determined by the s-wave scattering length, and the long-range, non-isotropic dipole-dipole interaction are of same order of magnitude [139], so that for a radius inversion to occur, the interaction between atoms has to be repulsive (where maximum repulsiveness is achieved for an exact parallel alignment of atomic dipoles), which might have not been fulfilled in this particular setup.

4.4.3 Condensate holding time

A sufficiently high lifetime of the BEC inside the optical dipole trap is crucial for further experimental steps. To determine the holding time, the atomic ensemble was measured for

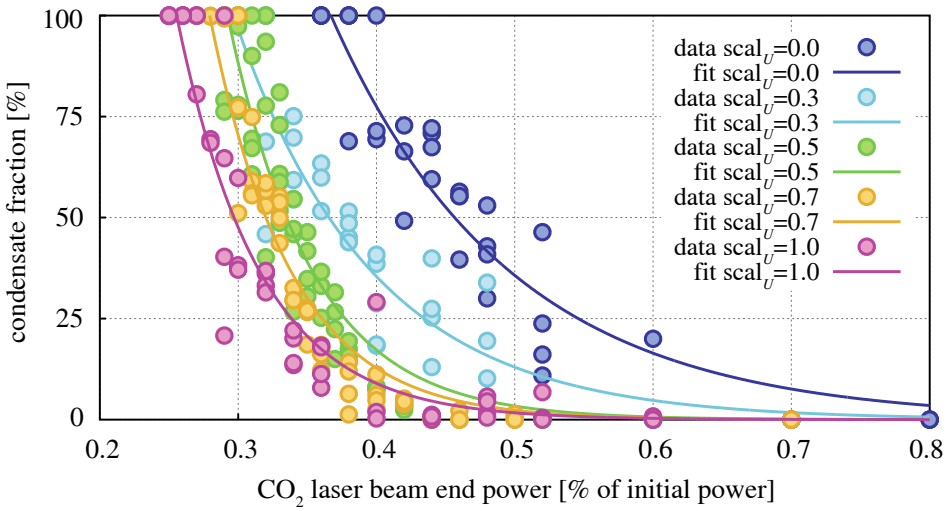

Fig. 4.15: Measurement results for the condensate fraction at different CO_2 laser beam powers at the end of evaporation for various trap depth ratios $\mathrm{scal}_U = U_{0,\mathrm{YAG}}/U_{0,\mathrm{CO_2}}$. The initial power of the CO_2 laser beam amounts to 72.6 W. Functions are fitted by convenience to illustrate the progression of the condensate fraction during evaporation. The higher the trap depth ratio is, the lower the CO_2 laser beam end power can be for reaching a pure condensate, which is understood from the trap depth contributions and added confinement provided by the Nd:YAG cross trapping beam. Accordingly for HCODT configuration (with $\mathrm{scal}_U > 0$) the phase transition to a pure BEC happens in a smaller CO_2 laser beam end power interval than for SODT configuration, for the same reasons stated before.

different trap potential depths at end of evaporation, seen in Fig. 4.17(a). As the condensate fraction for those measurements were also determined, the holding time can also be plotted against it, as shown in Fig. 4.17(b). The measurements were performed for SODT configuration ($\mathrm{scal}_U = 0.0$) as well as for two different HCODT configurations ($\mathrm{scal}_U = 0.5$ and 1.0) respectively. In general the holding time of the condensate decreases with increasing involvement of the Nd:YAG cross trap beam, which could have two reasons. The first cause could be erbium's higher scattering rate for laser light at 1064 nm in comparison to the very far-detuned CO_2 laser light at 10.6 μm, while the second cause could be the higher occurance of three-body collisions due to a possibly higher spatial atomic density in the hybrid crossed optical dipole trap. Collisions with the background gas however seem not to be a cause, as trap lifetimes for the here employed ultra-high vacuum are in the order of 30 s.

Typical holding times for a full condensate lie in the region of 12 s for SODT configuration, and between 8 to 10 s for HCODT configuration respectively. This is an improvement to earlier work, which determined the BEC holding time in SODT configuration to be (8.7 ± 0.9) s, by roughly 30 %. As the HCODT achieves a similar holding time as the SODT in earlier work, although here the scattering rate and the occurance of three-body collisions are possibly higher, consequentially the confinement was apparently proportionally increased for successful trapping with comparable parameters.

4.4.4 Long-term stability

A big advantage of the hybrid crossed optical dipole trap setup compared to a single beam optical dipole trap setup is the enhanced long-term stability of the experiment, leading to less

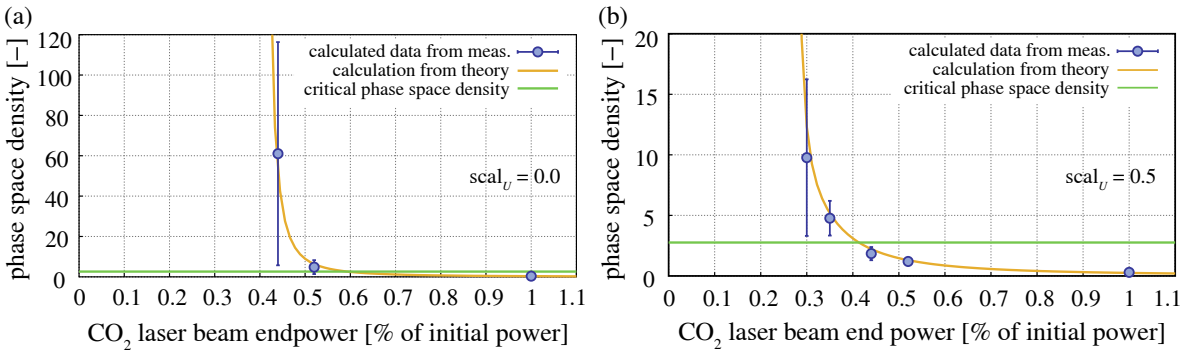

Fig. 4.16: Progression of the phase space density during the evaporation process for different CO_2 laser beam end powers as a percentage from the initial power $P_{\mathrm{init}} = 72.6\,\mathrm{W}$. Shown are data points calculcated from measurements results (blue) according to Tab. 4.1, as well as curves calculated from indirect measurements, theoretical values and fits (yellow), for optical dipole traps in (a) SODT ($\mathrm{scal}_U = 0.0$) and (b) HCODT ($\mathrm{scal}_U = 0.5$) configuration respectively. For the curves the trap frequencies were indirectly calculated from the measured beam waists via knife-edge method at a particular beam power instead of measuring them directly by Kohn breathing mode or amplitude modulation techniques, and subsequently calculated for all CO_2 laser beam end powers via $\nu(\mathrm{P_{end}}) \propto \sqrt{\mathrm{P_{end}}}$. For the temperature and atom numbers respectively, continuous values were obtained from fits shown earlier. The comparatively large errors on data points above the critical phase space density for a Bose-Einstein condensate (plotted as a green line) stem mainly from significant errors on low temperatures as well as axial trap frequencies for small trap potential depths, exacerbated by means of error propagation. However the data points including error margins at end of evaporation lie above the critical phase space density defined in Eq. 2.11, confirming the formation of a BEC discussed in Sec. 4.4.1. For the hybrid crossed optical dipole trap configuration the CO_2 laser beam power range, in which the phase space density including errors lies above the critical value, is roughly 50 % larger than for the single beam optical dipole trap, leading to a more stable long-term setup as here fluctuations of the CO_2 laser beam power have a lower impact on the BEC. Relative power drifts and fluctuations for the Nd:YAG laser beam have generally been found to be lower than for the CO_2 laser beam.

everyday maintenance efforts in the laboratory, and a better reproducibility of measurement results compared to older setups. As discussed in the context of Fig. 4.16, for the HCODT configuration the CO_2 laser beam power range, in which the phase space density including errors lies above the critical value, is roughly 50 % larger than for SODT configuration. Thus fluctuations and drifts of the CO_2 laser beam power have overall a lower impact on the BEC size than in the single beam optical dipole trap case, as for the cross Nd:YAG laser beam relative power drifts and fluctuations have in general been found to be much lower.

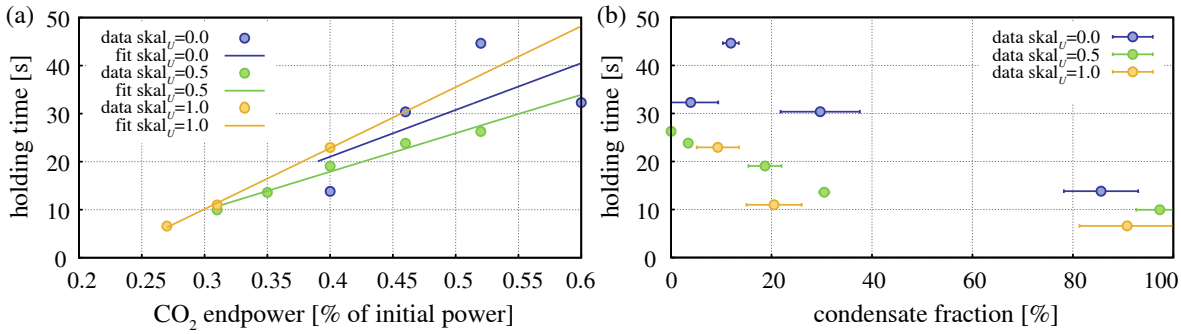

Fig. 4.17: Holding time measurement of the atomic erbium Bose-Einstein condensate in the optical dipole trap potential. (a) Shown is the holding time of the condensate for different CO_2 laser beam end powers, given as a percentage value from the initial power of $P_{\mathrm{init}} = 72.6\,\mathrm{W}$, for three data series: one in SODT configuration (with $\mathrm{scal}_U = 0.0$), and two in HCODT configuration (with $\mathrm{scal}_U = 0.5$ and 1.0) respectively. Fitted are linear functions to describe the progression of the holding time in the low trap potential depth regime. (b) Plotted is the same holding time data series as in (a), but here linked with values from corresponding condensate fraction measurements. Typical holding times of a full condensate lie in the region of 12 s (SODT), and 8 to 10 s (HCODT), showing an improvement from older setups.

5 Prospects for synthetic magnetic fields for ultracold erbium atoms

In this part of the thesis a theoretical treatment of synthetic magnetic fields for electrically neutral bosonic erbium atoms, strong enough to reach the fractional quantum Hall regime, is presented. After an introduction of the general concept and a review of the better known case of gauge fields for charged particles, firstly the simpler three-level atomic system will be discussed, after which the more complex atomic erbium case is treated. Here a parameter regime is given, for which strong synthetic magnetic fields with good spatial homogeneity are predicted. Finally an estimation of the Laughlin gap, the energetic gap between the lowest and the other remaining Landau levels of a two-dimensional atomic erbium microcloud in the synthetic magnetic field, expected from the s-wave contribution of the interaction is presented. The main findings in this chapter were also published in [50].

5.1 Introduction to synthetic gauge fields

Ultracold atomic clouds are extremely well-suited systems to study matter behaviour, as those systems are pure and controllable to a high degree. Atoms are electrically neutral, which is usually an advantage for many experimental studies. For the study of some currently very interesting phenomena as the fractional and integer quantum Hall effect [140], the spin Hall effect [141, 142] and topological insulators [143] an analogon of the Lorentz force is needed, which is present for electrically charged electrons in a magnetic field. To overcome this limitation artificial gauge fields can be constructed, imitating a circular motion of particles subject to the synthetic gauge field leading to the introduction of a Berry phase (analogous to the Aharonov-Bohm phase), and thus creating a Lorentz force equivalent [144, 145]. Techniques include trap rotation [146, 147], lattice shaking [148], or phase imprinting via photon recoil [46, 149–154]. Since trap rotation and lattice shaking techniques historically produced only comparably weak synthetic magnetic fields, in this thesis the possibility of the generation of strong artificial gauge fields for neutral lanthanide erbium atoms with a non-vanishing angular orbital momentum L in their ground state by phase imprinting via Raman manipulation beams is theoretically investigated.

Current implementations of such synthetic magnetic fields (for e.g. alkali atoms with their $L = 0$ S-electronic ground state) are not strong enough for fractional quantum Hall states to form, mainly because of limitations of the achievable coherence time, caused by the impossibility to detune the Raman light field further away from resonance than the electronic fine structure splitting of the excited states. However, another readily available Bose-Einstein condensated lanthanide atomic species is dysprosium, for which a similar, yet different scheme for artificial magnetic fields was proposed [49], which recently was utilized for theoretical investigations of dysprosium topological quantum Hall systems [51]. Further atomic species with a suitable P-electronic ground state as the oxygen atom are difficult to laser cool due to

technical inconvenient UV electronic transition wavelengths and a large number of required repumping lasers.

Instead of looking at atoms circulating in a lattice and accumulating a Peierls phase [155], our system is composed of a bulk gas whose atoms are adiabatically transferred to dressed states by altering the bandstructure. While the here presented system as well as earlier published work construct Abelian gauge fields [46], (synthetic) gauge fields can also be extended to the non-Abelian case [156], e.g. to study spin-orbit coupling [157, 158] leading to the spin Hall effect [159].

5.1.1 Review: Gauge fields for charged particles

To establish the basic concept the case of gauge fields in classical electrodynamics is discussed. The electric and magnetic (gauge) fields, $\mathbf{E}$ and $\mathbf{B}$, can be described by the vector and scalar potentials, $\mathbf{A}$ and ϕ:

$$\mathbf{E} = -\nabla\phi - \frac{\partial \mathbf{A}}{\partial t}, \qquad \mathbf{B} = -\nabla \times \mathbf{A}. \tag{5.1}$$

Here $\mathbf{A}$ and ϕ are only defined up to a gauge, meaning that certain constraints can be specified for them, leaving the resulting interaction of the particles in the gauge field unchanged – or invariant to the gauge. In a magnetic field $\mathbf{B}$ particles with mass m, charge q, and velocity $\mathbf{v}$ then experience the Lorentz force $\mathbf{F} = q\mathbf{v} \times \mathbf{B}$, which can also be expressed as the Hamiltonian [160]

$$\hat{H} = \frac{(\mathbf{p} - q\mathbf{A})^2}{2m} + q\phi, \tag{5.2}$$

where $\mathbf{p}$ is the canonical momentum operator, originating from the replacement for a free particle $\mathbf{p} \to \mathbf{p} - q\mathbf{A}$, in which an additional term $-q\mathbf{A}$ is introduced into the dispersion relation of the particle. As we are especially interested in the strength of the (synthetic) magnetic field, the cyclotron frequency is an important quantity. For e.g. a uniform magnetic field $\mathbf{B} = B\mathbf{e}_z$ along the z-axis, the cyclotron frequency of the circular motion a particle with charge q experiences in the $x-y$-plane can be defined as

$$\omega_\mathrm{c} = \frac{|q|B}{m}. \tag{5.3}$$

The minimal cyclotron orbit size, called magnetic length, is then [161]

$$\ell_\mathrm{mag} = \sqrt{\frac{\hbar}{m\omega_\mathrm{c}}}, \tag{5.4}$$

which serves as a characteristic length scale for e.g. the determination of the vortex density in a given system. To later reach experimentally interesting regimes for the study of fractional quantum Hall states, the vortex density has to be higher than the atomic density in the system.

5.2 Synthetic magnetic fields for three-level atoms

To keep the discussion simple, the treatment is started by considering the generation of a synthetic magnetic field for a three-level atom with two stable ground state levels and an excited state in a Λ-configuration. This setup has similarities with the rubidium alkali case in [47], however here we assume a different polarization configuration of the Raman beams, and consider Raman transitions with a Zeeman quantum number difference of $\Delta m_\mathrm{F} = 2$.

5.2.1 Hamiltonian and dispersion relation

To begin with, a three-level atom with two stable ground state levels $|g_{+1}\rangle$ and $|g_{-1}\rangle$ and one spontaneously decaying excited state level $|e_0\rangle$ is considered, as shown in Fig. 5.1(b). The index denotes the corresponding Zeeman quantum number. The here suggested implementation follows the work of I. Spielman [47] developed for alkali atoms, however our approach chooses the atoms to be driven by two far-detuned counter-propagating laser beams in a $\sigma^+ - \sigma^-$ polarization configuration, which results in Raman coupling between ground state sublevels $|g_{+1}\rangle$ and $|g_{-1}\rangle$ with $\Delta m_\mathrm{F} = 2$. For comparison the scheme for rubidium alkali atoms used a $\pi - \sigma$ polarization configuration with $\Delta m_\mathrm{F} = 1$ coupling between sublevels.

The basic idea is to construct a Hamiltonian offering an atomic dispersion that mimics that of a charged particle in the presence of a position-dependent vector potential $\mathbf{A}^*$, so that a synthetic magnetic field $\mathbf{B}^* = \nabla \times \mathbf{A}^*$ emerges. Considering $\mathbf{A}^* = (A_x^*, A_y^*, A_z^*)$, the components A_i^* with $i = x, y, z$ themselves can be of scalar, vectorial or matrix-valued nature. Here only the case for $A_x^* \neq 0$ is regarded, so that $\mathbf{A}^* = (A_x^*, 0, 0)$ (Landau gauge). Note that the superscript $*$ denotes synthetic quantities to distinguish them from real ones, e.g. synthetic and real magnetic fields.

From Eq. 5.1 one can see that for a time-varying synthetic vector potential a synthetic electric field, and for the case of a spatially varying synthetic vector potential a synthetic magnetic field can be constructed. The latter can be achieved with a transversal gradient of the (real) magnetic field, which leads to a two-photon detuning $\delta = \omega_+ - \omega_- - \omega_\mathrm{Z}$, where ω_+ and ω_- denote the laser frequencies with corresponding polarizations, and $\hbar\omega_\mathrm{Z}$ is the energetic difference between $|g_{+1}\rangle$ and $|g_{-1}\rangle$ that is position-dependent. Both the magnetic field $\mathbf{B} = B_x\mathbf{e}_x$ and the counter-propagating laser beams are assumed to be oriented along the x-axis, and a magnetic field gradient along the y-axis, as seen in Fig. 5.1(c). This results in $B_x(y) = B_{0,x} + y\partial B_x/\partial y$, which realizes a position-dependent Raman detuning

$$\delta(y) = \Delta m_\mathrm{F} g \mu_\mathrm{B} \frac{\partial B_x}{\partial y} y, \tag{5.5}$$

where g is the atomic Landé g-factor and μ_B the Bohr magneton.

As the next step an experimentally tunable energy momentum dispersion relation $(\mathbf{p} - q\mathbf{A}^*)^2/(2m^*)$, with m^* as an effective mass for the motion along the x-direction, accounting for the differently shaped dispersion, has to be created. The momentum of the atoms in x-direction is identified as $\mathbf{p} = \hbar\mathbf{k} = \hbar k_x \mathbf{e}_x$, where $\mathbf{k}$ is the atomic wave vector, and k_x is the absolute value of the wave vector along $\mathbf{e}_x$. Here the dynamics of a free particle in y-direction and a strong confinement in z-direction are assumed, and hereinafter only the Hamiltonian

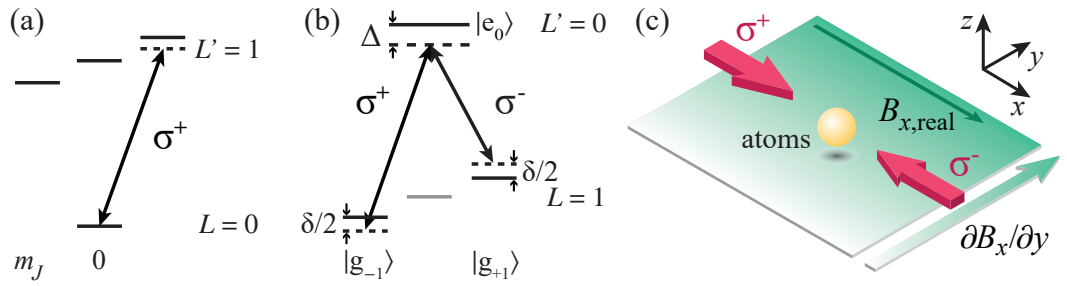

Fig. 5.1: Level schemes for two- and three-level atomic systems, respectively, as well as a schematic for the generation of synthetic magnetic fields. (a) Shown is a reduced level scheme of alkali atoms, with an S-electronic ground state ($L = 0$). (b) A reduced level scheme for a transition from a ground state with $L = 1$ to an electronically excited state with $L' = 0$ is depicted. This system gives an example for an electronic transition starting from a higher orbital angular momentum ground state, for which even with radiation far-detuned from the electronically excited state Raman transitions between different ground state spin projections become possible (the ground state $|g_0\rangle$ is shown in gray, because it is not relevant for the atom-light coupling here). Raman transitions with $\Delta m_\mathrm{F} = 2$ can be induced for the shown case of $L = 1$, when they are driven with a $\sigma^+ - \sigma^-$ optical polarization configuration. (c) Displayed is a schematic for synthetization of an artificial magnetic field for atoms using optical driving with two counter-propagating Raman beams and a transverse gradient of the (real) magnetic field.

in $\mathbf{e}_x$ is considered, which is possible due to the separability of the overall Hamiltonian. The light field consists of two counter-propagating Raman laser beams in the x-axis with wave vectors $\mathbf{k_1} \cong \mathbf{k_L} = k_\mathrm{L}\mathbf{e}_x$ and $\mathbf{k_2} \cong -\mathbf{k_L}$, where $\sim \pm 2\hbar k_\mathrm{L}$ momentum per Raman transition is transferred to the atoms, and $k_\mathrm{L} = 2\pi/\lambda$. In reality there will be a very small angle ϕ between both beam axes so that the effective single-photon recoil momentum amounts to $k_\mathrm{L} = \pi/(\lambda\cos(\phi/2))$. For our purposes $\phi = 0$ is assumed. The laser electric field is defined as

$$\mathbf{E_{laser}} = E_{0,+}\mathbf{e}_+ \cos(k_\mathrm{L}x - \omega_+ t) + E_{0,-}\mathbf{e}_- \cos(-k_\mathrm{L}x - \omega_- t), \tag{5.6}$$

where $E_{0,\pm}$ denotes the field amplitudes of the σ^+, σ^- polarized optical beams, and $\mathbf{e}_\pm$ are the corresponding unit polarization vectors. It is assumed for the remainder of this thesis that $E_{0,+} = E_{0,-}$.

In the following, $|g_\alpha, \mathbf{p}\rangle$ denotes an atom in the internal state g_α and with momentum $\mathbf{p}$. After utilizing the rotating wave approximation and adiabatically eliminating the upper states, which is possible due to a large detuning Δ from the excited states, the effective Hamiltonian for a single atom confined to the x-y plane is yielded, here written in the basis of the coupled levels $|g_{-1}, \hbar(\mathbf{k} + \mathbf{k}_\mathrm{L})\rangle$ and $|g_{+1}, \hbar(\mathbf{k} - \mathbf{k}_\mathrm{L})\rangle$ as

$$\hat{H} = \begin{pmatrix} \hbar^2(k_x - k_\mathrm{L})^2/2m + \hbar\delta(y)/2 & \hbar\Omega_\mathrm{R}/2 \\ \hbar\Omega_\mathrm{R}/2 & \hbar^2(k_x + k_\mathrm{L})^2/2m - \hbar\delta(y)/2 \end{pmatrix} + \frac{\hbar^2 k_y^2}{2m}, \tag{5.7}$$

where Ω_R denotes the effective Rabi frequency of the two-photon Raman transition. For an uncoupled system (i.e. for $\Omega_\mathrm{R} = 0$) the variation of the eigenstates is shown in Fig. 5.2(a), for which the usual parabolic dispersion centered at $-k_\mathrm{L}$ and k_L for states $|g_{-1}\rangle$ and $|g_{+1}\rangle$ respectively is obtained. Here the atoms behave as free particles along $\mathbf{e}_x$. If a non-vanishing

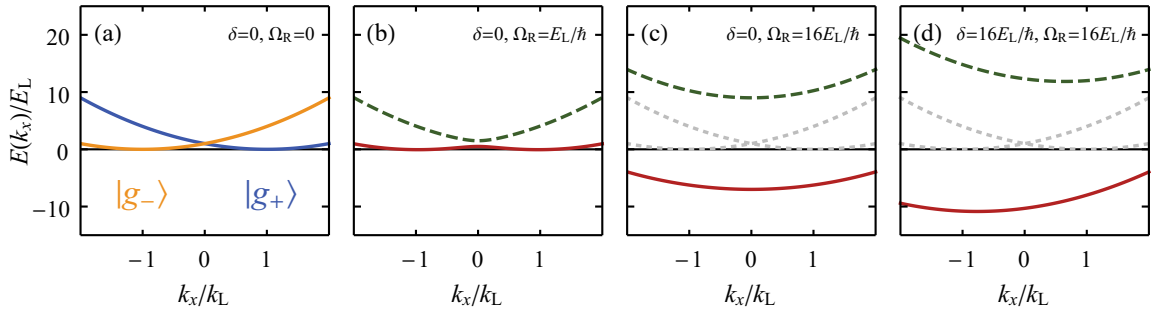

Fig. 5.2: Energy quasimomentum dispersion relation in a three-level configuration. (a) Dispersion relation for the undressed case ($\Omega_\mathrm{R} = 0$), (b) a weakly dressed case ($\Omega_\mathrm{R} = E_\mathrm{L}/\hbar$), and (c) a strongly dressed case ($\Omega_\mathrm{R} = 16E_\mathrm{L}/\hbar$), all for a vanishing two-photon detuning δ. (d) Here the dispersion relation with the same strong dressing as in (c) is shown, but for a non-vanishing two-photon detuning $\delta = 16E_\mathrm{L}/\hbar$, leading to a shift of $k_{x,\mathrm{min}}$ in k-space. The energy curves for the undressed case are plotted in (c) and (d) as gray dotted lines for comparison.

Raman coupling ($\Omega_\mathrm{R} = 16E_\mathrm{L}/\hbar$, where $E_\mathrm{L} = \hbar^2 k_\mathrm{L}^2/2m$ denotes the recoil energy), is chosen, a dressing of the energy levels is induced, leading to the dispersion relation seen in Fig. 5.2(c). Generally for a dressing of $\Omega_\mathrm{R} \gtrsim 4E_\mathrm{L}/\hbar$ the two resulting energy curves have a combined single minimum, which for $\delta = 0$ appears at $k_x = 0$, but can be shifted from that position in k-space by a non-vanishing value of δ, see Fig. 5.2(d). For $\Omega_\mathrm{R} \lesssim 4E_\mathrm{L}/\hbar$ the lowest energy curve exhibits two minima, as shown in Fig. 5.2(b).

We are now interested in the lower of the two dressed energy levels, with the dispersion shown as a solid red line in Fig. 5.2(b)-(d). Here the position of the minimum $k_{x,\mathrm{min}}$ depends on the value of the Raman detuning δ, see e.g. Fig. 5.2(d). In the presence of the gradient of the real magnetic field, $\partial B_x/\partial y$, this Raman detuning depends in turn on the transverse position y (cf. Fig. 5.3(a)). The effective Hamiltonian for the lower dressed state can thus be approximated as

$$\hat{H}_\mathrm{eff} \approx E_0 + \frac{\hbar^2(k_x - k_{\mathrm{x,min}}(y))^2}{2m^*} + \frac{\hbar^2 k_y^2}{2m} \tag{5.8a}$$

$$= E_0 + \frac{\hbar^2}{2m^*}\left(k_x - \frac{q^* A_x^*(y)}{\hbar}\right)^2 + \frac{\hbar^2 k_y^2}{2m}, \tag{5.8b}$$

where $k_{\mathrm{x,min}}(y)$ denotes the wavevector at which the described minimum of the dispersion curve occurs. In Eq. 5.8b the replacement $k_{\mathrm{x,min}}(y) = q^* A_x^*(y)/\hbar$ was used, where A_x^* is the synthetic vector potential discussed above and q^* is a synthetic charge, which will be chosen by convenience. It should be noted that both the effective mass m^* and $k_{x,\mathrm{min}}$ (correspondingly also the synthetic vector potential A_x^* and the synthetic magnetic field B_z^*, the latter as introduced in Eq. 5.10 below) depend on the used value of the effective Rabi frequency Ω_R. To subsume, an energy momentum dispersion relation $E(k_x) \approx (\hbar k_x - q^* A_x^*)^2/2m^*$ was constructed, which importantly is experimentally tunable via δ and Ω_R by changing the real magnetic field $B_x(y)$ and the laser beam intensity $I \sim |E_{0,\pm}|^2$ respectively.

5.2.2 Vector potential and synthetic gauge field

If the normalized synthetic vector potential $q^* A_x^*/\hbar k_\mathrm{L} = k_{x,\mathrm{min}}/k_\mathrm{L}$ is now plotted against the normalized detuning $\hbar\delta/E_\mathrm{L}$ for a Rabi frequency of $\Omega_\mathrm{R} = 16E_\mathrm{L}/\hbar$, the curve shown in Fig. 5.3(a) is obtained, giving the exact dependence for the corresponding parameters. Here the synthetic vector potential possesses point symmetry around $A_x^*(\delta = 0) = 0$, whereat $q^* A_x^*/\hbar$ is confined within $+k_\mathrm{L}$ and $-k_\mathrm{L}$. Near $y = 0$, for which $\delta \approx 0$, A_x^* varies linearly with the two-photon detuning δ, and correspondingly the transverse position y.

Then, given the transverse detuning variation from the gradient of the (real) magnetic field along $\mathbf{e}_y$, it is expected to obtain a non-vanishing value of the synthesized magnetic field along $\mathbf{e}_z$:

$$\mathbf{B}^* = -\nabla \times \mathbf{A}^* = \left(0, 0, -\frac{\partial A_x^*}{\partial y}\right), \tag{5.9}$$

where the component in z-direction is $B_z^* = -\partial A_x^*(y)/\partial y = -\hbar/q^* \partial k_{\mathrm{x,min}}(y)/\partial y$. With $\delta' = \partial\delta/\partial y = \Delta m_\mathrm{F} g \mu_\mathrm{B} \partial B_x/\partial y$ as the detuning gradient, one arrives at

$$B_z^* = -\frac{\hbar\delta'}{q^*}\frac{\partial k_{x,\mathrm{min}}(y)}{\partial\delta}. \tag{5.10}$$

The spatial variation of the generated synthetic magnetic field along $\mathbf{e}_y$, with a maximum at $y = \delta(y) = 0$, is shown in Fig. 5.3(b), where it was assumed to have $q^* = e$ and $\delta'/(2\pi) = 2.66\,\mathrm{kHz}/\mu\mathrm{m}$, as obtained e.g. with $g = 1$ and a gradient of the real magnetic field of $9.5\,\mathrm{G/cm}$. The magnitude of the synthetic field in the center can for $\Omega_\mathrm{R} \gg E_\mathrm{L}/\hbar$ be estimated when noting that in the limit of a detuning $\delta \gtrsim \Omega_\mathrm{R}$ ($\delta \lesssim -\Omega_\mathrm{R}$) one has $k_{x,\mathrm{min}} = -k_\mathrm{L}(+k_\mathrm{L})$ respectively (cf Fig. 5.2(d)), so that one expects a slope near $\delta = 0$ of order $\partial k_{x,\mathrm{min}}/\partial\delta \approx -k_\mathrm{L}/\Omega_\mathrm{R}$, from which $B_z^*(y = 0) \approx \hbar k_\mathrm{L}\delta'/q^*\Omega_\mathrm{R}$ is found. If a Taylor expansion up to lowest order in δ (for $\Omega_\mathrm{R} \gg E_\mathrm{L}/\hbar$) is employed for the analytically derived expression of the position of the minimum $k_{x,\mathrm{min}}$, the same results are obtained, which is plotted as the orange dashed line in Fig. 5.3(a), showing the based on this expansion derived value of the synthetic vector potential versus the detuning.

Experimental parameters for the magnetic field gradient, as well as the obtained magnitude and spatial variation of the synthetic magnetic field are comparable to the case of the rubidium experiment of [47]. The here introduced different transferred momentum of the Raman transitions with counter-propagating laser beams only account for changes of order below a factor of 2. The inhomogeneity of the effective magnetic field B_z^*, as shown in Fig. 5.3(b), is an evident disadvantage of the three-level scheme.

5.3 Synthetic magnetic fields for erbium atoms

The following discussion explores the possibility of generating synthetic magnetic fields for atomic erbium, using the transitions $4f^{12}6s^2(^3\mathrm{H}_6) \rightarrow 4f^{11}(^4\mathrm{I}^0_{15/2})5d_{5/2}6s^2(15/2, 5/2)^0_{J'}$, with $J' = 5, 6$ and 7 at transition wavelengths of $\lambda = 877\,\mathrm{nm}$, $\lambda = 847\,\mathrm{nm}$, and $\lambda = 841\,\mathrm{nm}$ respectively. These transitions excite an electron within the incompletely filled submerged f-shell

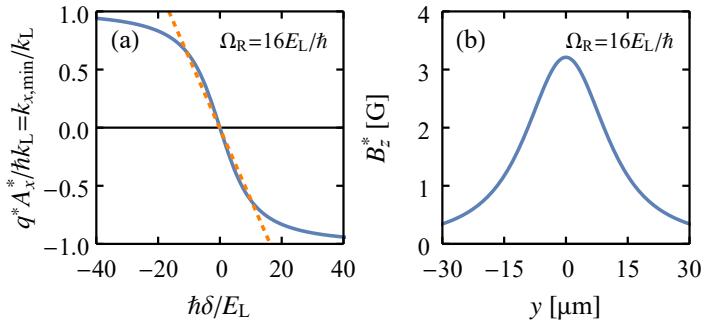

Fig. 5.3: Synthetization of magnetic fields in a three-level configuration. (a) Generated vector potential $q^*A_x^*(\delta)/\hbar$ versus the two-photon detuning δ for $\Omega_R = 16E_L/\hbar$ (blue solid line) and the dependence obtained from a Taylor expansion up to lowest order in δ ($k_{x,\mathrm{min}}^{\mathrm{Taylor}}/k_L = -\delta/\Omega_R$), yielding a linear slope (orange dotted line). (b) The generated synthetic magnetic field in the case of applying a transverse detuning gradient $\delta'/(2\pi) = 2.66\,\mathrm{kHz}/\mu\mathrm{m}$ with a gradient of the real magnetic field vs position y. Here $q^* = e$ was assumed.

of the atom, and all have a relatively small natural linewidth, e.g. $\Gamma/2\pi = 8.0\,\mathrm{kHz}$ for the $J = 6 \to J' = 7$ transition near $\lambda = 841\,\mathrm{nm}$ wavelength [77], which is also assumed for the remaining transitions.

As the energetic distance to neighbouring levels in terms of the linewidths is comparatively large, the systems are very attractive for Raman manipulation with far-detuned optical beams. Eventually, it is expected that the atomic lifetime will be limited by off-resonant scattering from e.g. the strong blue cooling transition near 401 nm (with linewidth $\Gamma_{\mathrm{blue}}/2\pi \approx 28\,\mathrm{MHz}$), which is detuned by an amount of order of the optical frequency. This defines a limit on the usable detuning from the upper state from the narrow-line transition of order $\Delta/\Gamma \simeq 10^7$, and within this limit it is assumed in the following that off-resonant contributions from other excited states are negligible. Regardless of the small scattering rate for radiation correspondingly tuned in the vicinity of such an inner-shell transition, scalar, vector, and tensor polarizabilities become comparable [75].

5.3.1 Hamiltonian and dispersion relation

From now on a nuclear spin of $I = 0$ is assumed, as is the case for all stable bosonic erbium isotopes (e.g. ^{168}Er), so that $F = J$. As the $^3\mathrm{H}_6$ ground state of atomic erbium possesses a total angular momentum of $J = 6$ (with $L = 5, S = 1$), 13 m_F-sublevels exist. The here proposed Raman coupling scheme uses a $\sigma^+ - \sigma^-$ configuration, coupling only states with $\Delta m_F = \pm 2$, so that 7 ground state sublevels $|g_\alpha\rangle$, with $m_F = \alpha$ and $\alpha = -6, -4, ..., 6$, are coupled by the Raman beams, which is shown in Fig. 5.4 for the coupling scheme of the $J = 6 \to J' = 7$ transition. The coupling scheme is chosen symmetric, which is believed to later generate an axially symmetric synthetic magnetic field. The laser electric field, with a σ^+ and a σ^- circularly polarized beam respectively, is, as in the three-level case, set to

$$\mathbf{E_{laser}} = E_{0,+}\mathbf{e}_+ \cos(k_L x - \omega_+ t) + E_{0,-}\mathbf{e}_- \cos(-k_L x - \omega_- t). \tag{5.11}$$

The relative strength of the coupling between a certain ground state sublevel $|g_\alpha\rangle$ component

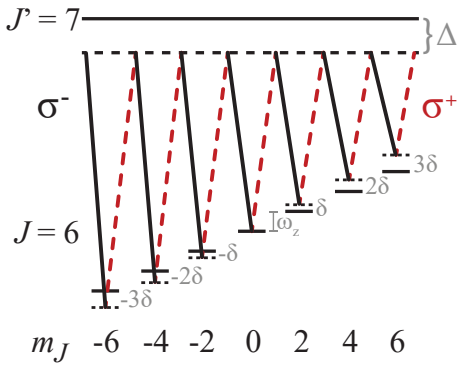

Fig. 5.4: Relevant atomic erbium levels for the $J = 6 \rightarrow J' = 7$ transition driven by Raman beams in a $\sigma^+ - \sigma^-$ optical polarization configuration. The Raman beams are irradiated in a counter-propagating geometry.

and an excited state component $|e_n\rangle$ with $\alpha = n \pm 1$ is characterized by the corresponding Clebsch-Gordan coefficient $c_{\alpha,n}$.[1] The laser coupling between levels can be written in the form

$$\Omega_{\pm} c_{\alpha,\alpha\pm1} = \frac{\langle e_{\alpha\pm1}|\mathbf{e}_{\pm}\mathbf{d}|g_{\alpha}\rangle E_{0,\pm}}{\hbar}, \tag{5.12}$$

where $\mathbf{d}$ denotes the dipole operator, and Ω_+,Ω_- the Rabi frequencies for the σ^+,σ^- polarized waves, respectively, for a transition with a Clebsch-Gordan coefficient of unity. The upper states can again be adiabatically eliminated for a large detuning Δ from the excited levels, resulting in an effective interaction Hamiltonian for the coupling to the laser fields

$$\begin{aligned}\hat{H}'_{\text{eff}} = \frac{p^2}{2m} &+ \sum_{\substack{\alpha=-6 \\ \alpha/2\in\mathbb{Z}}}^{6} \hbar\left[\omega_{\text{AC},\alpha} - \frac{\alpha}{2}\delta\right]|g_{\alpha}\rangle\langle g_{\alpha}| \\ &+ \sum_{\substack{\alpha=-6 \\ \alpha/2\in\mathbb{Z}}}^{4} \frac{\hbar\tilde{\Omega}_{\text{R},\alpha,\alpha+2}}{2}|g_{\alpha}\rangle\langle g_{\alpha+2}|\mathrm{e}^{-i2k_{\text{L}}x} \\ &+ \sum_{\substack{\alpha=-4 \\ \alpha/2\in\mathbb{Z}}}^{6} \frac{\hbar\tilde{\Omega}_{\text{R},\alpha,\alpha-2}}{2}|g_{\alpha}\rangle\langle g_{\alpha-2}|\mathrm{e}^{i2k_{\text{L}}x},\end{aligned} \tag{5.13}$$

where

$$\tilde{\Omega}_{\text{R},\alpha,\alpha\pm2} = \frac{c_{\alpha,\alpha\pm1}c_{\alpha\pm2,\alpha\pm1}\Omega_{\pm}\Omega_{\mp}}{2\Delta} \tag{5.14}$$

denotes effective two-photon Rabi frequencies between ground state sublevels and

[1] A list of relevant Clebsch-Gordan coefficients for the three erbium transitions mentioned above can be found in the appendix.

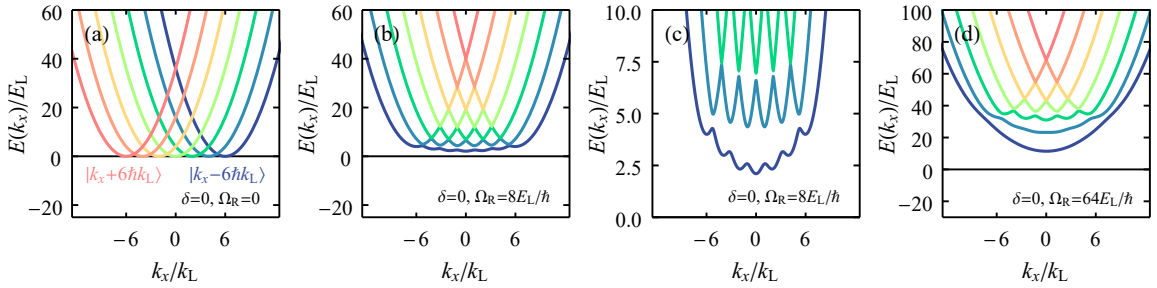

Fig. 5.5: Energy quasimomentum dispersion relation for the multi-level erbium case. (a) Dispersion relation $E(k_x)$ of the seven undressed (with $\Omega_R = 0$) states for $\delta = 0$. (b) Dispersion of the dressed state system with moderate Raman coupling ($\Omega_R = 8E_L/\hbar$, for which $\Omega_R < m_{F,\max}^2 E_L/\hbar$) and $\delta = 0$. (c) Zoom into the lower energy regions of (b) to reveal the well structure of the lowest energy band. (d) Dispersion for a larger value of the Raman coupling ($\Omega_R = 64E_L/\hbar$, for which $\Omega_R > m_{F,\max}^2 E_L/\hbar$, with $m_{F,\max} = 6$), for which the lowest energetic dressed state level has a near parabolic shape, again here for $\delta = 0$.

$$\omega_{AC,\alpha} = \frac{c_{\alpha,\alpha+1}^2 \Omega_+^2 + c_{\alpha,\alpha-1}^2 \Omega_-^2}{2\Delta} \tag{5.15}$$

is the ac Stark shift of the ground state sublevels. Any excited-state shifts δ_n can be neglected, as here a large detuning Δ was chosen. In the basis of eigenstates $|g_\alpha, \mathbf{p} + \alpha\hbar\mathbf{k}_L\rangle$ with $\alpha = -6, -4, ..., 6$, where $\mathbf{p} = \hbar\mathbf{k}$, Eq. 5.13 can be written more explicitely using the matrix form

$$\hat{H}_{\text{eff}} = \begin{pmatrix} H_{-6,-6} & \tilde{\Omega}_{-6,-4} & 0 & 0 & 0 & 0 & 0 \\ \tilde{\Omega}_{-4,-6} & H_{-4,-4} & \tilde{\Omega}_{-4,-2} & 0 & 0 & 0 & 0 \\ 0 & \tilde{\Omega}_{-2,-4} & H_{-2,-2} & \tilde{\Omega}_{-2,0} & 0 & 0 & 0 \\ 0 & 0 & \tilde{\Omega}_{0,-2} & H_{0,0} & \tilde{\Omega}_{0,2} & 0 & 0 \\ 0 & 0 & 0 & \tilde{\Omega}_{2,0} & H_{2,2} & \tilde{\Omega}_{2,4} & 0 \\ 0 & 0 & 0 & 0 & \tilde{\Omega}_{4,2} & H_{4,4} & \tilde{\Omega}_{4,6} \\ 0 & 0 & 0 & 0 & 0 & \tilde{\Omega}_{6,4} & H_{6,6} \end{pmatrix}, \tag{5.16}$$

where $H_{\alpha,\alpha} = \hbar(\omega_{AC,\alpha} - \alpha\delta/2) + \hbar^2((k_x + \alpha k_L)^2 + k_y^2)/2m$ and $\tilde{\Omega}_{\alpha,\alpha\pm2} = \hbar\tilde{\Omega}_{R,\alpha,\alpha\pm2}/2$. To find the eigenenergies of the multi-level system, the eigensystem 5.16 was solved numerically.

Fig. 5.5(a) shows the seven energy dispersion curves for $\delta = 0$ of the uncoupled system ($\Omega_R = 0$), and Figs. 5.5(b)-(d) for different values of $\Omega_R = 8E_L/\hbar$ and $64E_L/\hbar$ respectively, where $\Omega_R = \Omega_\pm\Omega_\mp/(2\Delta)$ denotes the effective two-photon Rabi frequency for Clebsch-Gordan coefficients of unity.

As in future experiments the atoms are planned to be adiabatically loaded from a BEC into the ground state of the dressed system, we are here only interested in the dispersion of the lowest energetic eigenstate. Whereas for lower values of the two-photon Rabi coupling, as seen

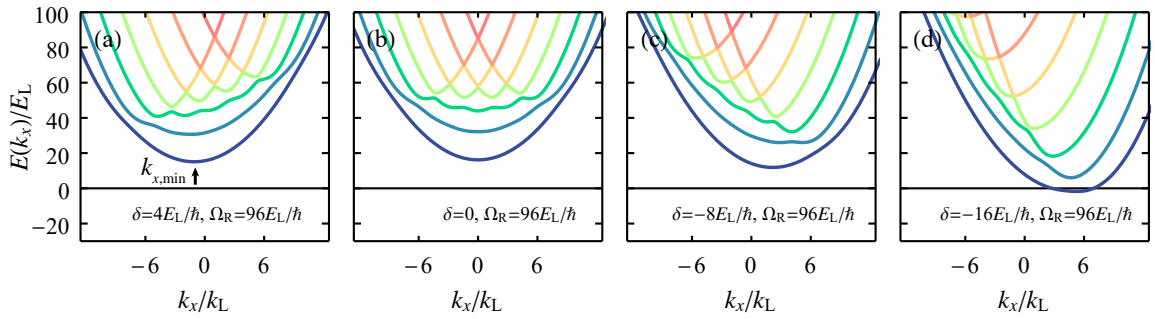

Fig. 5.6: Dependence of the dispersion relation on the two-photon detuning δ. (a) Dispersion for a large value of the Raman coupling ($\Omega_R = 96E_L/\hbar$, for which $\Omega_R > m_{F,max}^2 E_L/\hbar$, with $m_{F,max} = 6$). Here a non-vanishing two-photon detuning $\delta = 4E_L/\hbar$ was used, resulting in a minimum of the dispersion curve at $k_{x,min} \neq 0$. (b) Dispersion for the same Ω_R with $\delta = 0$, showing symmetry around $k_x = 0$. (c),(d) Dispersion for the same Ω_R, but with increasing negative detuning $\delta = -8E_L/\hbar$ and $-16E_L/\hbar$ respectively, showing $k_{x,min}$ shifting towards $k_x/k_L = m_{F,max}$ (for increasing positive detuning δ, $k_{x,min}$ shifts towards $-m_{F,max}$ correspondingly).

in Fig. 5.5(b) and especially (c), that curve has seven minima (corresponding to the seven ground state sublevels), the plot shown in Fig. 5.5(d) with $\Omega_R = 64E_L/\hbar$ depicts a smooth, near parabolic dispersion of the lowest energy dressed state. In general, for the $J = 6 \rightarrow J' = 7$ transition it appears that for Rabi frequencies $\hbar\Omega_R \gtrsim (m_{F,max}\hbar k_L)^2/(2m) = m_{F,max}^2 E_L$, with $m_{F,max} = 6$, corresponding to the recoil energy associated with the momentum difference between atoms in an outermost and a central Zeeman sublevel, the dispersion can be approximated as $E(\delta) = E_0 + \hbar(k_x - k_{x,min}(\delta))^2/(2m^*)$ for small enough values of the detuning δ. Using $A_x^*(\delta) = \hbar k_{x,min}(\delta)/q^*$, where in the presence of the transverse gradient of the real magnetic field $\delta = \delta(y)$ holds, it becomes apparent that one can describe the atomic dynamics also in the multi-level case by an effective Hamiltonian of the form of Eq. 5.8b. Additionally, a scalar potential emerges, leading to a negligible, spatially almost homogeneous energy offset, which can be seen in all dispersion relation panels with $\Omega_R \neq 0$ as the curve minimas move away from $E(k_x)/E_L = 0$. The dependence of the dispersion relation on the two-photon detuning δ is depicted in Fig. 5.6, showing a shift of $k_{x,min}$ towards $k_x/k_L = \pm m_{F,max}$ for increasing positive or negative δ respectively.

5.3.2 Vector potential and synthetic gauge field

The generated synthetic vector potential can be plotted versus the detuning δ, here shown in Fig. 5.7(a), which varies smoothly between $-6\hbar k_L/q^*$ and $6\hbar k_L/q^*$ for high values $\gtrsim m_{F,max}^2 E_L/\hbar$ of the effective Rabi frequency Ω_R. For too low Ω_R this variation of the synthetic vector potential becomes first bumpy, then even discontinuous as $k_{x,min}$ starts hopping from one distinct sublevel well of the dispersion relation to the next (as seen in Fig. 5.5(c)). With Eq. 5.10, again the synthetic magnetic field can be directly calculated from $k_{x,min}(y)$, leading to the blue solid curve shown in Fig. 5.7(b), for a detuning gradient of $\delta'/(2\pi) = 21\,\mathrm{kHz}/\mu\mathrm{m}$, as obtained with a gradient of the real magnetic field of 70.3 G/cm for the erbium case with $g = 1.166$. The synthetic magnetic field is spatially very uniform over a relatively large distance ($\sim 10\,\mu$m), with additional peaks at the edge. For smaller values of the two-photon Rabi frequency Ω_R the synthetic magnetic field loses spatial homogeneity, and for values below the

multi-photon recoil even becomes spikey, as shown in Fig. 5.7(c)), again as understood from the multiple minima of the dispersion curve in this parameter range.

To reach a ratio of $\hbar\omega_c/E_L = 1$ (with $E_L/(2\pi\hbar) \simeq 1.68\,\mathrm{kHz}$) in the center, where $\omega_c = eB^*/m^*$ denotes the value of the cyclotron frequency, a gradient of the real magnetic field of $\partial B_x/\partial y = 70.3\,\mathrm{G/cm}$ was used. This is expected to be a desirable parameter regime for the observation of fractional quantum Hall physics in such systems, as laid out in [161]. Then the magnetic length calculates as $\ell_{mag} = \sqrt{\hbar/m\omega_c} \approx 0.19\,\mu\mathrm{m}$, which yields an area per flux quantum in the order of $\mathcal{A} \sim 2\pi\ell_{mag}^2$, translating to an atomic area density of $n_a \simeq 1/(4\pi\ell_{mag}^2) \approx 2\,\mu\mathrm{m}^{-2}$ at half filling. The area of spatial homogeneity of around $10\,\mu\mathrm{m}$ diameter, as depicted in Fig. 5.7(b), should in a circular 2D geometry be sufficient to load up to about 200 atoms into a Laughlin state. In Fig. 5.7(b) for comparison the spatial variation of the synthetic magnetic field for the case of an idealized three-level system, as defined in Fig. 5.1(b), is shown (red dashed line), with parameters chosen as to also obtain $\hbar\omega_c = E_L$ at $y = 0$. It should be noted that typical area densities of cold atom systems differ from values used in electron fractional quantum Hall systems [162], so that also required (synthetic or real respectively) magnetic field strengths differ.

For a detuning $\Delta/(2\pi) \simeq 80\,\mathrm{GHz}$ from the $J = 6 \to J' = 7$ atomic erbium transition, one arrives at a ratio $\Delta/\Gamma = 10^7$. The required Raman beam intensity of $\sim 14.6\,\mathrm{W/mm^2}$, corresponding to e.g. $\simeq 115\,\mathrm{mW}$ beam power on a $100\,\mu\mathrm{m}$ beam diameter, as well as the specified value of the magnetic field gradient are experimentally well achievable. For the quoted parameters one e.g. obtains $\tilde{\Omega}_{R,0,\pm2} = c_{0,\pm1}c_{\pm2,\pm1}\Omega_R = \sqrt{2/13}\cdot 3\sqrt{5/96}\cdot 96E_L/\hbar \simeq 26E_L/\hbar$, which is roughly about a factor 2 above the value investigated for rubidium in [47]. The Clebsch-Gordan coefficients for the $\sigma^+ - \sigma^-$ polarization configuration considered here are more favorable than for the $\sigma^+ - \pi$ case investigated in the rubidium works, so that the ratio of Rabi coupling and spontaneous scattering at comparable detuning for the erbium and rubidium cases is expected to be roughly comparable. As mentioned earlier, the lanthanide case is expected to allow for larger values of Δ/Γ, leading to a reduced influence of spontaneous scattering. Since for a smooth variation of the low energy dispersion curve with a single minimum, Ω_R should be above $\sim m_{F,max}^2 E_L/\hbar$, from the point of a low spontaneous scattering, rare earth atoms with not too high values of $m_{F,max}$ seem advantageous. The latter, however, limits the magnitude of the obtainable synthetic magnetic flux.

In addition, rare-earth atoms with a comparatively small value of $m_{F,max}$ have a reduced magnetic dipole-dipole interaction. This phenomenon is already relevant when comparing the erbium (^{168}Er) and dysprosium (^{164}Dy) cases, with ratios of the dipole-dipole interaction and s-wave interaction, assuming the background scattering length, of $\epsilon_{dd,^{168}Er} \simeq 0.4$ and $\epsilon_{dd,^{164}Dy} \simeq 1.45$ respectively. However dipolar physics still remains important also for the erbium case [163].

The magnitude of the synthetic field can also for the multi-level case be varied by choice of a suitable detuning gradient δ'. Corresponding to the three-level case, for the here considered erbium transition one obtains $k_{x,min} = -m_{F,max}k_L$ ($m_{F,max}k_L$) respectively, assuming $\Omega_R > m_{F,max}^2 E_L/\hbar$ in the large detuning limit of $m_{F,max}\delta \gtrsim \Omega_R$ ($m_{F,max}\delta \lesssim -\Omega_R$), as indicated in Fig. 5.6(d). The synthetic field in the central spatial region (around $y = 0$) will be of order $B_z^* \sim \hbar k_L m_{F,max}^2 \delta'/(\Omega_R q^*)$ for the here relevant case of $\Omega_R > m_{F,max}^2 E_L/\hbar$. The

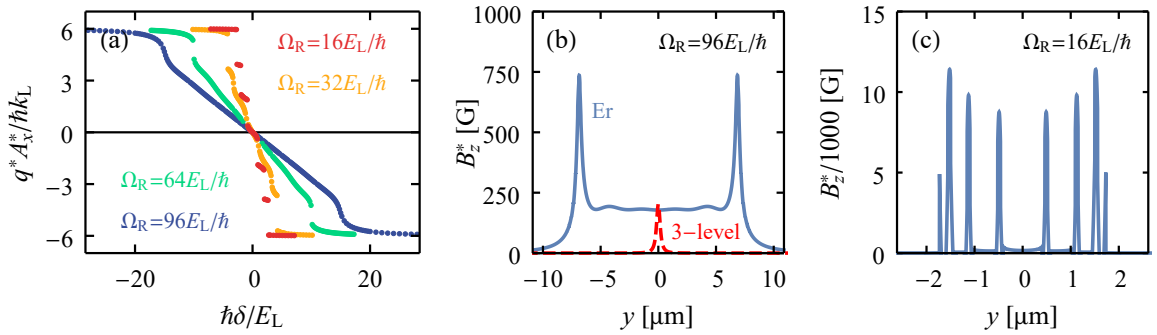

Fig. 5.7: Synthetization of magnetic fields for the multi-level erbium case. (a) Variation of the synthetic vector potential A_x^* versus the two-photon detuning δ for different values of the effective two-photon Rabi frequency Ω_R. For smaller values of Ω_R (roughly below $m_{F,\max}^2 E_L/\hbar$, with $m_{F,\max} = 6$), no continuous variation is observed. Level scheme as in Fig. 5.4. (b) Corresponding synthetic magnetic field (blue solid line) versus position along the y-axis for a transverse gradient of the real magnetic field of $\partial B_x/\partial y = 70.3\,\mathrm{G/cm}$. For $\Omega_R = 96E_L/\hbar$ a over a relatively large spatial region good spatial homogeneity is reached. For comparison, also the spatial variation of the synthetic magnetic field obtained for a pure three-level system as shown in Fig. 5.1(b) is depicted here (red dashed line), where a two-photon Rabi frequency $\Omega_R = 16E_L/\hbar$, $g = 1$, and a magnetic field gradient of 595 G/cm was assumed, for which the desired value of $\hbar\omega_c = E_L$ in the center (at $y = 0$) is achieved. (c) Whereas the synthetic magnetic field is homogeneous in the center region for large values of Ω_R, it becomes spikey for the case of small values of e.g. $\Omega_R = 16E_L/\hbar < m_{F,\max}^2 E_L/\hbar$. Additionally the extend of the synthetic field in real space reduces for smaller Ω_R, if the condition $\hbar\omega_c = E_L$ is kept unchanged.

synthetic field is dependent on the effective Rabi frequency Ω_R, which is understood from the influence of the coupling on the dressed system dispersion relation, as depicted in Fig. 5.5. Since the dispersion curve requires a smooth progression, Ω_R is not truly a free parameter, but preferably has to be choosen as a few times $m_{F,\max}^2 E_L/\hbar$. Accordingly, the dependence of the synthetic field on the maximum Zeeman quantum number $m_{F,\max}$ effectively cancels, in view of the for large values of $m_{F,\max}$ required increased Rabi coupling. However, for large values of $m_{F,\max}$ the possible maximum momentum transfer $m_{F,\max}\hbar k_L$ increases, which leads to a larger spatial area over which the synthetic magnetic field is imprinted, and correspondingly to a higher synthetic flux.

Besides the above considered transition, two other, namely the $J = 6 \to J' = 5$ and $J' = 6$ components of the $4f^{12}6s^2(^3\mathrm{H}_6) \to 4f^{11}(^4\mathrm{I}^0_{15/2})5d_{5/2}6s^2(15/2, 5/2)^0_{J'}$ erbium transition, were investigated regarding their use for synthetic magnetic fields. A comparison can be found in the top panel of Fig. 5.8, where dispersion curves for the $J = 6 \to J' = 5, 6, 7$ transitions are given for $\delta = 4E_L/\hbar$ and $\Omega_R = 96E_L/\hbar$. The middle and lower panels depict the detuning dependence of the synthetic vector potential and the spatial variation of the synthetic magnetic field respectively. For the $J = 6 \to J' = 5$ component it is also expected to reach a spatially quite uniform synthetic magnetic field and obtain $\hbar\omega_c = E_L$ in the center, with comparable parameters for the transverse magnetic field gradient. However for the $J = 6 \to J' = 6$ case the synthetic field essentially reduces to a single divergent spike in the center, which is understood from the less favorable variation of Clebsch-Gordan coefficients with the Zeeman quantum number, with relatively small couplings near the center of the Zeeman diagram ($|m_F| \approx 0$). Therefore, the lowest energetic dispersion curve has two, rather than a single

	$J' = 5$			$J' = 7$		
$\Omega_\mathrm{R}/E_\mathrm{L}$	$\delta'/2\pi$	$\partial B_x/\partial y$	I	$\delta'/2\pi$	$\partial B_x/\partial y$	I
32	9.18	28.14	4.52	10.43	31.94	4.90
64	15.78	48.36	8.98	14.99	45.92	9.74
96	24.11	73.88	13.51	20.96	70.34	14.64

Tab. 5.1: Calculated experimental parameters for different Raman coupling strengths. Detuning gradient $\delta'/2\pi$ (in kHz/μm), real magnetic field gradient $\partial B_x/\partial y$ (in G/cm) and Raman beam intensity I (in W/mm^2), chosen to reach a cyclotron frequency of $\hbar\omega_\mathrm{c} = E_\mathrm{L}$, for the two feasible Raman transitions for different values of the two-photon Rabi frequency Ω_R for unity Clebsch-Gordan coefficients.

minimum. It is reckoned that the $J = 6 \rightarrow J' = 6$ component cannot be used for the purpose of generating a synthetic magnetic field suitable to construct an experimental system for reaching fractional quantum Hall physics.

Tab. 5.1 gives a comparison of the required gradients of the real magnetic field to reach a value of the cyclotron frequency of $\hbar\omega_\mathrm{c}/E_\mathrm{L} = 1$ at $y = 0$ for different values of the two-photon Rabi frequency Ω_R for both the $J = 6 \rightarrow J' = 5$ and $J = 6 \rightarrow J' = 7$ transitions. For the lower values of Ω_R, while requiring smaller Raman beam intensities and gradients of the real magnetic field, the spatial homogeneity of the synthetic gauge field reduces. It was found that for the both here considered suitable erbium transitions for sufficient spatial homogeneity, the two-photon Rabi frequency Ω_R should lie at least above $50\,E_\mathrm{L}/\hbar$.

5.4 Laughlin-Gap

There exist two physical regimes for bosonic atoms in a synthetic magnetic field. If the applied artificial field is small, the ground state remains a Bose-Einstein condensate (BEC), characterized by a macroscopically occupied single-particle wavefunction, and the artificial magnetic field can induce vortices in the condensate. However as long as the density of vortices is small compared to the density of atoms, the condensate is not destroyed. In the ground state the vortices form a regular structure closely related to the Abrikosov lattice of type-II superconductors [164]. This regime is experimentally well accessible. For much larger values of the applied artificial magnetic field, when the density of vortices approaches that of the atomic gas, the vortex lattice melts, and in the presence of interactions the ground state can become a bosonic quantum Hall liquid.

All atoms subject to the synthetic gauge field have to be in the lowest Landau level (LLL), if one wants to observe the fractional quantum Hall effect in the latter regime. In the calculations below a LLL with a filling factor of $\nu = 1/2$ is assumed, and theory results from [165] are used, in which an ensemble of atoms subject to s-wave interactions is considered. The filling factor is here defined as

$$\nu = \frac{N_\mathrm{a}}{\Phi} = \frac{hN_\mathrm{a}}{q^* B_z^*}, \tag{5.17}$$

where N_a is the number of atoms, and $\Phi = q^* B_z^*/h$ is the number of vortices or magnetic flux quanta, respectively, in the sample area. The true ground state becomes a highly correlated Laughlin state in the presence of interactions [165,166], which is particularly interesting since some of the excitations above this ground state possess anyonic character [167]. The energetic gap to the next excited state, the so-called Laughlin gap ΔE_LG, should be sufficiently large to allow for a selective loading by adiabatic mapping from e.g. an initial Bose-Einstein condensate.

It may seem preferable to use small atom numbers in view of experimental limits on the experimentally realizable flux of the gauge field. In the investigation below, it is assumed that the besides the usual s-wave interactions additional dipole-dipole interactions present for the erbium case do not introduce significant alterations to the described picture. It should be noted that in the case of longer-range interactions, such as $1/r^3$ couplings due to dipole-dipole interactions, higher order Haldane pseudopotentials increase in importance, so that the ground state may not be well characterized by a Laughlin state. For large filling fractions however, such as $\nu = 1/2$, the ground state is still a Laughlin state, as discussed for example for the case of bosons with van-der-Waals $1/r^6$ interactions in [168]. Here, a disk-shaped trapping geometry called microtrap is considered, with the confinement along the axis of the synthetic magnetic field (i.e. the z-axis) being sufficiently strong to restrict the atomic dynamics to the two transverse directions (i.e. in the x-y plane).

In the following the case of $N_\mathrm{a} = 4$ atoms per microtrap is considered. Then the Laughlin gap can be estimated to $\Delta E_\mathrm{LG} \approx 0.16 g_\mathrm{int}$, where $g_\mathrm{int} = \sqrt{32\pi}\hbar\omega_\mathrm{c} a_\mathrm{s}/\ell_z$ is the 2D interaction coefficient, a_s the s-wave scattering length and $\ell_z = \sqrt{\hbar/m\omega_z}$ the confinement length in z-direction. Here ω_z is the corresponding trapping frequency. One way to realize the disk-shaped configuration is by the dipole potential induced by a far-detuned one-dimensional standing wave with wavelength λ_trap. In this configuration one obtains $\omega_z/(2\pi) = \sqrt{2U_0/m}/\lambda_\mathrm{trap}$, where U_0 denotes the trap depth. For a trapping light wavelength $\lambda_\mathrm{trap} = 1.064\,\mu$m and a typical trap depth $U_0 = 50 E_\mathrm{L,trap}$, with $E_\mathrm{L,trap} = h^2/(2m\lambda_\mathrm{trap}^2)$, one arrives at $\ell_z \simeq 64\,$nm and $\omega_\mathrm{c}/(2\pi) = 14.8\,$kHz. To reach the quantum Hall regime with roughly $\hbar\omega_\mathrm{c} = E_\mathrm{L}$, as expected to achieve using parameters described in section 5.3.2, a Laughlin gap of $\Delta E_\mathrm{LG} \approx h \cdot 720\,$Hz is estimated for the case of a Raman beams wavelength tuned to near the $J = 6 \rightarrow J' = 7$ transition and a s-wave scattering length of $a_s = 200 a_0$ [36], where a_0 is Bohr's radius. For larger atom numbers the predicted size of the Laughlin gap slightly reduces, and in the asymptotic case ($N_\mathrm{a} \gg 1$) reaches $\Delta E_\mathrm{LG} \simeq 0.1 g_{int}$, corresponding to $\approx h \cdot 450\,$Hz for the above parameters. Accordingly for the case of the $J = 6 \rightarrow J' = 5$ transition a Laughlin gap of $\Delta E_\mathrm{LG} \approx h \cdot 600\,$Hz is obtained for $N_\mathrm{a} = 4$, and respectively $\Delta E_\mathrm{LG} \approx h \cdot 380\,$Hz in the asymptotic case with $N_\mathrm{a} \gg 1$.

Considering the calculated gap sizes, adiabatic loading from a Bose-Einstein condensate seems realistic. Moreover larger atom numbers per trap are experimentally feasible, where one benefits from the incompressibility of the Laughlin phase, pushing quasi-holes to the outer trap regions, leading to a useable configuration when applying spatially resolved detection techniques only monitoring the central trap region.

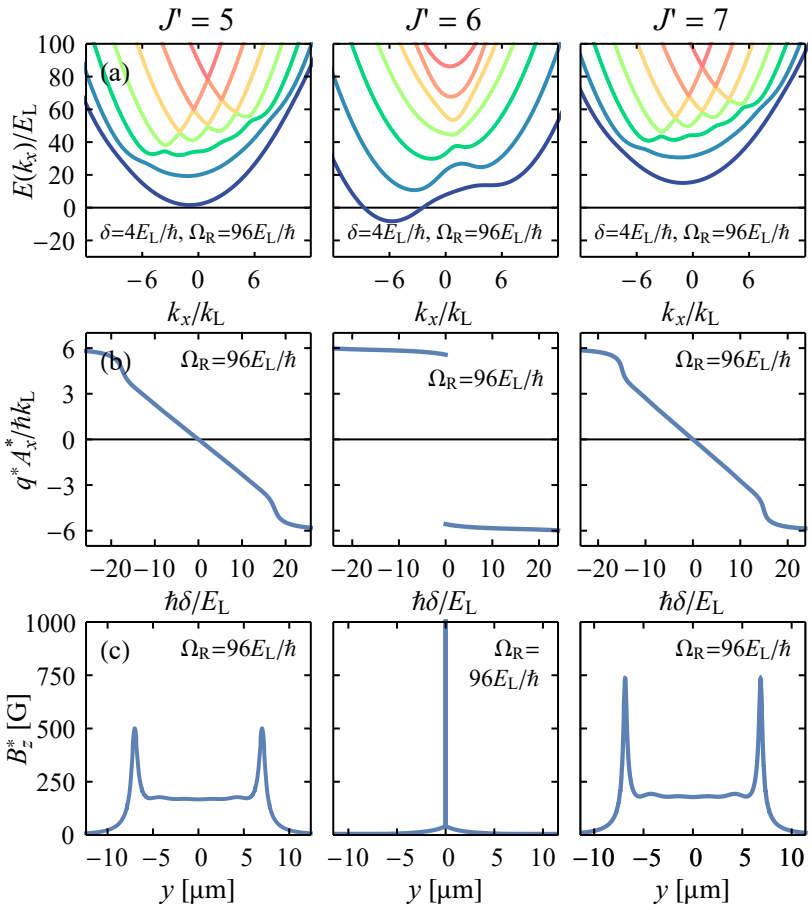

Fig. 5.8: Comparison of results for the different narrow-line transition components $J = 6 \to J' = 5, 6,$ and 7 (left, middle, and right panels respectively) of the erbium transition, where $\Omega_\mathrm{R} = 96E_\mathrm{L}/\hbar$ is assumed in all cases. (a) Energy wavevector dispersion $E(k_x)$ for a two-photon detuning $\delta = 4E_\mathrm{L}/\hbar$. (b) Synthetic vector potential A_x^* versus the two-photon detuning δ, and (c) the synthetic magnetic field versus position y for a transverse gradient of the (real) magnetic field of 73.9 G/cm in the case of $J' = 5$ and of 70.3 G/cm in the case of $J' = 7$, for which in both cases $\hbar\omega_\mathrm{c} = E_\mathrm{L}$ is reached in the center. Then for both the $J = 6 \to J' = 5$ and $J' = 7$ transitions the lowest energetic dispersion curve has only a single minimum, enabling the synthetization of a – within the central region – spatially relatively homogeneous synthetic magnetic field. In the case of the $J = 6 \to J' = 6$ transition the lowest energy dispersion curve for the same value of the Raman coupling has two minima, with the absolute minimum alternating from $k_{x,\mathrm{min}} < 0$ to $k_{x,\mathrm{min}} > 0$ for $\delta > 0$ and $\delta < 0$ respectively, so that the synthetic vector potential exhibits a step-like behaviour. The resulting expected synthetic magnetic field (shown here for a transverse gradient of the real magnetic field of 70.3 G/cm) exhibits a divergence at $y = 0$, as understood from the here discontinuous variation of the vector potential versus δ. The synthetic magnetic field in the latter case is estimated to not be usable for the purpose of constructing an experimental system capable of reaching fractional quantum Hall physics.

6 Conclusion and outlook

Quantum degenerate atomic rare earth gases are attractive systems for both studies of novel dipolar gas effects as well as for the physics of atoms in strong gauge fields. This thesis reports of an experiment where an atomic erbium Bose-Einstein condensate was generated in a hybrid crossed optical dipole trap realized with a focused mid-infrared beam near 10.6 μm wavelength generated by a CO_2 laser and a beam near 1.064 μm wavelength generated by a Nd:YAG laser. In further work of this thesis, a proposal for the generation of strong synthetic magnetic fields based on ultracold erbium atoms is given.

In the first experimental part of the thesis, ultracold erbium atoms were generated by initially decelerating an erbium atomic beam with a Zeeman slower, as to load a magneto-optical trap operated on a narrow-line transition. After spatially compressing the trapped atomic ensemble, it is loaded into an optical dipole trap potential provided by a CO_2 laser beam near 10.6 μm wavelength, which then is supplemented by an additional crossing beam stemming from a Nd:YAG laser operated near 1064 nm wavelength during evaporation. Here it was possible to increase the phase space density above the critical value of 2.612, and observe the formation of a Bose-Einstein condensate consisting of up to $3.5 \cdot 10^4$ erbium atoms, showing an improvement of more than 15 % compared to earlier iterations of the experiment with a single beam optical dipole trap setup. The BEC exhibits a condensate lifetime of up to 12 s, increased by 30 % in comparison to former single beam optical dipole trap setups. Furthermore the general long-term stability of the experimental setup was improved significantly, leading to much less maintenance efforts and downtimes of the experiment, which arguably was the main challenge of the old setup.

As an experimental outlook it should be mentioned that also other optical dipole trap configurations are tested in setups succeeding this thesis, especially a crossed optical dipole trap consisting of a CO_2 laser beam and an erbium fiber laser beam operated at 1550 nm to potentially further optimize condensate lifetimes due to lower scattering rates with the cross beam in comparison to Nd:YAG laser light. In parallel the experimental realization of synthetic magnetic fields by phase imprinting via Raman manipulation in prospect of fractional quantum Hall physics has begun at this experiment, with theoretical work carried out within the scope of this thesis to determine critical future experimental parameters.

For the latter the laser-induced synthetization of gauge fields in the atomic erbium lanthanide system with a ground state orbital angular momentum $L > 0$ was investigated here. A configuration with two counter-propagating oppositely circularly polarized Raman beams was shown to be an attractive approach for both on $J = 6 \rightarrow J' = 5$ and $J' = 7$ narrow-line atomic erbium transitions. In the presence of a transverse gradient of the real magnetic field, sufficiently strong synthetic magnetic fields with good spatial homogeneity are predicted to be possible, with estimated photon scattering rates roughly two orders of magnitude lower than in implementations with alkali atomic systems. Moreover the size of the expected Laughlin

gap arising from s-wave interactions for typical experimental parameters was estimated, showing that rare earth atomic systems are attractive candidates for experimental investigations of fractional quantum Hall physics.

For the future, it will be important to experimentally realize synthetic magnetic fields in an erbium atomic system. Attractive areas of research interest then include the investigation of vortices in such a dipolar quantum gas, as well as the generation and detection of fractional quantum Hall states. Here theoretical work describing the form of the ground state in the presence of both the synthetic magnetic field and dipolar interactions will be crucial [169,170]. A far future outlook would be the achievement of fundamental understandings of fractional quantum Hall states and their topology-induced robustness as well as their non-Abelian dynamics, possibly supporting the realization of a fault-tolerant topological quantum computer [145].

Appendix

In Tab. 6.1 the Clebsch-Gordan coefficients for the here relevant ground state sublevels of the three transitions with $J = 6 \rightarrow J' = 5, 6, 7$ respectively are listed. Here m_F denotes the ground state sublevel from which a transition to $m_{F'} = m_F + 1$ (with $\Delta m_F = +1$) or $m_F - 1$ (with $\Delta m_F = -1$) originates.

m_F	-6	-4	-2	0	2	4	6
$J = 6 \rightarrow J' = 5$							
$\Delta m_F = +1$	$\sqrt{\frac{11}{13}}$	$\sqrt{\frac{15}{26}}$	$\sqrt{\frac{14}{39}}$	$\sqrt{\frac{5}{26}}$	$\frac{1}{\sqrt{13}}$	$\frac{1}{\sqrt{78}}$	
$\Delta m_F = -1$		$\frac{1}{\sqrt{78}}$	$\frac{1}{\sqrt{13}}$	$\sqrt{\frac{5}{26}}$	$\sqrt{\frac{14}{39}}$	$\sqrt{\frac{15}{26}}$	$\sqrt{\frac{11}{13}}$
$J = 6 \rightarrow J' = 6$							
$\Delta m_F = +1$	$-\frac{1}{\sqrt{7}}$	$-\sqrt{\frac{5}{14}}$	$-\sqrt{\frac{10}{21}}$	$-\frac{1}{\sqrt{2}}$	$-\sqrt{\frac{3}{7}}$	$-\sqrt{\frac{11}{42}}$	
$\Delta m_F = -1$		$\sqrt{\frac{11}{42}}$	$\sqrt{\frac{3}{7}}$	$\frac{1}{\sqrt{2}}$	$\sqrt{\frac{10}{21}}$	$\sqrt{\frac{5}{14}}$	$\frac{1}{\sqrt{7}}$
$J = 6 \rightarrow J' = 7$							
$\Delta m_F = +1$	$\frac{1}{\sqrt{91}}$	$\sqrt{\frac{6}{91}}$	$\sqrt{\frac{15}{91}}$	$\frac{2}{\sqrt{13}}$	$3\sqrt{\frac{5}{91}}$	$\sqrt{\frac{66}{91}}$	1
$\Delta m_F = -1$	1	$\sqrt{\frac{66}{91}}$	$3\sqrt{\frac{5}{91}}$	$\frac{2}{\sqrt{13}}$	$\sqrt{\frac{15}{91}}$	$\sqrt{\frac{6}{91}}$	$\frac{1}{\sqrt{91}}$

Tab. 6.1: Relevant Clebsch-Gordan coefficients for the three transitions $J = 6 \rightarrow J' = 5, 6, 7$.

Bibliography

[1] A. Einstein, *Quantentheorie des einatomigen idealen Gases*, Sitzber. Kgl. Preuß. Akad. Wiss., 261–267 (1924).

[2] A. Einstein, *Quantentheorie des einatomigen idealen Gases. Zweite Abhandlung*, Sitzber. Kgl. Preuß. Akad. Wiss., 3–14 (1925).

[3] S. N. Bose, *Plancks Gesetz und Lichtquantenhypothese*, Z. Phys. **26**, 178–181 (1924).

[4] M. H. Anderson, J. R. Ensher, M. R. Matthews, and E. A. Wieman, C. E. und Cornell, *Observation of Bose-Einstein Condensation in a Dilute Atomic Vapor*, Science **269**, 198 (1995).

[5] K. B. Davis, M. O. Mewes, M. R. Andrews, N. J. Van Druten, D. S. Durfee, D. M. Kurn, and W. Ketterle, *Bose-Einstein Condensation in a Gas of Sodium Atoms*, Phys. Rev. Lett. **75**, 3969–3973 (1995).

[6] F. Dalfovo, S. Giorgini, L. P. Pitaevskii, and S. Stringari, *Theory of Bose-Einstein condensation in trapped gases*, Rev. Mod. Phys. **71**, 463 (1999).

[7] M. R. Andrews, *Observation of Interference Between Two Bose Condensates*, Science **275**, 637–641 (1997).

[8] M. R. Matthews, B. P. Anderson, P. C. Haljan, D. S. Hall, C. E. Wieman, and E. A. Cornell, *Vortices in a Bose-Einstein Condensate*, Phys. Rev. Lett. **83**, 2498–2501 (1999).

[9] M. Greiner, O. Mandel, T. Esslinger, T. W. Hänsch, and I. Bloch, *Quantum phase transition from a superfluid to a Mott insulator in a gas of ultracold atoms*, Nature **415**, 39–44 (2002).

[10] M. B. Dahan, E. P., J. R., Y. C., and C. Salomon, *Bloch Oscillations of Atoms in an Optical Potential*, Physical Review Letters **76**, 4508–4511 (1996).

[11] M. Leder, C. Grossert, L. Sitta, M. Genske, A. Rosch, and M. Weitz, *Real-space imaging of a topologically protected edge state with ultracold atoms in an amplitude-chirped optical lattice*, Nat. Commun. **7**, 13112 (2016).

[12] U. Fano, *Sullo spettro di assorbimento dei gas nobili presso il limite dello spettro d'arco*, Nuovo Cim. **12**, 154–161 (1935).

[13] H. Feshbach, *Unified theory of nuclear reactions*, Ann. Phys. **5**, 357–390 (1958).

[14] S. L. Cornish, N. R. Claussen, J. L. Roberts, E. A. Cornell, and C. E. Wieman, *Stable 85Rb Bose-Einstein Condensates with Widely Tunable Interactions*, Phys. Rev. Lett. **85**, 1795–1798 (2000).

[15] C. Chin, R. Grimm, P. Julienne, and E. Tiesinga, *Feshbach resonances in ultracold gases*, Rev. Mod. Phys. **82**, 1225–1286 (2010).

[16] A. Polkovnikov, K. Sengupta, A. Silva, and M. Vengalattore, *Colloquium: Nonequilibrium dynamics of closed interacting quantum systems*, Rev. Mod. Phys. **83**, 863–883 (2011).

[17] A. M. Kaufman, M. E. Tai, A. Lukin, M. Rispoli, R. Schittko, P. M. Preiss, and M. Greiner, *Quantum thermalization through entanglement in an isolated many-body system*, Science **353**, 794–800 (2016), no. 6301.

[18] I. M. M. Georgescu, S. Ashhab, and F. Nori, *Quantum simulation*, Rev Mod Phys **86**, 153–185 (2014).

[19] R. Balili, V. Hartwell, D. Snoke, L. Pfeiffer, and K. West, *Bose-Einstein Condensation of Microcavity Polaritons in a Trap*, Science **316**, 1007–1010 (2007).

[20] J. Klaers, J. Schmitt, F. Vewinger, and M. Weitz, *Bose-Einstein condensation of photons in an optical microcavity*, Nature **468**, 545–548 (2010).

[21] S. Christopoulos, G. Baldassarri, H. von Högersthal, A. J. D. Grundy, P. G. Lagoudakis, A. V. Kavokin, J. J. Baumberg, G. Christmann, R. Butté, E. Feltin, J.-F. Carlin, and N. Grandjean, *Room-Temperature Polariton Lasing in Semiconductor Microcavities*, Phys. Rev. Lett. **98**, 126405 (2007).

[22] B. DeMarco, *Onset of Fermi Degeneracy in a Trapped Atomic Gas*, Science **285**, 1703–1706 (1999).

[23] E. Fermi, *Zur Quantelung des idealen einatomigen Gases*, Z. Phys. **36**, 902–912 (1926).

[24] P. A. M. Dirac, *On the Theory of Quantum Mechanics*, Proc. R. Soc. Lond. Series A **112**, 661–677 (1926).

[25] T. Esslinger, *Fermi-Hubbard Physics with Atoms in an Optical Lattice*, Ann. Rev. Cond. Matt. Phys. **1**, 129–152 (2010).

[26] S. Stellmer, M. K. Tey, B. Huang, R. Grimm, and F. Schreck, *Bose-Einstein Condensation of Strontium*, Phys. Rev. Lett. **103**, 200401 (2009).

[27] M. Lu, N. Q. Burdick, S.-H. Youn, and B. L. Lev, *Strongly Dipolar Bose-Einstein Condensate of Dysprosium*, Phys. Rev. Lett. **107**, 190401 (2011).

[28] M. Lu, N. Q. Burdick, and B. L. Lev, *Quantum Degenerate Dipolar Fermi Gas*, Phys. Rev. Lett. **108**, 1–5 (2012).

[29] Y. Takasu, K. Maki, K. Komori, T. Takano, K. Honda, M. Kumakura, T. Yabuzaki, and Y. Takahashi, *Spin-Singlet Bose-Einstein Condensation of Two-Electron Atoms*, Phys. Rev. Lett. **91**, 040404 (2003).

[30] K. Aikawa, A. Frisch, M. Mark, S. Baier, A. Rietzler, R. Grimm, and F. Ferlaino, *Bose-Einstein Condensation of Erbium*, Phys. Rev. Lett. **108**, 210401 (2012).

[31] K. Aikawa, A. Frisch, M. Mark, S. Baier, R. Grimm, and F. Ferlaino, *Reaching Fermi Degeneracy via Universal Dipolar Scattering*, Phys. Rev. Lett. **112**, 010404 (2014).

[32] D. Sukachev, A. Sokolov, K. Chebakov, A. Akimov, S. Kanorsky, N. Kolachevsky, and V. Sorokin, *Magneto-optical trap for thulium atoms*, Phys. Rev. A **82**, 011405(R) (2010).

[33] E. Kalganova, G. Vishnyakova, A. Golovisin, D. Tregubov, D. Sukachev, S. Fedorov, K. Khabarova, A. Akimov, N. Kolachevsky, and V. Sorokin, *Laser cooling and trapping of thulium atoms for further investigation of collisional properties*, J. Phys.: Conf. Ser. **635**, 092117 (2015).

[34] J. Miao, J. Hostetter, G. Stratis, and M. Saffman, *Magneto-optical trapping of holmium atoms*, Phys. Rev. A **89**, 041401(R) (2014).

[35] A. Trautmann, P. Ilzhöfer, G. Durastante, C. Politi, M. Sohmen, M. J. Mark, and F. Ferlaino, *Dipolar Quantum Mixtures of Erbium and Dysprosium Atoms*, Phys. Rev. Lett. **121**, 213601 (2018).

[36] A. Frisch, M. Mark, K. Aikawa, F. Ferlaino, J. L. Bohn, C. Makrides, A. Petrov, and S. Kotochigova, *Quantum chaos in ultracold collisions of gas-phase erbium atoms*, Nature **507**, 475–9 (2014).

[37] K. Baumann, N. Q. Burdick, M. Lu, and B. L. Lev, *Observation of low-field Fano-Feshbach resonances in ultracold gases of dysprosium*, Phys. Rev. A **89**, 020701(R) (2014).

[38] K. Aikawa, S. Baier, A. Frisch, M. Mark, C. Ravensbergen, and F. Ferlaino, *Observation of Fermi surface deformation in a dipolar quantum gas*, Science **345**, 1484 (2014).

[39] A. Frisch, M. Mark, K. Aikawa, S. Baier, R. Grimm, A. Petrov, S. Kotochigova, G. Quéméner, M. Lepers, O. Dulieu, and F. Ferlaino, *Ultracold Dipolar Molecules Composed of Strongly Magnetic Atoms*, Phys. Rev. Lett. **115**, 203201 (2015).

[40] S. Baier, M. J. Mark, D. Petter, K. Aikawa, L. Chomaz, Z. Cai, M. Baranov, P. Zoller, and F. Ferlaino, *Extended Bose-Hubbard Models with Ultracold Magnetic Atoms*, Science **352**, 6282 (2016).

[41] N. Q. Burdick, A. G. Sykes, Y. Tang, and B. Lev, *Anisotropic collisions of dipolar Bose–Einstein condensates in the universal regime*, New. J. Phys. **18**, (2016), no. 111004.

[42] L Chomaz, S Baier, D Petter, M. J. Mark, F Wächtler, L Santos, and F Ferlaino, *Quantum-Fluctuation-Driven Crossover from a Dilute Bose-Einstein Condensate to a Macrodroplet in a Dipolar Quantum Fluid*, Physical Review X **6**, (2016), no. 4.

[43] D. Petter, A. Patschneider, G. Natale, M. J. Mark, M. A. Baranov, R. v. Bijnen, S. M. Roccuzzo, A. Recati, B. Blakie, D. Baillie, L. Chomaz, and F. Ferlaino, *High-energy Bragg scattering measurements of a dipolar supersolid*, , arXiv:2005.02213 (2016).

[44] X.-L. Qi and S.-C. Zhang, *Topological insulators and superconductors*, Rev. Mod. Phys. **83**, 1057–1110 (2011).

[45] S. Das Sarma, M. Freedman, and C. Nayak, *Topologically Protected Qubits from a Possible Non-Abelian Fractional Quantum Hall State*, Phys. Rev. Lett. **94**, 166802 (2005).

[46] Y.-J. Lin, R. L. Compton, K. Jiménez-García, J. V. Porto, and I. B. Spielman, *Synthetic magnetic fields for ultracold neutral atoms*, Nature **462**, 628–632 (2009).

[47] I. B. Spielman, *Raman processes and effective gauge potentials*, Phys. Rev. A **79**, 063613 (2009).

[48] R. Grimm, M. Weidemüller, and Y. B. Ovchinnikov, *Optical Dipole Traps for Neutral Atoms*, Adv. At. Mol. Opt. Phys. **42**, 95–170 (2000).

[49] X. Cui, B. Lian, T. L. Ho, B. L. Lev, and H. Zhai, *Synthetic gauge field with highly magnetic lanthanide atoms*, Phys. Rev. A **88**, 011601 (2013).

[50] D. Babik, R. Roell, D. Helten, M. Fleischhauer, and M. Weitz, *Synthetic magnetic fields for cold erbium atoms*, Phys. Rev. A **101**, 053603 (2020).

[51] T. Chalopin, T. Satoor, A. Evrard, V. Makhalov, J. Dalibard, R. Lopes, and S. Nascimbene, *Probing chiral edge dynamics and bulk topology of a synthetic Hall system*, Nat. Phys. (2020). https://doi.org/10.1038/s41567-020-0942-5.

[52] J. J. McClelland and J. L. Hanssen, *Laser cooling without repumping: A magneto-optical trap for erbium atoms*, Phys. Rev. Lett. **96**, 143005 (2006).

[53] H. Brammer, *Aufbau eines frequenzstabilisierten Lasersystems zur optischen Kühlung von Erbiumatomen*, Diplomarbeit, Rheinische Friedrich-Wilhelms-Universität Bonn (2010).

[54] J. Ulitzsch, *Magnetooptische Falle für Erbiumatome*, Diplomarbeit, Rheinische Friedrich-Wilhelms-Universität Bonn (2011).

[55] H. Brammer, *Ultrakalte Erbiumatome in einer CO_2-Laser Dipolfalle*, Dissertation, Rheinische Friedrich-Wilhelms-Universität Bonn (2016).

[56] J. Ulitzsch, *Erzeugung eines Bose-Einstein-Kondensats aus Erbiumatomen in einer quasi-elektrostatischen Dipolfalle*, Dissertation, Rheinische Friedrich-Wilhelms-Universität Bonn (2016).

[57] J. Ulitzsch, D. Babik, R. Roell, and M. Weitz, *Bose-einstein condensation of erbium atoms in a quasielectrostatic optical dipole trap*, Phys. Rev. A **95**, 043614 (2017).

[58] W. Pauli, *Über den Zusammenhang des Abschlusses der Elektronengruppen im Atom mit der Komplexstruktur der Spektren*, Z. Phys. **31**, 765–783 (1925).

[59] C. J. Pethick and H. Smith, *Bose-Einstein condensation in Dilute Gases*, 1. Ed., Cambridge: Cambridge University Press, 2002.

[60] C. Patrignani, *Review of particle physics*, Chin. Phys. C **40**, 100001 (2016).

[61] C. G. Mosander, *On the new metals, lanthanium and didymium, which are associated with cerium; and on erbium and terbium, new metals associated with yttria*, Philos. Mag. [3] **23**, 241–254 (1843).

[62] A. F. Holleman and N. Wiberg, *Lehrbuch der Anorganischen Chemie*, 102. Ed., Berlin: de Gruyter, 2007.

[63] J. Emsley, *Nature's building blocks - An A-Z Guide to the Elements*, 1. Ed., Oxford: Oxford University Press, 2001.

[64] J. Emsley, *The Elements*, 1. Ed., Oxford: Oxford University Press, 1989.

[65] T. Daniyarov, *Metallische magnetische Kalorimeter zum hochauflösenden Nachweis von Röntgenquanten und hochenergetischen Molekülen*, Dissertation, Ruprecht-Karls-Universität Heidelberg (2005).

[66] G. Teikemeier and D. J. Goldberg, *Skin Resurfacing with the Erbium: YAG Laser*, Dermatologic Surgery **23**, 685–687 (1997).

[67] E. Bornstein, *Proper use of Er:YAG lasers and contact sapphire tips when cutting teeth and bone: scientific principles and clinical application*, Dentistry Today **23**, 84 (2004).

[68] E. Saglamyurek, J. Jin, V. B. Verma, M. D. Shaw, F. Marsili, S. W. Nam, D. Oblak, and W. Tittel, *Quantum storage of entangled telecom-wavelength photons in an erbium-doped optical fibre*, Nature Phot. **9**, 83–87 (2015).

[69] X. Cheng, Y. Pan, Z. Yuan, X. Wang, W. Su, L. Yin, X. Xie, and L. Huang, *Er^{3+} Sensitized Photon Upconversion Nanocrystals*, Adv. Funct. Mater. **28**, 1800208 (2018).

[70] W. C. Martin, R. Zalubas, and L. Hagan, *Atomic energy levels - The rare-Earth elements*, Washington: National Bureau of Standards, U.S. Department of Commerce, 1978.

[71] A. Frisch, *Dipolar Quantum Gases of Erbium*, Dissertation, Universität Innsbruck (2014).

[72] J. Müller, B. Singh, and N. A. Surplice, *The gettering action of evaporated films of titanium and erbium*, Jour. Phys. D **5**, 6 (1972).

[73] B. G. Wybourne and L. Smentek, *Optical Spectroscopy of Lanthanides: Magnetic and Hyperfine Interactions*, Boca Raton: CRC Press, 2007.

[74] A. Kramida, Y. Ralchenko, J. Reader, and NIST ASD Team, *NIST Atomic Spectra Database (version 5.7.1)*, Gaithersburg, MD, 2019 [visited on 15.09.2020].

[75] M. Lepers, J.-F. Wyart, and O. Dulieu, *Anisotropic optical trapping of ultracold erbium atoms*, Phys. Rev. A **89**, 022505 (2014).

[76] E. Raab, M. Prentiss, A. Cable, S. Chu, and D. Pritchard, *Trapping of Neutral Sodium Atoms with Radiation Pressure*, Phys. Rev. Lett. **59**, 2631 (1987).

[77] H. Ban, M. Jacka, J. Hanssen, J. Reader, and J. McClelland, *Laser cooling transitions in atomic erbium*, Opt. Express **13**, 3185–3195 (2005).

[78] E. A. Den Hartog, J. P. Chisholm, and J. E. Lawler, *Radiative lifetimes of neutral erbium*, Jour. Phys. B **43**, 155004 (2010).

[79] J. E. Lawler, J.-F. Wyart, and E. A. Den Hartog, *Atomic transition probabilities of Er I*, Jour. Phys. B **43**, 235001 (2010).

[80] A. Frisch, K. Aikawa, M. Mark, A. Rietzler, J. Schindler, E. Zupanič, R. Grimm, and F. Ferlaino, *Narrow-line magneto-optical trap for erbium*, Phys. Rev. A **85**, 051401 (2012).

[81] J. G. Conway and B. G. Wybourne, *Low-Lying Energy Levels of Lanthanide Atoms and Intermediate Coupling*, Phys. Rev. **130**, 2325 (1963).

[82] P. Zeeman, *The Effect of Magnetisation on the Nature of Light Emitted by a Substance*, Nature **55**, 347–347 (1897).

[83] B. R. Judd and I. Lindgren, *Theory of Zeeman Effect in the Ground Multiplets of Rare-Earth Atoms*, Phys. Rev. **122**, 1802–1812 (1961).

[84] H. Metcalf and P. van der Straten, *Laser Cooling and Trapping*, New York: Springer, 1999.

[85] W. Demtröder, *Experimentalphysik 1*, Berlin: Springer, 2008.

[86] C. A. Doppler, *Ueber das farbige Licht der Doppelsterne und einiger anderer Gestirne des Himmels*, Abhandlung der Königlich Böhmischen Gesellschaft der Wissenschaften **5**, 3 (1842).

[87] S. Chu, L. Hollberg, J. E. Bjorkholm, A. Cable, and A. Ashkin, *Three-dimensional viscous confinement and cooling of atoms by resonance radiation pressure*, Phys. Rev. Lett. **55**, 48–51 (1985).

[88] J. Dalibard and C. Cohen-Tannoudji, *Laser cooling below the Doppler limit by polarization gradients: simple theoretical models*, J. Opt. Soc. Am. B **6**, 2023–2045 (1989).

[89] C. S. Adams and E. Riis, *Laser cooling and trapping of neutral atoms*, Prog. Quant. Electr. **21**, 1–79 (1997).

[90] F. Bardou, J. P. Bouchaud, O. Emile, A. Aspect, and C. Cohen-Tannoudji, *Subrecoil laser cooling and Lévy flights*, Phys. Rev. Lett. **72**, 203–206 (1994).

[91] F. M. Peixoto, *Enhanced Loading of a Lithium 7 Magneto Optical Trap using Transverse Cooling and Frequency Spread Light*, Dissertation, Yale University (2002).

[92] M. A. Joffe, W. Ketterle, A. Martin, and D. E. Pritchard, *Transverse cooling and deflection of an atomic beam inside a Zeeman slower*, J. Opt. Soc. Am. B **10**, 2257 (1993).

[93] N. Leefer, A. Cingöz, B. Gerber-Siff, A. Sharma, J. R. Torgerson, and D. Budker, *Transverse laser cooling of a thermal atomic beam of dysprosium*, Phys. Rev. A **81**, 043427 (2010).

[94] W. D. Phillips and H. Metcalf, *Laser Deceleration of an Atomic Beam*, Phys. Rev. Lett. **48**, 596–599 (1982).

[95] T. H. Loftus, T. Ido, M. M. Boyd, A. D. Ludlow, and J. Ye, *Narrow line cooling and momentum-space crystals*, Phys. Rev. A **70**, 063413 (2004).

[96] H. Katori, T. Ido, Y. Isoya, and M. Kuwata-Gonokami, *Magneto-Optical Trapping and Cooling of Strontium Atoms down to the Photon Recoil Temperature*, Phys. Rev. Lett. **82**, 1116–1119 (1999).

[97] C. V. Harnik, *A hybrid crossed optical dipole trap for Bose-Einstein condensation of atomic erbium*, Masterarbeit, Rheinische Friedrich-Wilhelms-Universität Bonn (2019).

[98] P. W. Langhoff, S. T. Epstein, and M. Karplus, *Aspects of Time-Dependent Perturbation Theory*, Rev. Mod. Phys. **44**, 602–644 (1972).

[99] J. Stark, *Beobachtungen über den Effekt des elektrischen Feldes auf Spektrallinien. I. Quereffekt*, Ann. d. Phys. **348**, 965–982 (1914).

[100] J. Stark and G. Wendt, *Beobachtungen über den Effekt des elektrischen Feldes auf Spektrallinien. II. Längseffekt*, Ann. d. Phys. **348**, 983–990 (1914).

[101] A. Mosk, S. Kraft, M. Mudrich, K. Singer, W. Wohlleben, R. Grimm, and M. Weidemüller, *Mixture of ultracold lithium and cesium atoms in an optical dipole trap*, App. Phy. B **73**, 791–799 (2001).

[102] A. N. Nikolov, E. E. Eyler, X. T. Wang, J. Li, H. Wang, W. C. Stwalley, and P. L. Gould, *Observation of Ultracold Ground-State Potassium Molecules*, Phys. Rev. Lett. **82**, 703–706 (1999).

[103] T. Takekoshi, J. R. Yeh, and R. J. Knize, *Quasi-electrostatic trap for neutral atoms*, Opt. Commun. **114**, 421–424 (1995).

[104] J. H. Becher, S. Baier, K. Aikawa, M. Lepers, J.-F. Wyart, O. Dulieu, and F. Ferlaino, *Anisotropic polarizability of erbium atoms*, Phys. Rev. A **97**, 012509 (2018).

[105] C. S. Adams, H. J. Lee, N. Davidson, M. Kasevich, and S. Chu, *Evaporative cooling in a crossed dipole trap*, Phys. Rev. Lett. **74**, 3577–3580 (1995).

[106] T. Takekoshi and R. J. Knize, *CO_2 laser trap for cesium atoms*, Opt. Lett. **21**, 77 (1996).

[107] M. Weitz, S. Friebel, R. Scheunemann, J. Walz, and T. W. Hänsch, *A CO_2 laser optical lattice with cold rubidium atoms*, in Int. Quant. Electr. Conf., P. Corkum and N. Peyghambarian (eds.), **7**, OSA Technical Digest (1998).

[108] E. Hecht, *Optics*, 4. Ed., San Francisco: Addison Wesley, 2001.

[109] S. Baier, *An optical dipole trap for Erbium with tunable geometry*, Masterthesis, University of Innsbruck (2012).

[110] A. Kuhn, H. Perrin, W. Hänsel, and C. Salomon, *Three Dimensional Raman Cooling using Velocity Selective Rapid Adiabatic Passage*, in OSA TOPS on Ultracold Atoms and BEC, K. Burnett (eds.), Opt. Soc. Am. **7**, 58; arXiv:1109.5237 (1996).

[111] H. Perrin, A. Kuhn, I. Bouchoule, and C. Salomon, *Sideband cooling of neutral atoms in a far-detuned optical lattice*, EPL **42**, 395–400 (1998).

[112] H. F. Hess, *Evaporative cooling of magnetically trapped and compressed spin-polarized hydrogen*, Phys. Rev. B **34**, 3476–3479 (1986).

[113] W. Ketterle and N. J. van Struten, *Evaporative Cooling of Trapped Atoms*, Advances In Atomic, Molecular, and Optical Physics, Bd. **37**, 181–236 (1999).

[114] K. M. O'Hara, M. E. Gehm, S. R. Granade, and J. E. Thomas, *Scaling laws for evaporative cooling in time-dependent optical traps*, Phys. Rev. A **64**, 051403(R) (2001).

[115] C.-L. Hung, X. Zhang, N. Gemelke, and C. Chin, *Accelerating evaporative cooling of atoms into Bose-Einstein condensation in optical traps*, Phys. Rev. A **78**, 011604(R) (2008).

[116] D. Meschede, *Gerthsen Physik*, 23. Ed., Berlin Heidelberg New York: Springer, 2006.

[117] M. Rehberger, *Ultracold Erbium Atoms in Far-Detuned Optical Traps - Construction of a Zeeman-Slower*, Masterarbeit, Rheinische Friedrich-Wilhelms-Universität Bonn (2013).

[118] D. Babik, *Frequency stabilization of a dye laser for narrow-line laser cooling of erbium atoms*, Masterarbeit, Rheinische-Friedrich-Wilhelms-Universität Bonn (2014).

[119] A. Harder, *Setup and testing of an apparatus for cooling and trapping erbium atoms*, Masterarbeit, Rheinische Friedrich-Wilhelms-Universität Bonn (2014).

[120] M. Prentiss, E. L. Raab, D. E. Pritchard, A. Cable, J. E. Bjorkholm, and S. Chu, *Atomic-density-dependent losses in an optical trap*, Opt. Lett. **13**, 452 (1988).

[121] N. F. Ramsey, *Molecular Beams*, Oxford: Oxford University Press, 1963.

[122] G. Scoles, *Atomic and Molecular Beam Methods Volume I*, Oxford: Oxford University Press, 1988.

[123] C. Bolkart, *Erzeugung eines ultrakalten Gases fermionischer Kaliumatome im optischen Dipolfallenpotential*, Dissertation, Rheinische Friedrich-Wilhelms-Universität Bonn (2011).

[124] A. Gatto, *Trapping fermionic potassium atoms in a quasi-electrostatic optical dipole potential*, Dissertation, Rheinische Friedrich-Wilhelms-Universität Bonn (2011).

[125] D. J. McCarron, S. A. King, and S. L. Cornish, *Modulation transfer spectroscopy in atomic rubidium*, Meas. Sci. Technol. **19**, 105601 (2008).

[126] V. Negnevitsky and L. D. Turner, *Wideband laser locking to an atomic reference with modulation transfer spectroscopy*, Opt. Express **21**, 3103 (2013).

[127] R. W. P. Drever, J. L. Hall, F. V. Kowalski, J. Hough, G. M. Ford, A. J. Munley, and H. Ward, *Laser phase and frequency stabilization using an optical resonator*, Appl. Phys. B **31**, 97–105 (1983).

[128] M. Hohn, *Frequenzstabilisierung eines Diodenlasers mittels Doppler-freier Spektroskopie an einer Erbium-Hohlkathodenlampe*, Bachelorarbeit, Rheinische Friedrich-Wilhelms-Universität Bonn (2017).

[129] D. Dreon, L. A. Sidorenkov, C. Bouazza, W. Maineult, J. Dalibard, and S. Nascimbene, *Optical cooling and trapping of highly magnetic atoms: the benefits of a spontaneous spin polarization*, J. Phys. B: At. Mol. Opt. Phys. **50**, 065005 (2017).

[130] D. Meschede, *Optik, Licht und Laser*, 2. Ed., Wiesbaden: Vieweg+Teubner, 2005.

[131] W. Ketterle and M. W. Zwierlein, *Making, probing and understanding ultracold Fermi gases*, Proceedings of the International School of Physics "Enrico Fermi" on Ultracold Fermi Gases, Course CLXIV, M. Inguscio, W. Ketterle, and C. Salomon (eds.); Amsterdam: IOS Press, 2008.

[132] L. Bergmann and C. Schaefer, *Lehrbuch der Experimentalphysik, Band 3, Optik*, 10. Ed., Berlin, New York: Walter de Gruyter, 2004.

[133] L. D. Landau and E. M. Lifschitz, *Lehrbuch der Theoretischen Physik, Band 1, Mechanik*, 14. Ed., Frankfurt am Main: Harri Deutsch, 2004.

[134] F. Chevy, V. Bretin, P. Rosenbusch, K. W. Madison, and J. Dalibard, *Transverse Breathing Mode of an Elongated Bose-Einstein Condensate*, Phys. Rev. Lett. **88**, 250402 (2002).

[135] P. D. Lett, R. N. Watts, C. I. Westbrook, W. D. Phillips, P. L. Gould, and H. J. Metcalf, *Observation of Atoms Laser Cooled below the Doppler Limit*, Phys. Rev. Lett. **61**, 169–172 (1988).

[136] J. D. Miller, R. A. Cline, and D. J. Heinzen, *Far-off-resonance optical trapping of atoms*, Phys. Rev. A **47**, R4567(R) (1993).

[137] W. Gerlach and O. Stern, *Der experimentelle Nachweis der Richtungsquantelung im Magnetfeld*, Z. Phys. **9**, 349–352 (1922).

[138] F. Gerbier, J. H. Thywissen, S. Richard, M. Hugbart, P. Bouyer, and A. Aspect, *Critical Temperature of a Trapped, Weakly Interacting Bose Gas*, Phys. Rev. Lett. **92**, 030405 (2004).

[139] K. Aikawa, A. Frisch, M. Mark, S. Baier, R. Grimm, J. L. Bohn, D. S. Jin, G. M. Bruun, and F. Ferlaino, *Anisotropic Relaxation Dynamics in a Dipolar Fermi Gas Driven Out of Equilibrium*, Physical Review Letters **113**, 263201 (2014).

[140] K. v. Klitzing, G. Dorda, and M. Pepper, *New Method for High-Accuracy Determination of the Fine-Structure Constant Based on Quantized Hall Resistance*, Phys. Rev. Lett. **45**, 494–497 (1980).

[141] M. I. D'Yakonov and V. I. Perel', *Possibility of Orienting Electron Spins with Current*, Sov. Phys. JETP **13**, 467 (1971).

[142] J. Sinova, D. Culcer, Q. Niu, N. A. Sinitsyn, T. Jungwirth, and A. H. MacDonald, *Universal intrinsic spin hall effect*, Phys. Rev. Lett. **92**, 126603 (2004).

[143] C. L. Kane and E. J. Mele, *Z_2 Topological Order and the Quantum Spin Hall Effect*, Phys. Rev. Lett. **95**, 146802 (2005).

[144] J. Dalibard, F. Gerbier, G. Juzeliūnas, and P. Öhberg, *Colloquium: Artificial gauge potentials for neutral atoms*, Rev. Mod. Phys. **83**, 1523–1543 (2011).

[145] N. Goldman, G. Juzeliūnas, P. Öhberg, and I. B. Spielman, *Light-induced gauge fields for ultracold atoms*, Rep. Prog. Phys. **77**, 126401 (2014).

[146] V. Bretin, S. Stock, Y. Seurin, and J. Dalibard, *Fast Rotation of a Bose-Einstein Condensate*, Phys. Rev. Lett. **92**, 050403 (2004).

[147] V. Schweikhard, I. Coddington, P. Engels, V. P. Mogendorff, and E. A. Cornell, *Rapidly Rotating Bose-Einstein Condensates in and near the Lowest Landau Level*, Phys. Rev. Lett. **92**, 040404 (2004).

[148] P. Hauke, O. Tieleman, A. Celi, C. Ölschläger, J. Simonet, J. Struck, M. Weinberg, P. Windpassinger, K. Sengstock, M. Lewenstein, and A. Eckardt, *Non-Abelian Gauge Fields and Topological Insulators in Shaken Optical Lattices*, Phys. Rev. Lett. **109**, 145301 (2012).

[149] J. Ruseckas, G. Juzeliūnas, P. Öhberg, and M. Fleischhauer, *Non-Abelian Gauge Potentials for Ultracold Atoms with Degenerate Dark States*, Phys. Rev. Lett. **95**, 010404 (2005).

[150] G. Juzeliūnas, J. Ruseckas, P. Öhberg, and M. Fleischhauer, *Light-induced effective magnetic fields for ultracold atoms in planar geometries*, Phys. Rev. A **73**, 025602 (2006).

[151] Shi-Liang Zhu, Hao Fu, C.-J. Wu, S.-C. Zhang, and L.-M. Duan, *Spin hall effects for cold atoms in a light-induced gauge potential*, Phys. Rev. Lett. **97**, 240401 (2006).

[152] K. Jiménez-García, *Artificial Gauge Fields for Ultracold Neutral Atoms*, Dissertation, NIST, and the University of Maryland (2012).

[153] M. Aidelsburger, M. Atala, M. Lohse, J. T. Barreiro, B. Paredes, and I. Bloch, *Realization of the Hofstadter Hamiltonian with Ultracold Atoms in Optical Lattices*, Phys. Rev. Lett. **111**, 185301 (2013).

[154] C. J. Kennedy, G. A. Siviloglou, H. Miyake, W. C. Burton, and W. Ketterle, *Spin-Orbit Coupling and Quantum Spin Hall Effect for Neutral Atoms without Spin Flips*, Phys. Rev. Lett. **111**, 225301 (2013).

[155] M. Aidelsburger, M. Atala, S. Nascimbène, S. Trotzky, Y.-A. Chen, and I. Bloch, *Experimental Realization of Strong Effective Magnetic Fields in an Optical Lattice*, Phys. Rev. Lett. **107**, 255301 (2011).

[156] F. Wilczek and A. Zee, *Appearance of Gauge Structure in Simple Dynamical Systems*, Phys. Rev. Lett. **52**, 2111–2114 (1984).

[157] Y.-J. Lin, K. Jiménez-García, and I. B. Spielman, *Spin–orbit-coupled Bose–Einstein condensates*, Nature **471**, 83–86 (2011).

[158] P. Wang, Z.-Q. Yu, Z. Fu, J. Miao, L. Huang, S. Chai, H. Zhai, and J. Zhang, *Spin-Orbit Coupled Degenerate Fermi Gases*, Phys. Rev. Lett. **109**, 095301 (2012).

[159] M. C. Beeler, R. A. Williams, K. Jiménez-García, L. J. LeBlanc, A. R. Perry, and I. B. Spielman, *The spin Hall effect in a quantum gas*, Nature **498**, 201–204 (2013).

[160] J. D. Jackson, *Classical Electrodynamics*, 2. Ed., New York: Wiley, 1987.

[161] J. Dalibard, *Introduction to the physics of artificial gauge fields*, Proceedings of the International School of Physics "Enrico Fermi" on Quantum Matter at Ultralow Temperatures, M. Inguscio, W. Ketterle, S. Stringari, and G. Roati (eds.); arXiv:1504.05520 (2016).

[162] D. Yoshioka, *The Quantum Hall Effect*, Berlin: Springer-Verlag, 2002.

[163] A. M. Martin, N. G. Marchant, D. H. J. O'Dell, and N. G. Parker, *Vortices and vortex lattices in quantum ferrofluids*, J. Phys.: Condens. Matter **29**, 103004 (2017).

[164] A. A. Abrikosov, *The magnetic properties of superconducting alloys*, J. Phys. Chem. Solids **2**, 199–208 (1957).

[165] N. Regnault and Th. Jolicoeur, *Quantum Hall Fractions in Rotating Bose-Einstein Condensates*, Phys. Rev. Lett. **91**, 030402 (2003).

[166] N. R. Cooper, N. K. Wilkin, and J. M. F. Gunn, *Quantum Phases of Vortices in Rotating Bose-Einstein Condensates*, Phys. Rev. Lett. **87**, 120405 (2001).

[167] B. Paredes, P. Fedichev, J. I. Cirac, and P. Zoller, $\frac{1}{2}$*-Anyons in Small Atomic Bose-Einstein Condensates*, Phys. Rev. Lett. **87**, 010402 (2001).

[168] F. Grusdt and M. Fleischhauer, *Fractional quantum Hall physics with ultracold Rydberg gases in artificial gauge fields*, Phys. Rev. A **87**, 043628 (2013).

[169] T. Lahaye, T. Koch, B. Fröhlich, M. Fattori, J. Metz, A. Griesmaier, S. Giovanazzi, and T. Pfau, *Strong dipolar effects in a quantum ferrofluid*, Nature **448**, 672–675 (2007).

[170] L. Chomaz, D. Petter, P. Ilzhöfer, G. Natale, A. Trautmann, C. Politi, G. Durastante, R. M. W. van Bijnen, A. Patscheider, M. Sohmen, M. J. Mark, and F. Ferlaino, *Long-Lived and Transient Supersolid Behaviors in Dipolar Quantum Gases*, Phys. Rev. X **9**, 021012 (2019).

Danksagung

Bedanken möchte ich mich an dieser Stelle bei einer Vielzahl von Personen, allen voran bei Herrn Prof. Dr. Martin Weitz, der mir in seiner Arbeitsgruppe die Möglichkeit gegeben hat, im Rahmen meiner Dissertation an einem spannenden Forschungsprojekt mitzuwirken. Seine Betreuung und Ideen halfen mir im Laboralltag bei der Lösung zahlreicher Probleme weiter, und trugen sehr zu meinem physikalischen Verständnis bei. Außerdem möchte ich Herrn Prof. Dr. Simon Stellmer für die freundliche Übernahme des Koreferats recht herzlich danken.

Desweiteren danke ich meinen Arbeitskollegen, die mich während der Dissertation im Labor tatkräftig unterstützt haben. Das war vor allem Roberto Röll, mit dem das Forschen nie langweilig wurde, und mit dem man, falls es doch mal schwierige Herausforderungen im Labor gab, nie den Humor verloren hat. Auch möchte ich meinen Betreuern aus alten Tagen zu Beginn der Promotion danken: Henning Brammer und Jens Ulitzsch. Von ihnen konnte ich viel physikalisches und technisches Know-How erlangen, und den Grundstein für diese Dissertation legen. Weiterhin danke ich allen Bachelor- und Masterstudenten, die unser Team über die Jahre am Erbium-Experiment verstärkt haben. Spezieller Dank gilt auch den Kollegen vom Rubidium-Nachbarexperiment, die uns bei der ein oder anderen technischen Hürde gerne unter die Arme gegriffen haben, zu nennen seien hier u.a. Martin Leder und Johannes Koch. Danke auch an die ganze Arbeitsgruppe, die immer sehr hilfsbereit, und für das ein oder andere Späßchen zu haben war. Ferner möchte ich noch der Verwaltung und den Werkstätten des IAPs danken. Zudem danke ich Herrn Prof. Dr. Michael Fleischhauer für die produktive Zusammenarbeit an unserem Paper.

Außerdem möchte ich mich noch bei meiner Familie, und insbesondere bei meinen Eltern bedanken, die immer eine gute Unterstützung während des Studiums gewesen sind. Zuletzt danke ich auch allen meinen Freunden, die in der ganzen Zeit ein willkommener Gegenpol zum Arbeitsalltag waren, und mich stets motiviert haben. Vielen Dank!